Structure Elucidation, Signaling Mechanism and Structure-Based Lead Design of the Human Cannabinoid Receptor 2 (CB2)

by

Changrui Xing

Bachelor of Science, Fudan University, 2014

Master of Science, University of Pittsburgh, 2016

Submitted to the Graduate Faculty of the

School of Pharmacy in partial fulfillment

of the requirements for the degree of

Doctor of Philosophy

University of Pittsburgh

2020

UNIVERSITY OF PITTSBURGH

SCHOOL OF PHARMACY

This dissertation was presented

by

Changrui Xing

It was defended on

July 14, 2020

and approved by

Cheng Zhang, Assistant Professor, Department of Pharmacology and Chemical Biology

Guillermo G. Romero, Associate Professor, Department of Pharmacology and Chemical Biology

Junmei Wang, Associate Professor, Department of Pharmaceutical Sciences

Terence McGuire, Assistant Professor, Department of Pharmaceutical Sciences

Zhiwei Feng, Assistant Professor, Department of Pharmaceutical Sciences

Dissertation Advisor: Xiang-Qun Xie, Professor, Department of Pharmaceutical Sciences

Structure Elucidation, Signaling Mechanism and Structure-Based Lead Design of the Human Cannabinoid Receptor 2 (CB2)

Changrui Xing, PhD

University of Pittsburgh, 2020

Cannabinoid receptor 2 (CB2) has an important role in mediating immune signal transduction and is an attractive therapeutic target for chronic neuropain, osteoporosis, autoimmune diseases, and tumors of immune origin. Unlike CB1, which is expressed in the central nervous system (CNS), CB2 is primarily expressed in cells of the immune system and its selective modulation will not produce psychoactive effects. This feature has attracted great interest in CB2, particularly since the anti-obesity drug Rimonabant (CB1 antagonist) was withdrawn from the European market due to depression side effects.

Despite research efforts to date, the CB2 active-state structure, activation mechanism, and allosteric binding features remain elusive, representing a significant hindrance in the development of novel CB2 agonist and allosteric modulators. Thus, in this study, we first unveiled the cryo-EM structure of CB2-Gi signaling complex to gain an unprecedented understanding of the structural and functional mechanisms inherent to CB2 using high-end biophysical and biochemical approaches with purified functional CB2. Next, we developed and applied an innovative residual energy calculation algorithm to aid in the design of a pair of selective CB2 agonist and inverse agonist in order to validate our putative mechanism of receptor activation involving the structural arrangement of critical residues. Then, we investigated the binding features of selective CB2 agonists, as well as the CB2 biased ligand and CB2 positive allosteric modulators (PAMs) and negative allosteric modulators (NAMs).

Collectively, the results from this study will provide insightful information to facilitate structure-based design and discovery of high-affinity and/or high-selectivity CB2 ligands that can be developed as CB2-targeting therapeutic agents.

Table of Contents

List of Tables

List of Figures

Preface

I am lucky to have my Ph.D. training at the University of Pittsburgh, School of Pharmacy. I would like to express my deep gratitude to my advisor, Dr. Xiang-Qun Xie, for his dedicated support and mentorship since 2014. His trust and encouragement allow me to pursue my research interest. I would like to thank Dr. Cheng Zhang for allowing me to study in his lab at the School of Medicine and for supporting my independent research while giving me instructions all the time.

I also would like to thank my committee members, for their valuable suggestions on my research and the precious time and efforts they have committed. I would also acknowledge my dearest friends and colleagues in the School of Pharmacy, who helped me through the hardest times.

I'd also like to thank all the faculties and lab fellows in the CCGS center, the staff, faculty, and students in the School of Pharmacy. I have learned a lot from everyone.

Finally, I give my gratitude to my family for their love and support. I want to thank my parents, and in-laws for their understanding and encouragement. I also want to thank my beloved wife, my best friend and soul mate, with whom I shared joys and tears all over the years. We met each other in Pittsburgh on August 5, 2014. Our marriage at Pitt and our lovely son, Eddie, are the best gifts during my graduate study, as well as the rest of my life. With the power of love, I will keep marching forward on my way of life and career regardless of trials and hardships.

Abbreviations

Å	Ångström
ABDT	AdaBoost decision tree
AC	Adenyl cyclase or adenylate cyclase
AD	Alzheimer's disease
AHD	α-helical domain
AMP	Adenosine monophosphate
AM	Allosteric modulator
AEA	Anandamide
APS	Advanced photon source
2-AG	2-arachidonoylglycerol
3-D	Three Dimensional
Arg	Arginine
Asp	Aspartic acid
B_{max}	Maximum binding capacity
BN	β2-AR N-terminal
BSA	Bovine serum albumin
β2-AR	β2-Adrenergic Receptor
cAMP	Cyclic adenosine monophosphate
CB1/2	Cannabinoid receptor 1 or 2
CBD	Cannabidiol
C'	Carboxy terminal
CCL2	Chemokine (C-C motif) ligand 2
cDNA	Complementary DNA
ºC	Degree Celsius
CNS	Central nervous system
CPM	Counts per minute or 7-Diethylamino-3-(4'-Maleimidylphenyl)-4-Methylcoumarin

CHO	Chinese hamster ovary cell
CHAPS	3[(3cholamidopropyl)dimethylammonio]-1-propanesulfonate hydrate
CHS	Cholesteryl hemisuccinate
CMC	Critical micelle concentration
Cryo-EM	Cryogenic electron microscopy
CXCL8	Interleukin 8
DCM	Dichloromethane
DNA	Deoxyribonucleic acid
DMSO	Dimethyl sulfoxide
DMF	Dimethylformamide
DTT	Dithiothreitol
DPBS	Dulbecco's Phosphate-Buffered Saline
DDM	Dodecyl-beta-D-maltoside
DT	Allodecision tree
ECL	Extracellular loop
ECS	Endocannabinoid system
EDTA	Ethylene diaminetetraacetic acid
EGTA	Ethylene glycol tetraacetic acid
ERK	Extracellular signal-regulated kinase
E.coli	*Escherichia coli*
EC_{50}	Half maximal effective concentration
EM	Electron microscopy
FAAH	Fatty acid amide hydrolase
Fab	Antigen-binding fragment
FBS	Fetal bovine serum
FDA	The Food and Drug Administration
Flag	Epitope, octapeptide protein tag
FUB	Fubinaca
g	Gram
GTP	Guanosine 5'-triphosphate
$G\alpha_i$	G alpha subunit inhibitory

$G\alpha_s$	G alpha subunit stimulatory
$G_{\alpha/\beta\gamma}$	G protein (Gα and Gβγ subunits)
GDP	Guanosine 5'-diphosphate
GIRK	G protein-coupled inwardly-rectifying potassium channel
GPCR	G-protein coupled receptor
GPR55	G-protein coupled receptor-55
× g	Centrifugal force
Glu	Glutamic acid
h or Hrs.	Hours
hCB1/2	Human cannabinoid receptors 1 or 2
HA	Hemagglutinin
His	Histidine
HEK	Human Embryonic Kidney cells
HEPES	4-(2-hydroxyethyl)-1-piperazineethanesulfonic acid
ICL	Intracellular loop
IMAC	Immobilized Metal Affinity Chromatography
IA	2-Iodoacetamide
IPTG	Isopropyl β-D-1-thiogalactopyranoside
Ile	Isoleucine
IL-12	Interleukin 12
K_i	Binding Affinity of the inhibitor
kDa	Kilodalton
LB	Luria-Bertani
L	Liter
LCP	Lipid cubic phase
Lys	Lysine
Leu	Leucine
MAPK	Mitogen-activated protein kinase
MAG	
MEK	MAP kinase kinase
Met	Methionine

mins	Minutes
ml	Milliliter
mM or mmol	Millimolar
M	Molar
MNG	Lauryl maltose neopentyl glycol
MBP	Maltose binding protein
MLP	Multi-layer perceptron
MW	Molecular weight
N'	Amino terminal
NAM	Negative allosteric modulator
NB	Naïve bayes
Ni-NTA	Ni-Nitrilotriacetic acid agarose
nM	Nanomolar
NMR	Nuclear Magnetic Resonance
PAM	Positive allosteric modulator
Phe	Phenylalanine
pH	-log10 [H+]
PNGase F	Peptide -*N*-Glycosidase F
PI3K	Phosphatidylinositide-3-kinase
PCR	Polymerase chain reaction
P1 ,P2 and P3	Virus passage
Pro	Proline
ppm	Parts per million
$PtdInsP_2$	Phosphatidylinositol 4,5-bisphosphate
RF	Random forest
RT	Room temperature
Rev	Reverse
SAM	Silent allosteric modulator
SAR	Structure activity relationship
ScFv	Single-chain variable fragment
Ser	Serine

Sf21 and Sf9	*Spodoptera frugiperda* (insect cell)
S.E.M	Standard Error of Mean
SDS	Sodium dodecyl sulfate
SDS-PAGE	Sodium dodecyl sulphate polyacrylamide gel electrophoresis
SEC	Size exclusion chromatography
SVM	Support vector machine
TCEP	*tris*(2-carboxyethyl)phosphine
TEA	Triethylamine
TEV	Tobacco Etch Virus nuclear-inclusion-a endopeptidase
TM	Transmembrane
TNF-α	Tumor necrosis factor alpha
Tris	Tris (hydroxymethyl) aminomethane
Tris-HCl	Tris - hydrogen chloride
THC	Tetrahydrocannabinol
Trp	Tryptophan
TRP	Transient receptor potential
Tyr	Tyrosine
Val	Valine
VGCC	Voltage-gated calcium channels
WB	Western blot
WT	Wild type
µM	Micromolar
µg	Microgram

1.0 Introduction

1.1 Endocannabinoid System

Cannabis has been used by humans as medicines for a very long time. Nearly 5000 years ago, the Chinese had already described the use of marijuana to treat cramps and pain [1]. It was recorded that about 3000 years ago, ancient Indians also used the hemp for anxiety-relieving. The use of marijuana did not reach the Americas and Europe until the 19th century, but it was developed as both medicinal agent and recreation drugs. Later, the extraction from marijuana was widely spread across the United States for medical use until 1937, when people realized the potential drug abuse issue brought by marijuana and start banning it. However, people have regained interest in marijuana recently especially when nowadays more than 30 states have legalized the medical use of it in the United States. This also led to the research interest in the endocannabinoid system (ECS), which becomes the molecular targets for the therapeutic agents.

Scientists have been studying the role of ECS and its related receptors and ligands for more than 50 years. ECS is a complex and homeostatic system that has now been indicated to be involved in a broad spectrum of physiological and pathological processes such as appetite regulation [2], peripheral energy metabolism [3], pain and inflammation [4, 5], cardiovascular regulation [6], musculoskeletal disorders [7], and cancer [8]. However, people did not know the underlying mechanism until the 1990s. At first, the effect of marijuana was thought to be caused by the non-specific interactions between the active component (−)-trans-Δ^9-tetrahydrocannabinol (THC) to the cell membrane [9]. THC was one of the more than 60 cannabinoids that exist in the plant, which discovered and isolated in 1964 by Raphael Mechoulam and Yechiel Gaoni [10].

Subsequently, from the 1970s, scientists have synthesized a broad spectrum of analogs or cannabinoids with diverse chemical structures. Among them, the cannabinoid agonist CP-55,940 was found to have saturable and high-affinity binding to the mouse brain plasma membrane, which led to the discovery of cannabinoid receptors. Interestingly, this finding was consistent with the cAMP inhibition and analgesic effect of the compound in *in vitro* and *in vivo* models, respectively. Later, the development of radioactive labeling technology enables the mapping of cannabinoid receptors inside the human body. As a result, the two most important GPCRs in the ECS, cannabinoid receptors 1 (CB1) and cannabinoid receptor 2 (CB2) were identified.

Further studies on the ECS make both CB1 and CB2 valuable therapeutic targets for varies of pathological or physiological conditions:

Pain and inflammation

There is a long history for human beings to use cannabis for the treatment of pain [11]. *In vivo* studies of many phytocannabinoids such as THC, cannabidiol, as well as synthetic cannabinoids such as CP-55,940 and WIN 55,212-2 have shown the inhibition of acute pain including chemical, mechanical and thermal pain stimuli [4, 12-16]. Recent preclinical studies also showed that cannabinoids have the potential to treat chronic pain from both inflammatory and neuropathic origin [17-23]. Besides, when using together with non-steroid anti-inflammatory drugs, both synthetic and endogenous cannabinoid ligands showed synergistic analgesic effects [24, 25]. The antinociceptive effects of some commonly used analgesic drugs such as acetaminophen and propofol were also proved to be involved in the activity within the endocannabinoid system [26, 27]. The underlying mechanism of the antinociceptive effects is complex and related to both CB1 and CB2 receptors in the central nervous system and peripheral nervous system respectively. Many evidence showed that cannabinoid receptors are responsible

for immune regulation and the regulation of inflammation [5, 28-30]. The anti-inflammatory effects are involved in many biological processes such as the infection of cytokine (e.g., IL-12 and TNF-α) and chemokine production (e.g., CCL2 and CXCL8); the regulation of adenosine; the upregulation of adhesion molecules and the apoptosis and proliferation of inflammatory cells [5, 28-30].

Cancer

Cannabinoids are usually used on chemotherapy-treated patients for the pain-relieving, appetite stimulation, and nausea inhibition [31, 32]. THC and its analog have been approved by the FDA for the treatment of nausea in patients with cancer [31, 32]. Additionally, it has been reported that some cannabinoids can directly inhibit the growth of the tumor by inhibiting tumor cell migration, increasing the apoptosis in tumor cells, and reducing tumor angiogenesis [33-38]. It was proved that cannabinoids including cannabidiol, 2-AG, and anandamide can induce apoptosis in various tumor cell lines such as breast cancer, leukemia, and prostate cancer [39-42]. Importantly, in vivo experiments in mice also showed that cannabinoids can inhibit the tumor growth of various kinds such as skin carcinoma, thyroid epithelioma, and lymphoma [43-45].

Nervous system disorders

ECS is involved in many physiological processes related to CNS, such as movement, mood, memory, and learning. It is a crucial system that protects the neuron from injuries and disorders including stroke, Alzheimer's disease (AD), multiple sclerosis, epilepsy, and Huntington's disease. For example, WIN 55,212-2 is reported to protect cortical neurons against hypoxia and glucose deprivation, prevent Aβ-induced microglial activation, loss of neuronal markers, and cognitive impairment [46, 47]. Anandamide can also prevent the Aβ-induced

neurotoxicity through the MAPK pathway in the cell-based assay [48]. It is also reported to dependently inhibited electroshock-induced seizures in animal models [49].

Drug addiction

Drugs that have addictive properties often increase the dopamine levels in the nucleus accumbens or have the ability to activate the mesolimbic dopaminergic reward pathway [50, 51]. Like other drugs of abuse, the active component of marijuana, THC increases the extracellular dopamine levels in the nucleus accumbens 0074hrough the activation of the CB1 receptor [52, 53]. It is also reported that THC can decrease the reward threshold for electrical brain stimulation [54], and downregulate the corticotropin-releasing factor levels in the central nucleus of the amygdala [55, 56], which are believed to be involved in the drug abuse activity. THC also meets the reward-related behavioral criteria for abusive drugs by supporting conditioned place preference and restore cocaine-seeking behavior in rats [57-60]. Besides, the activation of the CB1 receptor by their endogenous ligands goes through retrograde transmission [61-63]. It is reported that drug abuse can cause synaptic plasticity and long term depression through similar mechanisms. Further studies also show that CB1 receptor antagonists can mitigate the behavioral and neurochemical responses to different classes of abusive drugs. These findings indicate the important role of the endocannabinoid system and the CB1 receptor in the drug abuse-related pathway [64, 65].

Cardiovascular disease

The cardiovascular effect of cannabinoids is complex and reported to be involving in the regulation of myocardium and vasculature [66-72], as well as the modulation of autonomic outflow in the nervous systems [73-77]. CB1 receptors are found in the myocardium and vascular tissues where they can mediate the negative inotropy and lead to vasodilation respectively [66, 69, 70, 78, 79]. These effects are related to the hypertensive effects caused by anandamide. The CB2 receptor

was proved to be less important in terms of cardiovascular interventions. It is only reported to be involved in the ischemic preconditioning injury of the myocardium. CB2 selective antagonist SR144528 can reduce the beneficial effects of pretreatment of endotoxin, which causes a decrease of functional recovery on reperfusion and an increase in the infarct size. These effects are not observed in CB1 selective antagonist SR141716. Similarly, SR144528 but not SR141716 can abolish the infarct size-reducing effect conferred by heat stress preconditioning in isolated rat hearts [80, 81].

Both CB1 and CB2 receptors were initially cloned in the 1990s and were reported to have pertussis toxin-sensitive signaling through $G_{\alpha i/o}$ proteins. However, it was demonstrated that although CB1 and CB2 had a similar affinity towards $G_{\alpha i}$, CB2 had a significantly lower binding affinity for $G_{\alpha o}$. Interestingly, CB1 is demonstrated to be coupling with $G_{\alpha s}$ and $G_{\alpha q}$ too under some circumstances or in certain cells, where $G_{\alpha i}$ activation is limited. Activation of these receptors triggers the replacement of GDP with GTP on G_{α} subunit, which cause the dissociation of the G_{α} and $G_{\beta\gamma}$ subunit. G_{α} and $G_{\beta\gamma}$ subunit will then act as effectors and trigger downstream signals inside the cells such as the regulation of adenylate cyclase by $G_{\alpha i}$ or $G_{\alpha s}$; the inhibition of calcium channels and activation of potassium channels caused by the release of $G_{\beta\gamma}$ subunit; the activation of mitogen-activated protein kinases (MAPK); the recruitment of β-arrestin and G protein independent pathways that related to the internalization and desensitization of the receptor.

As a therapeutic target, CB2 has a notable advantage over CB1 in its pattern of expression. CB1 is primarily expressed in the central nervous system (CNS) and is the primary receptor responsible for the psychotropic effects of THC and the deleterious psychiatric side effects of CB1-targeting drugs. The CB1 inverse agonists Rimonabant and Taranabant (MK-0364), both of which were developed as anti-obesity drugs, produce crippling CNS side effects of anxiety, depression,

and suicide [82-84] and were consequently either withdrawn from the market or dropped in clinical trials. In contrast, CB2 is predominantly expressed in peripheral tissues of the immune system, such as the spleen and thymus, where it modulates immune suppression, apoptosis, and cell migration [85, 86]. Modest levels of CB2 expression have also been observed in several areas of the brain such as the ventral tegmental area dopamine neurons and the hippocampal CA3 neurons [87], which regulate cravings of drug addiction and memory processes, respectively [88]. Thus, it is believed that selective CB2 ligands can be developed as treatments for a number of disorders while avoiding the severe psychiatric side effects associated with CB1 [89]. Regarding the ligand efficacy, although CB2 antagonists/inverse agonists have been reported to promote osteoclast apoptosis and to prevent bone loss [90], a large body of evidence has indicated a broad therapeutic application of CB2 agonists in neurodegenerative disorders [91, 92], drug abuse or addiction [93], cardiovascular diseases [94], neuroinflammation and neuropathic pain [95-97]. However, the lack of a well-defined CB2 ligand activation and signaling mechanism has hindered development of novel synthetic CB2 agonists.

Besides two of the most abundant cannabinoid receptors CB1 and CB2, several other GPCRs including GPR18, GPR55 and GPR119 have been reported to be activated by the endogenous or synthetic cannabinoids. These ligands can also interact with glycine receptors or transient receptor potential (TRP) channels. There is still much to explore in terms of the function, mechanism as well as the contribution of these receptors to the therapeutic effects of cannabinoids.

1.2 Discovery of GPCRs Structures

G-protein-coupled receptors (GPCRs) consist of a large family of membrane proteins that

are responsible for the transduction of signals across the cell membrane. They are characterized by the seven transmembrane domain (TM) and the extracellular and intracellular loops that connect them. More than 800 GPCRs in the human genome have been discovered, where they can be classified into six families based on their sequence and function similarity: Class A (Rhodopsin-like); Class B (Secretin receptor family); Class C (Metabotropic glutamate/pheromone); Class D (Fungal mating pheromone receptors); Class E (Cyclic AMP receptors) and Class F (Frizzled/Smoothened). Among them, the Rhodopsin-like family is the most abundant protein family which includes neurotransmitters, hormones, and light receptors, etc., that account for about 80% of GPCRs. Based on the phylogenetic study, they can be further classified into 19 subfamilies which will not be discussed in detail here.

GPCRs are one of the most diverse and largely expressed proteins in the human body, where they are involved in numerous physiological and pathological processes, such as immune response, appetite regulation, muscle contraction, Alzheimer's disease, pain, and cancer. Although there is a great diversity in terms of GPCR functions in the human body, the structure of GPCRs shares a great extent of homology, especially in the 7-TM helices. The ligand-binding pocket usually resides in the upper part of 7-TM helices, while the lower part, together with the intracellular loops and C-terminus, is crucial for G protein binding and downstream signal transductions. On the other hand, the N-terminus and extracellular loops play an important role in ligand recognition and selectivity.

Regarding GPCR dynamics, they are considered in an equilibrium where an active state and an inactive state exist at the same time. Upon ligand activation, the equilibrium will break and the conformation of GPCR will change from inactive state to active state, caused by a series of signal propagation. This change will then result in the GTP-GDP exchange, followed by the release

of G protein, which will lead to the downstream signal cascades. In contrast, the inverse agonists of GPCRs will shift the equilibrium to the inactive state and decrease the activation by their agonists or the basal activity.

GPCRs are promising drug targets. Among all FDA-approved drugs, about 34% of them or about 475 drugs target GPCRs. They are account for a global sales volume of over 180 billion US dollars annually. According to clinical studies, there are approximately 321 agents target 66 potentially novel GPCR targets that do not currently have an approved drug. Moreover, 224 clinically unexplored non-olfactory GPCRs have the potential to treat a series of diseases especially genetic and immune system disorders. In short, the research on GPCRs is extremely important for all the patients and human beings across the globe and will bring huge social and economic impact.

Although remarkable progress has been made recently in terms of structural elucidation of GPCRs, the determination of GPCR structures has always been a difficult research area and is often different case by case. At present, out of more than 800 GPCRs that are known, less than fifty have 3-D crystal structures that have been published [98, 99]. One reason can be attributed to the seven transmembranes (7TM) domains and numerous conformations of the GPCRs that account for their functional versatility. This structural heterogeneity brings difficulties to obtain a complex stable enough to grow crystals suitable for X-ray diffraction studies.

Like many other GPCRs, CB2 is expressed at levels usually insufficient for biophysical studies in both cultured cells and native tissues due to the limited cell membrane area and self-aggregation. Additionally, there is the difficulty maintaining the structural and functional integrity of CB2 during the expression and purification process due to the absence of a cell membrane.

Further, for cryo-EM studies, the stabilization of CB2-G_i interactions is a major challenge in obtaining high-resolution structural information that gives insights into CB2 signaling mechanisms. Many approaches have been developed to enhance CB2-G_i complex formation, including insertions of mutations in G proteins and inclusion of additives like anti-G_i Fab, scFv, or $PtdInsP_2$ during complex formation. Optimization of the various factors is necessary to acquire the best stabilized CB2-G_i complex suitable for cryo-EM study can be challenging.

1.3 Current Development of Cannabinoid Drugs

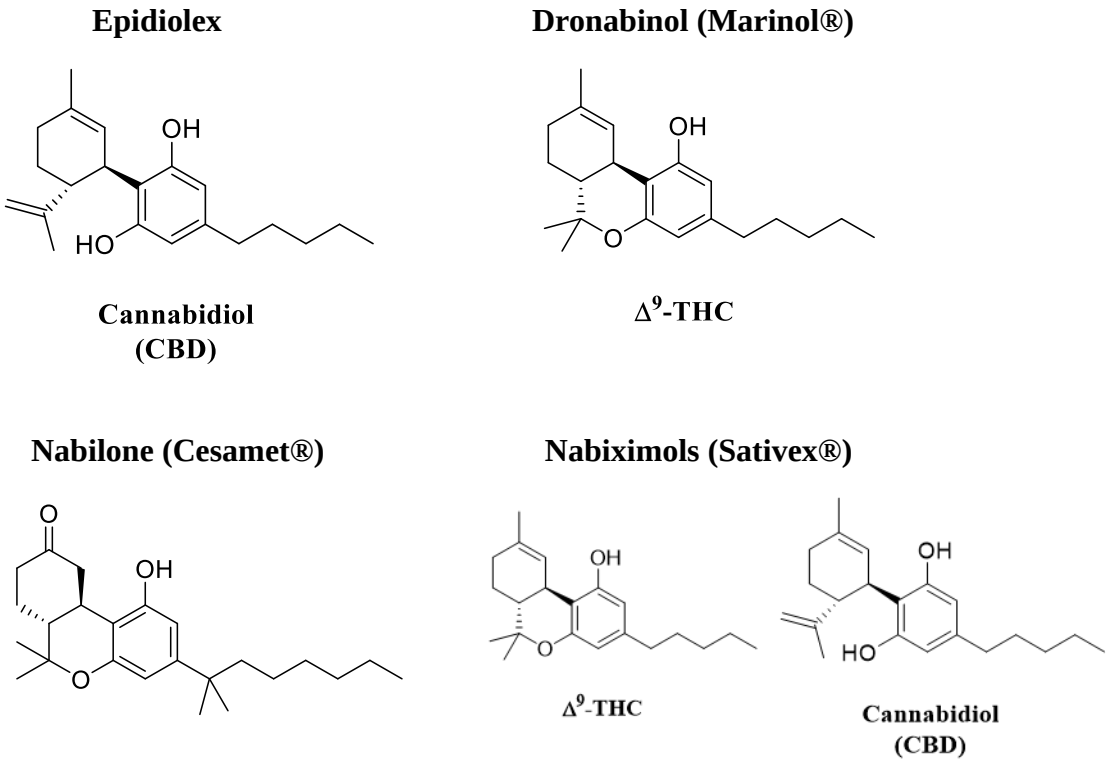

Figure 1. Cannabinoid receptor drug on the market

Four cannabinoid drugs are approved by the FDA. Cannabidiol is the active component of Epidiolex and THC is the

active component of Dronabinol. Nabilone is the synthetic analogue of THC and Nabiximols is the combination of THC and cannabidiol.

Although the cannabinoid receptors have been discovered for more than 30 years, there are still no CB2 selective drugs available in the market, which partly due to the lack of CB2 structures and activation mechanisms. **Figure 1** shows the current therapeutic agent in the market that targets the cannabinoid system for the treatment of spasticity, nausea, or pain. Epidiolex was approved by FDA in 2018 for the treatment of a rare and severe form of epilepsy. Its active component is cannabidiol (CBD) and it is the first and only FDA approved prescription CBD [100]. Dronabinol is another extract from cannabis. The active component is the specific enantiomer of THC, which is used to treat cannabis addiction, mitigate chronic pain, and stimulate the appetite [101-105]. Nabilone is a synthetic cannabinoid that mimics the structure of THC. It is approved for the treatment of vomiting, nausea, movement disorder, and neuropathic pain [105, 106]. Nabiximols is a combination drug with THC: CBD = 1.08: 1. It has been shown to be effective for spasticity reduction [107]. However, all of the drugs listed here are either phytocannabinoid that extracted from the plant such as CBD and THC, or the very similar analogue of them. They tend to have multiple targets or side effects such as dizziness, dry mouth, sleep disturbance and euphoria, etc. [101, 108, 109] Besides, the CB2 drugs in the clinical trials are also very limited, as partly summarizaed in the Appendix A, Table 4. Thus, it is crucial to understand the structural information of cannabinoid receptors to design a higher level of therapeutics that have better selectivity and fewer side effects.

Recently, the allosteric modulators of cannabinoid receptor have gained much attention from the scientist due to their advantages compared to the orthosteric ligands. Allosteric modulators are ligands that bind to different pockets from the orthosteric binding site. They

modulate the efficacy and affinity of orthosteric ligands by altering the conformation of the receptor. Based on the effect of allosteric modulators, they can be classified as positive allosteric modulator (PAM), negative allosteric modulator (NAM) and silent allosteric modulator (SAM). PAM alters the function of the receptor by upregulating the orthosteric ligand-driven signals. It can also reduce the desensitization of the receptor. On the other hand, NAM can decrease the affinity or efficacy of the agonist that bound to the orthosteric site, while SAM act as neutral modulators that compete with NAM or PAM but does not modulate orthosteric activities. Interestingly, several allosteric modulators can trigger signals independently without the presence of orthosteric ligands. Other modulators can be either PAM or NAM based on the signal output being measured [110].

Compared with orthosteric ligands, allosteric modulators of cannabinoid receptors are favored due to the following reasons: (1) Ceiling effect. The activity of allosteric modulators relies on the presence of orthosteric ligands. Thus, increasing the concentration of allosteric modulators beyond saturation will not elevate the downstream signals of the receptor. This feature can be very useful to avoid the risk of overdose caused by traditional ligands. (2) Subtype selectivity. Allosteric modulators give us a better chance to design CB1 or CB2 selective drugs because most of the time, the orthosteric binding pocket is very similar among subtypes of certain GPCRs due to evolutionary conservation. However, the allosteric binding site can be very different, which provides strategies to design selective modulators that have fewer adverse effects. (3) Spatial and temporal selectivity. Under pathological circumstances, the level of both cannabinoid receptors and endogenous ligands might vary significantly among different tissues. Unlike orthosteric ligands, allosteric modulators can only exert their effects where the endogenous ligands or orthosteric ligands exist. As a result, a “fine-tuning” pattern will be shown because the therapeutic

effect and its duration will depend on the level and location of the orthosteric ligands. (4) Functional selectivity. Orthosteric ligands of cannabinoid receptors often trigger a variety of downstream signals or have miscellaneous functional selectivity among different pathways. This is problematic because some pathways such as β-arrestin signaling will cause adverse effects such as drug tolerance. Nevertheless, allosteric modulators tend to stabilize certain conformations of the receptor, which allow us to obtain a more precise modulation of the pharmacological effects [110].

Although several CB1 and CB2 allosteric modulators have been developed, we are still in the early stage of allosteric research [111]. Since the very first CB1 allosteric modulator ORG27569 that generated in 2005 [112], scientists have spent intensive efforts to push it into translational use. However, even the two best known CB1 allosteric modulators ORG27569 and PSNCBAM-1 are not fully profiled in the animal studies, due to their inverse agonism effect other than NAM activity. Recently, the co-crystal structure of CB1 with both NAM ORG27569 and agonist CP-55,940 was solved [113]. The structure illustrates the binding site of CB1 NAM and the conformation of the orthosteric binding pocket as well as the whole receptor. This can be very useful to design allosteric drugs that modulate the CB1 receptor and to provide strategies and tools for the study of CB2 allosteric modulators.

In short, the development of both selective cannabinoid ligands and allosteric modulators are difficult, and researchers are at their beginning stages in terms of the understanding of their molecular mechanisms. More efforts are needed regarding the structural insights of cannabinoid receptors with different ligands, the translation between *in vitro* and *in vivo* assays, the development of more accurate pharmacological assays to study the kinetics of ligand binding as well as functional selectivity [114].

2.0 Advance and Application of Structural Biology Technologies

Structural biology came into history around the 1950s when the structures of globular proteins and several DNAs were solved [115, 116]. It is a subject that aims to unveil the molecular mechanisms of various macromolecular complexes inside the cells by uncovering the 3-D arrangement of their atoms. The development in structural biology has contributed substantially to the discovery of novel therapeutics. By now, there are mainly three technologies including Nuclear Magnetic Resonance (NMR) spectroscopy, X-ray crystallography, and electron microscopy (EM). Among them, X-ray crystallography has played the primary role to determine atomic models of macromolecules during the past 60 years. It also contributes most to the atomic coordinates of macromolecules deposited in the Protein Data Bank (PDB). Nuclear magnetic resonance (NMR) technologies appeared to the scientists in the 1980s and it allows people to obtain structures of macromolecules in solution. Although it provides unique information about molecular dynamics and interactions between them, the structure determination with high resolution, is restricted to small complex with molecular weight (MW) below 50 kDa. Furthermore, either X-ray crystallography or NMR technologies require a large amount of samples with higher purity, which makes it even difficult for structural biology studies of GPCRs. During the past 40 years, the EM technology or cryogenic electron microscopy (Cryo-EM) technology has been improved dramatically and not until recently become the major tool to study the structure of macromolecule complexes that are difficult to be dissolved in certain solutions or be crystallized. Recently, the development and breakthrough of both hardware and software in cryo-EM, together with the advancement in single-particle cryo-EM technology have been changing the structural biology field significantly.

2.1 NMR Spectroscopy and X-ray Crystallography

NMR spectroscopy has been invented for more than sixty years and is now a well-developed technology in structural biology, due to several technological advancements including higher magnetic field, cryoprobes, and the new design of spectrometer electronics [117]. NMR spectroscopy has many features that make it suitable for structural determination, molecular dynamics, and function analysis especially for soluble proteins with a relatively low molecular weight [118, 119]. First of all, NMR studies are usually carried out in the aqueous solution system, which makes it possible to study the structure-function relationship of the protein caused by the subtle change of its environments such as salt or pH. Also, the chemical shift mapping obtained in the NMR provides us strategies to validate the biochemical functions and to facilitate the drug development process. Additionally, by using the nuclear relaxation approach, we can characterize the changes in internal dynamics and thus study the relating mechanisms of molecular function. Lastly, NMR technology is particularly valuable for that protein that is difficult to produce diffraction quality crystals. For example, solid-state NMR has been developed as an important tool to study the structure of some membrane protein that is not accessible by X-ray crystallography. In short, NMR spectroscopy serves as a crucial and complementary approach to X-ray crystallography in the structural biology field, both for elucidating the 3-D structures and in the characterization of their biophysical or biochemical functions.

However, NMR spectroscopy has some limitations. Although during the past several decades, much significant progress has been made regarding the determination of structures of larger systems, current standard methods and application of NMR technology are limited to smaller proteins with molecular weights less than 25 kDa in order to obtain a higher resolution structure. In addition, a large amount of pure sample needed to be dissolved in the solution to

improve the signal to noise ratio. This is problematic especially for GPCRs that have both hydrophilic and hydrophobic domains and tend to have a relatively low expression level in the cells.

X-ray crystallography is a technology that uses X-ray to determine the position of atoms in crystals. It is one of the most commonly used technology to determine the 3-D structure of macromolecules including proteins and nucleic acids. Unlike NMR spectroscopy, the application of X-ray crystallography is not limited to the molecular weight or size of the macromolecule. X-ray crystallography usually gives high atomic resolution as well as the position and structure of the active center of the protein that helps us understand the molecular mechanism at the atomic level [120].

One of the most commonly used technology is single-crystal X-ray diffraction. Simply, atoms in the crystal will diffract the X-ray and from a scattered pattern on the detector. During this process, the crystal will rotate gradually which causes the change of both intensity and angle of these diffracted beams. Then, a 3-D image of the electron density within the crystal can be generated accordingly. Based on this information, a series of structural information can be obtained such as the atom positions, interactions, and some potential molecular mechanisms of flexibility and mobility of the protein. It also gives insights about the ligand-binding pocket, related conformational changes as well as the functional effects of point mutations in the protein sequences. All these structural information is important for structural-based drug design.

Over the past one hundred years, there has been significant discoveries and advancement in X-ray technologies that awarded Nobel Prizes. In 1895, Wilhelm Röntgen first discovered the X-ray that earned him the Nobel Prize in Physics [121, 122]. Max von Laue then discovered that X-rays can be diffracted by crystals, which opened a new era in the research of the atomic world

[123]. After one year, William H. Bragg and William L. Bragg got the Nobel Prize for the elucidation of NaCl structure from its crystal [124]. In 1934, J.D. Berna. took the first X-ray diffraction image of a protein. During the past 20 years, a significant amount of structures are determined by X-ray crystallography. As of January 2019, over 130,000 structures were reported in the PDB by using X-ray crystallography although only about 2% of them are related to the membrane proteins. Membrane proteins usually have both hydrophobic and hydrophilic domains that make them precipitated or denatured in the aqueous system. Thus, it is difficult to extract the membrane protein from the cell membrane without interfering with their native conformation or function. Johan Deisenhofer, Robert Huber, and Hartman Michel won the Nobel Prize in 1988 for their notable work, in which they start using detergents to solubilize and stabilize the membrane protein outside the cell membrane [125]. This idea makes later research possible and has a remarkable contribution to the work in the field including the determination of the 3-D structures of ATP synthase (Nobel Prize to John Walker in 1997), potassium channels (Nobel Prize to Roderick MacKinnon in 2003), and GPCRs (Nobel Prize to Robert Lefkowitz and Brian Kobilka, 2012).

Although X-ray crystallography has been widely used in the structural biology field for the determination of macromolecules, there are still some limitations. First of all, it requires the sample to be crystallized in a very organized pattern, which is usually difficult especially for those molecules with higher molecular weight or membrane proteins that have poor solubility and stability. Furthermore, we can only obtain one static conformation of the structure in the crystal without knowing information about its dynamic features or signaling mechanisms. The elucidation of secondary structures of the protein as well as the domain movement is also very difficult compared to NMR spectroscopy [120].

Briefly, both NMR spectroscopy and X-ray crystallization are important tools and are complementary techniques. All of the advantages and disadvantages mentioned above provide us a better strategy to answer different types of questions in the structural biology field.

2.2 Cryo-EM Development and Application

Cryo-EM is a technology based on electron scattering. The coherent electrons are used as the light source to measure cryogenic samples embedded in the vitrified water environment. When the beam passes the sample, it will be scattered, magnified, and then recorded on the detector. The utilization of cryo-EM has been limited to large molecules or low-resolution models for a long time. However, recent advancements in electron detection and image processing make cryo-EM very popular in the determination of GPCRs structures. It is also becoming a rival to X-ray crystallography and a newly dominant discipline in structure biology field [126].

The development of EM technology and its application in biological specimens goes back to the 1940s when Ruska use the first EM to take pictures of bacteriophage [127]. Back then, it was difficult to maintain the integrity of the sample while collecting the data due to the radiation damage as well as the preservation of the sample. Additionally, the dehydrated sample used in the initial EM was not optimum and always bring artificial structure to the native ones. In the early 1980s, scientists successfully made a thin layer of a noncrystalline form of solid water or vitrified water. This vitreous water environment allows the molecules to remain their shape and properties in a vacuum environment during the observation and this technology was named “cryo-EM”. Cryo-EM is a fast developing subject. In the early 1990s, people can only obtain the structure of the ribosome through cryo-EM at a 40Å resolution. When we go into the 21st century, it was

improved to about 10Å due to the advancement in image processing technology for asymmetric complexes. However, back to 10 years ago, there are still very few cryo-EM structures of asymmetric molecules with resolution beyond 7-9Å. It was not until 2013 that people start to get higher quality cryo-EM structure when the "resolution revolution" took place due to the development of electron detectors and the image processing approach [128]. In 2017, three scientists Joachim Frank, Jacques Dubochet, and Richard Henderson have been awarded the Nobel Prize in Chemistry for their contribution to cryo-EM development. The Nature Methods also named cryo-EM the "Method of the Year" in 2015 for its broad application in the structural biology field. Since the first cryo-EM structure was deposited in PDB in 1997, the number of deposited structures has grown significantly, among which many of these structures are previously thought impervious to structure determination [129].

There are many advantages of cryo-EM compared to conventional structural biology techniques. First of all, unlike X-ray crystallography, cryo-EM does not require the sample to be crystallized. This feature makes cryo-EM powerful in the structural determination and analysis of larger or more flexible complex such as membrane proteins, which are difficult to be crystallized. It also has an edge over X-ray crystallography due to its sample preparation process. The rapid freezing of the sample in cryo-EM help significantly with the maintenance of its native state. This can be crucial for the structural and functional investigation as well as the structure-based drug design. Additionally, the cryo-EM only requires a relatively small amount of sample compared to other approaches, which is important because the extraction and purification of membrane proteins with higher yield has always been difficult and case by case. Although cryo-EM has become one of the main disciplines in structural determination, it has some limitations. One of the main defects is that it usually generates a relatively low-resolution structure compared to X-ray crystallography,

which might due to the intrinsic properties of frozen-hydrated samples or low-dose imaging of frozen-hydrated biological molecules [130].

2.3 Single Particle Cryo-EM

Cryo-EM usually refers to three different techniques: single-particle cryo-EM, electron crystallography, and electron cryotomography. The single-particle cryo-EM was initially used in the structural determination of macromolecule complexes that are difficult to be crystallized, although the resolution might be relatively low. Back in the 1970s, when scientists first developed the single-particle cryo-EM, many difficulties make the resolution very poor [131, 132]. For example (1) the 3-D reconstruction process, (2) the maintenance of sample hydration during data collection under the beam, (3) the radiation damage by the high energy beam, and (4) the signal to noise ratio caused by the limitation of the electron dose. Many other factors have an impact on obtaining a high resolution including the homogeneity of the cryo-EM sample, the efficient data collecting, the alignment of 2D images, and the data processing procedures. Due to these challenges, it was very difficult to obtain high-resolution structures that sufficient to build an atomic model for further structural study and drug development. However, over the last decades, the groundbreaking technological advancement in instrumentation, computation, and sample preparation in single-particle cryo-EM has led a revolution in structural biology. Nowadays, we can obtain near-atomic resolution structures using single-particle cryo-EM and it has become the main discipline besides X-ray crystallography.

The “Resolution Revolution” of cryo-EM technology that happens recently can mainly be categorized into two parts: hardware and software [131]. (1) Direct-electron detectors. For a long time, photographic film was used for the data collection in the cryo-EM. However, the film is often poor at retaining the low-frequency signals which makes the overall resolution relatively low. Although people came up with the idea of recording two images of the same specimen with both high and low defocus to increase the overall resolution, it is still very time-consuming. In the late 1990s, the charge-couple device camera was introduced to replace the traditional film [132]. Although it enhances the resolution to some extent and facilitates the automated image acquisition process, it is not suitable for the routine determination of high-resolution structures because it needs to convert electrons into photon signals during the data collection. In comparison, the direct-coupled device camera does not require this conversion. Thus, it can localize the electron with much higher precision and increasing detective quantum efficiency. Furthermore, this camera can capture the sample image at a very high rate and generate a movie stack accordingly to facilitate further data processing and imaging approaches such as the correction of beam-induced image motion and the mitigation of radiation damage. We are now having several commercially available detectors of this kind from Gatan (K2), Direct Electron (DE) and FEI (Falcon). (2) Image processing algorithms. There are mainly two improvements in the image processing approach to address two problems encountered during the cryo-EM data collection. The first problem is the conformational or compositional heterogeneity of the sample, which will lead to the low-resolution mapping during the 3-D reconstruction process. This often happens when it is difficult to distinguish the 2-D projections of different conformations from the 2-D projections of different directions. Currently, many algorithms that address this issue have been implemented in the RELION software and allow the unsupervised 3-D classification as well as the high-resolution

reconstruction process. These algorithms are based on maximum-likelihood procedures, multivariate statistical analysis, nonstatistical multiparticle refinement, or 3-D variance calculation. It is a huge breakthrough regarding noise mitigation and human intervention compared with a previously used supervised 3-D classification that relies on the known structural variables of the sample. The second problem is the sample movement caused by the electron beam. This movement is usually caused by the breaking bonds or increasing charges of the sample under the beam, and it will be captured by the detector, which leads to a blurring map. Thus, researchers came up with the idea to record movies instead of images during the data collection. Consequently, the beam-induced motion correction algorithm was developed, which significantly improve the signal to noise ratio of the individual particle [132].

To summarize, compared to X-ray crystallography and NMR spectroscopy, cryo-EM has a relatively easy sample preparation process with less sample size. It is also more likely to give structures in a native state which is helpful for drug design and signaling mechanism studies (**Table 3**). cryo-EM is becoming a routine and powerful tool for structural determination and analysis due to all these advancements in both hardware such as detectors and software such as image processing algorithms.

3.0 Cryo-EM Structure of CB2-Gi Signaling Complex

3.1 Research Background

Cannabinoids (CB) can be defined as a class of compounds that act on CB receptors and affect various aspects of human physiology. There are mainly two subtypes of cannabinoid receptors termed CB1 and CB2. They share about 44% homology in protein sequence but as for distribution, CB1 is mainly located in the brain while CB2 is mainly expressed in the peripheral immune system such as spleens. Thus, as a therapeutic target, CB2 has advantages over CB1 in its pattern of expression. One of the examples is the withdrawal of famous CB1 inverse agonist Rimonabant as an anti-obesity drug in Europe. It is shown to have severe CNS side effects of depression, anxiety, or suicidal ideation. As a result, it is believed that selective CB2 ligands can be developed as treatments for a number of disorders while avoiding the severe psychiatric side effects associated with CB1. However, a lack of a well-defined CB2 ligand activation and signaling mechanism has hindered the development of novel synthetic CB2 agonists.

Although the CB2 crystal structure was published in 2019 [133], it has a certain number of drawbacks which make our study significant. First, The crystal structure published is in an inactive state, bound with a CB2 antagonist. But the agonist bound structure is still unknown. Second, there are mutations in the inactive state structure that used to stabilize the conformation in order to grow crystals with higher resolution. This alters the native structure of CB2 in cells and proved to cause the loss of cyclic AMP (cAMP) inhibition function. However, in cryo-EM, the CB2 will be in the native state without any mutations, which make the structure more convincing and useful in terms of novel drug development. Moreover, the crystal structure did not provide enough information

about ICL3, as well as G protein binding features, which is very important to understand the signaling mechanisms of G protein selectivity and specificity. Whereas the cryo-EM structure will show very detailed interactions between the CB2 and G protein.

In this study, we have built and optimized a systematic approach to construct, express, and purify CB2 receptors as well as the G protein in Sf9 insect cells. The first cryo-EM structure of CB2 G-protein complex bound to agonist was then obtained, together with the scFv antibody. Binding features of the agonist in the orthosteric binding pocket were examined. We have also designed, synthesized, and characterized a pair of rationally designed agonist and antagonist to support the binding mode of WIN 55,212-2 and structural determinants for distinguishing CB2 agonists from antagonists. Computational docking and MD simulation were also used to investigate the differences between CB2 and CB1 in receptor activation, ligand recognition, and G_i coupling.

3.2 Experimental Procedures

CB2 and G protein constructs

The full-length gene coding sequence of wild type human CB2 was cloned into pFastBac vector (ThermoFisher) with an N-terminal FLAG tag followed by β2-AR N-terminal tail region (BN, hereafter) as a fusion protein and a TEV cleavage site, along with a His8 tag at the C-terminal to facilitate expression and purification. The prolactin precursor sequence was inserted into the N-terminus as a signaling peptide to anchor CB2 to the membrane and improve CB2 expression. A dominant-negative bovine Gαi1 (Gαi1_4M) construct was generated by site-directed mutagenesis

to incorporate mutations S47N, G203A, E245A and A326S to decrease the affinity of nucleotide-binding of Gαβγ complex [134]. All three G protein complex components, Gαi1_4M, rat Gβ1, and bovine Gγ2, were cloned into pFastBac vector separately. ScFv16 coding sequence was cloned into pFastBac vector (ThermoFisher) with a GP67 signaling peptide inserted into the N-terminus and a TEV cleavage site-His8 at the C-terminus.

Protein complex expression, formation, and purification

CB2, Gαi1_4M, His8-tagged Gβ1, and Gγ2 were co-expressed in Sf9 insect cells (Invitrogen) using the Bac-to-Bac baculovirus expression system (ThermoFisher). Cell cultures were grown in ESF 921 serum-free medium (Expression Systems) to a density of 4×10^6 cells mL^{-1} and then infected with the four types of baculoviruses expressing CB2, Gαi1_4M, His8-tagged Gβ1, and Gγ2 at the ratio of 1:1:1:1. After infection at 27℃ for 48h, the cells were collected by centrifugation at 2000 rpm (ThermoFisher, H12000) for 20 min and kept frozen at -80℃ for further usage.

For the purification of CB2-G_i complex, cell pellets from 1.5L culture were thawed at room temperature and suspended by French press in 20 mM HEPES pH 7.2, 50 mM NaCl, 5 mM $CaCl_2$. The complex was formed on the cell membrane in the presence of 2 μM WIN 55,212-2 (Tocris) and treated with apyrase (25 mU/ml, NEB), followed by incubation for 1.5 h at room temperature. Cell membranes were collected by ultra-centrifugation at 100,000 x g for 35 min. The membranes were then re-suspended and solubilized in buffer containing 20 mM HEPES, pH 7.2, 100 mM NaCl, 5 mM $CaCl_2$, 10% Glycerol, 0.5% (w/v) dodecyl-β-D-maltoside (DDM, Anatrace), 0.15% (w/v) cholesteryl hemisuccinate TRIS salt (CHS, Anatrace), 0.5% (w/v) 3-[(3-cholamido-propyl)-dimethylammonio]-1-propanesulfonate (CHAPS, Anatrace), 0.1%(w/v) digitonin (Sigma Aldrich), 2 μM WIN 55,212-2 and 25 mU mL^{-1} apyrase for 2.5 h at 4℃. The supernatant was

isolated by centrifugation at 100,000 × g for 45 min and then incubated for 3h at 4℃ with pre-equilibrated 5mL FLAG resin. After batch binding, the FLAG resin with immobilized protein complex was manually loaded onto a gravity column (Bio-Rad). The resin was first washed with 10 column volumes of 20 mM HEPES, pH 7.2, 100 mM NaCl, 0.05% DDM (w/v), 0.01% CHS (w/v), 0.05% CHAPS, 0.1% digitonin(w/v), 2μM WIN 55,212-2. Detergent was then exchanged on resin by two washing steps in 20 mM HEPES, pH 7.2, 100 mM NaCl, 2μM WIN 55,212-2 supplemented with different detergents: first 0.02% DDM (w/v), 0.004% CHS (w/v), 0.02% CHAPS, 0.1% digitonin, then 0.1% digitonin for 10 column volumes each. Subsequently, the FLAG resin with bound material was gently resuspended in 20 mM HEPES, pH 7.2, 100 mM NaCl, 0.1% digitonin, 2μM WIN 55,212-2, treated with TEV protease and 2.5 mg scFv16 overnight at 4°C. Released protein from FLAG beads was collected the next day, concentrated and then loaded onto a Superdex 200, 10/300 GL increase column (GE Healthcare) pre-equilibrated with buffer containing 20 mM HEPES, pH 7.2, 100 mM NaCl, 0.075% digitonin, 2μM WIN 55,212-2. The eluted fractions of the monomeric complex were pooled and concentrated for cryo-EM grids preparation. The final yield of the purified complex is approximately 1mg per liter of insect cell culture.

Purification of scFv16

Purification of scFv16 was conducted as previously described (Koehl et al., 2018) with a subtle change. Briefly, secreted scFv16 from baculovirus-infected Sf9 insect cells was purified using Ni-NTA and size exclusion chromatography. After balancing the pH and removing the chelating agents by Ni^{2+} and Ca^{2+}, the cell culture supernatant was loaded onto Ni-NTA. The nickel resin was first washed with 20mM HEPES pH 7.2, 100mM NaCl, 50mM imidazole for 10 column volumes, and then eluted in buffer containing 250mM imidazole. The eluted sample was treated

with TEV protease (homemade) followed by dialysis in 20mM HEPES pH 7.2, 100mM NaCl overnight at 4℃ and then reloaded onto Ni-NTA resin to remove the cleaved octa-histidine tag. The flow-through was collected and applied to a HiLoad Superdex 200, 10/60 column (GE Healthcare). The monomeric peak fractions were concentrated and fast-frozen by liquid nitrogen.

Sample preparation and EM data collection

A droplet (3.0 μl) of the purified CB2-WIN 55,212-2-G_i-scFv16 complex at a concentration of about 7.0 mg ml^{-1} was applied to a glow-discharged holey carbon grid (Quantifoil R1.2/1.3, Au 300 mesh), and subsequently vitrified using a Vitrobot Mark IV (FEI Company). Cryo-EM movie stacks were collected on a Titan Krios microscope operated at 300 kV under EFTEM mode. Nanoprobe with a 0.9 μm illumination area was used. Data were recorded on a post-GIF Gatan K2 summit camera at a nominal magnification of 130,000, using a super-resolution counting model at a physical pixel size of 1.029 Å. BioQuantum energy filter was operated in the zero-energy-loss mode with an energy slit width of 20 eV. The total accumulative electron dose is ~83 e-/ $Å^2$ fractioned over 40 subframes with a total exposure time of 8 seconds. The target defocus range was set to -1.0 ~ -2.5 μm. A total of 8,810 image stacks were collected with two datasets.

Image processing and 3-D reconstructions

The movie stacks were corrected for drift and beam-induced motion by MotionCor2 [135] with 2× binning, which generated drift-corrected summed images with and without electron-dose weighting. Each micrograph was manually inspected to remove bad pictures that were contaminated by crystalline ice or other forms of visible contamination, and CTF parameters were estimated by CTFFIND4 [136] using non-dose-weighted images. After sorting, micrographs with maximum estimated resolution beyond 4.0 Å were discarded, and good motion-corrected summed images with dose-weighting were used for all other image processing in RELION 3.0 [137] and

cryoSPARC [138]. Global and local resolution estimates were calculated in RELION using the gold-standard Fourier shell correlation (FSC = 0.143) criterion [139]. About 3.5K manually picked parties were used to generate the auto picking 2D reference. The two datasets were performed auto picking and particle extraction, separately in RELION3.0. Particles extracted from each sub-dataset were 4 times downscaled and subjected to reference-free 2D classification to remove false picks and obvious junk classes leaving behind approximately 341,033 particles from dataset1 and 627,252 particles from dataset2 (Figure S2). The selected particles were re-centered and re-extracted for further 3-D processing. The initial model was generated in cryoSPARC (Figure S2) with re-extracted particles from dataset1. The totally good 968,288 particles were 3-D classified with 8 classes in RELION3.0 with 60 Å low pass filter of the initial model. Two good classes (~812k particles) were selected for another round of 3-D classification with CB2/G_i/scFv16 mask. A final set of 772k homogeneous CB2/G_i/scFv16 complex particles was selected to perform 3-D refinements in RELION3.0. The final model was refined to an overall resolution of 3.2 Å. The map was sharpened with a B-factor of −98 $Å^2$. Local resolution estimates were determined by ResMap software [140]. The final set of homogeneous CB2/Gi/scFv16 complex particles were also subjected to AHD focused refinement to generate a better map for AHD domain.

Model building and refinement

The initial G_i protein and scFv16 model were adopted from the cryo-EM structure of the μ-opioid receptor-G_i Protein complex (PDB: 6DDE), and the initial CB2 model was generated by an online homology model building tool [141]. All models were docked into the electron microscopy density map, followed by iterative manual adjustment and rebuilding in COOT [142], and real-space refinement using Phenix programs [143]. The model statistics were validated using Phenix Comprehensive validation [143]. Structural figures were prepared in Chimera and PyMOL

(https://pymol.org/2/). The final refinement statistics are provided in the Reagent and Resource Table. The extent of any model overfitting during refinement was measured by refining the final model against one of the half-maps and by comparing the resulting map versus model FSC curves with the two half-maps and the full model.

Protein thermostability assay

A fluorescence detection assay was conducted using the thiol-specific fluorochrome N-[4-(7-diethylamino-4-methyl-3-coumarinyl)-phenyl]-maleimide (CPM) to determine the thermal stability of CB2-G_i-scFv16 complex. The CPM reacts with the native cysteines embedded in the protein. CPM dye (Sigma Aldrich) was dissolved at 4 mg/mL in DMSO as stock and then diluted 1:40 with CPM dilution buffer containing 20 mM HEPES, pH 7.2, 100 mM NaCl. The protein (30–40 ng) was diluted in CPM dilution buffer supplemented with 0.1% digitonin to a final volume of 150μL. 10μL of the diluted dye was added and mixed with the protein sample gently. After incubation in ice for 10 min to allow full equilibration of the reaction system, the mixture was transferred into a sub-micro quartz fluorimeter cuvette (Starna Cells, Inc.). The melting curve was recorded by heating the mixture from 20°C to 90 °C with a ramp rate of 2 °C/min in a Cary Eclipse Fluorescence Spectrophotometer (Agilent Technologies). The excitation wavelength was set at 387 nm and the emission wavelength was 463 nm. Data analysis was performed by Prism 7 (GraphPad), Tm was determined by fitting the curve to the Boltzmann sigmoidal equation.

Synthesis and characterization of XIE55 and XIE57

(E)-N, N-diethyl-4-(((3,4,5- trimethoxybenzyl)imino)methyl)aniline (1)

3,4,5-Trimethoxybenzylamine (1972 mg, 10 mmol) was added slowly to a solution of 4-(diethylamino) benzaldehyde (1770 mg, 10 mmol) and methanol (20 mL). The reaction mixture was stirred and refluxed for 12 hours. The reaction mixture was cooled to room temperature, and

the solvent was removed by evaporation in vacuum to give the crude compound **1**, which was used in the next step without further purification.

N, N-diethyl-4-(((3,4,5-trimethoxybenzyl)amino)methyl)aniline (2)

The crude compound **1** was dissolved in methanol (20 mL), and $NaBH_4$ (570 mg, 15 mmol) was added. The mixture was stirred continuously for 12 hours at room temperature. The reaction solution was poured into water and extracted with ethyl acetate. The combined organic layers were washed with water and brine and then dried over Na_2SO_4. The residue was purified by flash chromatography (ethyl acetate/petroleum ether, 1:2) on silica gel to obtain the intermediate **2** used in the following steps.

(E)-N-(4-(diethylamino)benzyl)-2-phenyl-N-(3,4,5-trimethoxybenzyl)ethene-1-sulfonamide (XIE55)

XIE55 was prepared from the intermediate compound **2** (358 mg, 1.0 mmol) and (*E*)-2-phenylethene-1- sulfonyl chloride (202 mg, 1.0 mmol). The residue was purified by flash chromatography (ethyl acetate/petroleum ether, 1:2) on silica gel to obtain final product **XIE55**. White solid (278 mg, yield: 53%). m.p 95-97°C; ^{1}H NMR (400 MHz, DMSO-*d*6) δ7.65 (t, *J* = 2.4 Hz, 2H), 7.44–7.42 (m, 3H), 7.38 (s, 1H), 7.26 (s, 1H), 7.09 (d, *J* = 8.80 Hz, 2H), 6.59 (d, *J* = 8.40 Hz, 2H), 6.47 (s, 2H), 4.22 (s, 2H), 4.19 (s, 2H), 3.65 (s, 6H), 3.59 (s, 3H), 3.30–3.25 (m, 4H), 1.06 (t, *J* = 7.20 Hz, 6H). ^{1}H NMR (400 MHz, CDCl3) δ7.44 – 7.37 (m, 6H), 6.64 (d, *J* = 8.80 Hz, 2H), 6.56–6.502 (m, 3H), 4.28 (s, 4H), 3.85 (s, 3H), 3.82 (s, 6H), 1.18 (t, *J* = 6.80 Hz, 6H); ^{13}C NMR (600 MHz, CDCl3): δ 153.29, 147.54, 140.51, 137.37, 132.88, 131.88, 130.57, 130.47, 129.00, 128.05, 125.70, 121.63, 111.47, 105.55, 60.86, 56.10, 50.02, 49.85, 44.33, 12.54; MS (ESI): *m/z* 525.33 $(M + H)^+$.

N-(4-(diethylamino)benzyl)-N-(3,4,5-trimethoxybenzyl)thiophene-2-sulfonamide (XIE57)

XIE57 was prepared from the intermediate compound **2** (358 mg, 1.0 mmol) and thiophene-2-sulfonyl chloride (182 mg, 1.0 mmol). The residue was purified by flash chromatography (ethyl acetate/petroleum ether, 1:2) on silica gel to obtain final product **XIE57**. Yellow solid (270 mg, yield: 54%). m.p 77-80°C; ^{1}H NMR (400 MHz, DMSO-*d*6) δ 8.03–8.02 (m, 1H), 7.76–7.75 (m, 1H), 7.28–7.25 (m, 1H), 6.96 (d, *J* = 8.40 Hz, 2H), 6.55 (d, *J* = 8.80 Hz, 2H), 6.28 (s, 2H), 4.20 (s, 2H), 4.17 (s, 2H), 3.61 (s, 6H), 3.60 (s, 3H), 3.30–3.26 (m, 4H), 1.06 (t, *J* = 11.20 Hz, 6H); ^{13}C NMR (600 MHz, CDCl3): δ 153.06, 147.44, 141.71, 137.18, 131.72, 131.57, 131.33, 130.27, 127.28, 121.26, 111.36, 105.50(2C), 60.84, 56.00, 50.84, 50.73, 44.30, 12.52; MS (ESI): *m/z* 505.28 $(M + H)^{+}$.

CB2 radioligand competition binding assay

Nonradioactive ligands were diluted in binding buffer and supplemented with 10% dimethyl sulfoxide (DMSO) and 0.4% methylcellulose. Each assay plate well contained a total of 200 μL of reaction mixture composed of 5 μg of CB2 membrane protein, labeled [^{3}H] CP-55,940 ligand at a final concentration of 3 nM, and the unlabeled ligand at variable dilutions, as stated above. Plates were incubated at 30°C for 1 h with gentle shaking. The reaction was terminated by rapid filtration through Unifilter GF/B filter plates using a Unifilter Cell Harvester (PerkinElmer). After the plate was allowed to dry overnight, 30 μL of MicroScint-0 cocktail (PerkinElmer) was added to each well and the radioactivity was counted using a PerkinElmer TopCounter. All assays were performed in duplicate and data points were represented as mean ± SEM. Bound radioactivity data was analyzed for Ki values using nonlinear regression analysis via GraphPad Prism 7 software.

cAMP functional assay

Cellular cAMP levels were measured according to the reported method with modifications using LANCE cAMP 384 kits (PerkinElmer) [144, 145]. The assay is based on competition between a Europium-labeled cAMP trace complex and total cAMP for binding sites on cAMP-specific antibodies labeled with a fluorescent dye. CB_2 receptor wild type (WT)-transfected CHO cells were seeded into a 384-well white ProxiPlates with a density of 2000 cells per well in 5 μL of RPMI-1640 medium containing 1% dialyzed FBS, 25 mM HEPES, 100 μg/mL penicillin, 100 U/ml streptomycin and 200 μg/mL of G-418. After culture overnight, 2.5 μL of cAMP antibody and RO20-1724 (final concentration, 50 μM) in stimulation buffer (DPBS 1x, containing 0.1% BSA) was added to each well, followed by addition of either 2.5 μL compound or forskolin (final 5 μM) for agonist-inhibited adenylate cyclase (AC) activity assay. After incubation at room temperature for 45 min, 10 μL of detection reagent was added into each well. The plate was then incubated for 1 h at room temperature and measured in Synergy H1 hybrid reader (BioTek) with excitation at 340 nm and emission at 665 nm. Each cAMP determination was made via at least three independent experiments, each in triplicate. EC_{50} values were determined by nonlinear regression, dose-response curves (GraphPad Prism 7).

Quantitative characterization of binding residues on CB2

Ligand binding always involves its interaction with key binding residues, the changes in the features of ligand binding sites, particular rearrangements of the protein structure, etc. Thus, several key aspects of ligand binding can be explored quantitatively in a special binding region of a crystal/Cryo-EM structure, including the involved key residues, residual energy contribution, energy term, etc. Starting with the code base of the current stable version 2.2.3 of idock [146, 147] that adopts the exact scoring function of AutoDock Vina [148], we developed an even more

efficient variant integrating the ability to calculate also the residual contributions of the binding energy. Our adaptation skips the CPU-intensive precalculation of free energy grid map in the case of crystal/Cryo-EM structures with a ligand bound because the need for testing a massive number of conformational candidates is no longer there. Thereafter, the program populates the precisely calculated per-atom-pair free energy for every residue and produces the results. The improvement could reduce total time consumption by 95%~97% for most input. We will discuss this method in-depth in our future publications.

Molecular docking

The docking program Surflex-Dock GeomX (SFXC) in SYBYL-X 2.0 was applied to construct receptor-ligand complexes in which the docking scores were expressed in -log10 (Kd). The main protocols or parameters of docking were addressed in our previous publications [149, 150]. Briefly, the docking parameters used were as follows: (a) the "number of starting conformations per ligand" was set to 10, and the "number of max conformations per fragment" was set to 20; (b) the "maximum number of rotatable bonds per molecule" was set to 100; (c) flags were turned on at "pre-dock minimization," "post-dock minimization," "molecule fragmentation," and "soft grid treatment"; (d) "activate spin alignment method with density of search" was set to 9.0; and (e) the "number of spins per alignment" was set to 12.

Molecular Dynamics (MD) simulations

The MD simulation system consists of one copy of the human CB2 transmembrane domain and the WIN 55212-2 ligand, 240 POPC (1-palmitoyl-2-oleoyl-sn-glycero-3-phosphocholine) lipids, 0.15 M NaCl, and 17082 TIP3P [151] water molecules. The lipids, ions, and water molecules were added using CHARMM-GUI (www.charm-gui.org). The detailed force field set

up and MD protocol can be found elsewhere [152]. In brief, protein, lipid, and ligand are described by AMBER FF14SB [153] LIPID14 [154] and GAFF [155] force fields, respectively.

MD simulation was performed using the AMBER18 software package.[156] The MD system was first relaxed by a set of minimizations by removing possible steric clashes. There were three phases for the subsequent NPT (constant particle number, pressure, and temperature) MD simulations: the relaxation phase (1 nanosecond for each temperature from 50 to 250 K at a step of 50 K), the equilibrium phase (25 nanoseconds, 298 K), and the sampling phase (200 nanoseconds). 2000 snapshots were evenly selected from the sampling phase for MM-GBSA binding free energy decomposition analysis. The integration of the equations of motion was conducted at a time step of 1 fs for the relaxation phase and 2 fs for the equilibrium and sampling phases.

For each MD snapshot, the molecular mechanical (MM) energy (E_{MM}) and the MM-GB/SA solvation free energy were calculated without further minimization [157-159]. The interaction energies between each residue and the ligand were calculated with the solvent effect being taken into account using an MM-GBSA solvation model developed previously [160]. Key parameters controlling the MM-GBSA analyses were the following: external dielectric constant ~ 80; internal dielectric constant ~ 1; and the surface tension for estimating the nonpolar solvation energy ~ 0.005.

3.3 Experimental Results

3.3.1 Expression and purification of CB2-Gi complex

To obtain a stable complex of CB2 bound to WIN 55,212-2 and G_i, we co-expressed human CB2 with heterotrimeric G_i protein in insect cells (**Figure 2**). The receptor-G_i complexes were assembled on the membrane by incubation with WIN 55,212-2 and apyrase. In addition, the antibody fragment scFv16 was added to stabilize the nucleotide-free G_i complex by binding to the interface between $G\alpha_i$ and $G\beta$ [161]. The CB2-WIN 55,212-2-G_i-scFv16 complex was then purified through sequential steps of affinity chromatography to homogeneity, yielding a relatively thermostable complex suitable for single-particle cryo-EM analysis (**Figure 2**).

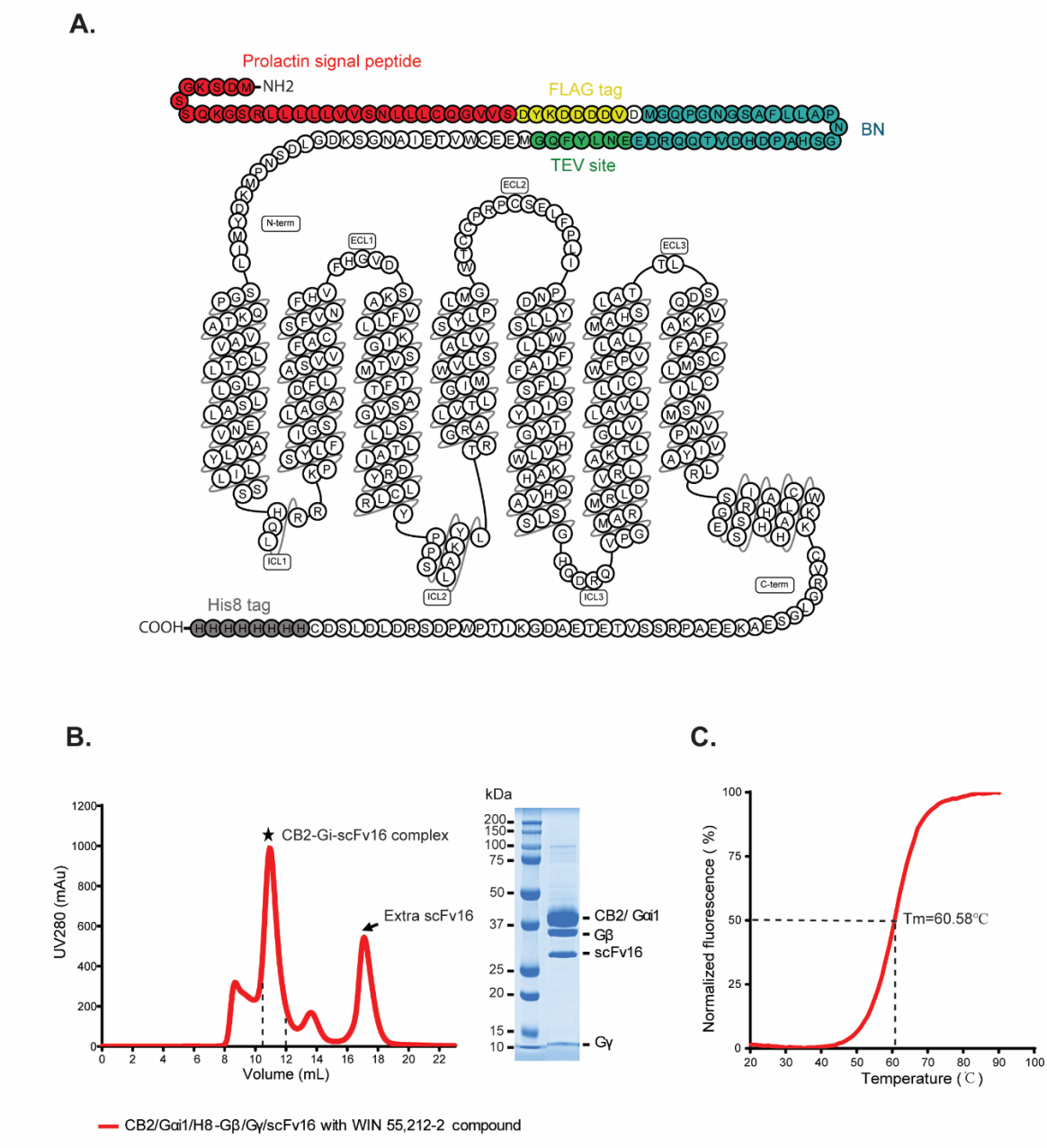

Figure 2. CB2 Construct and Complex Formation.

(**A**) Snake model of the CB2 constructs used in this paper. (**B**) Size exclusion chromatography profile and SDS-PAGE analysis of CB2-G_i-scFv16-WIN 55,212-2 complex; the peak of complex elution is marked with a star and the peak of extra scFv16 is marked with an arrow. Fractions between two dashed lines were pooled and concentrated for cryo-EM experiments. (**C**) CPM assay of CB2-G_i-scFv16 activated by WIN 55,212-2 to test the half denaturing temperature, Tm value. Tm was determined by fitting the curve to the Boltzmann sigmoidal equation.

3.3.2 Cryo-EM structure of CB2-Gi complex

The structure of the CB2-WIN 55,212-2-G_i-scFv16 complex (**Figure 3**) was determined from 772k particles to a nominal resolution of 3.2 Å (**Figure 4**), which allowed an unambiguous assignment of the TM domain of CB2, G_i protein, as well as the antibody fragment in the EM density maps (**Figure 5**). The α-helical domain (AHD) of $G\alpha_i$, which is poorly resolved in most cryo-EM GPCR-G protein complex structures, is resolved in our CB2-G_i complex structure with a relatively low resolution compared to that of the core structure of this complex. The overall structures were built by the rigid-body fit of an online homology building model [141]. Apart from the AHD of the G_i protein, the majority of the amino acid side chains were well resolved in the final models against the EM density map with excellent geometry.

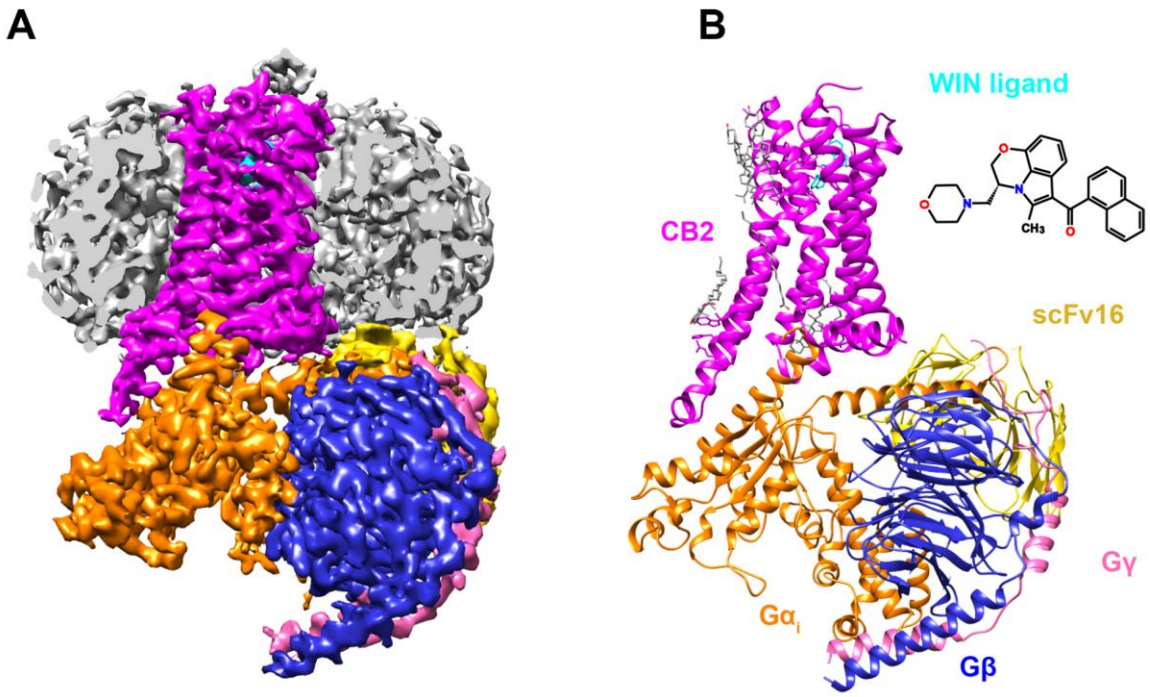

Figure 3. Cryo-EM Structure of CB2-Gi Coupling in Complex with WIN 55,212-2.

(**A**) Cut-through view of the cryo-EM density map of CB2-WIN 55,212-2-G_i-scFv16 complex. The unsharpened cryo-EM density map at 0.015 contour level shown as light gray surface indicates a micelle. The colored complex cryo-EM density map is shown at 0.022 contour level. (**B**) Cartoon representation of the CB2-G_i in complex with antibody scFv16 is shown with lipids in gray stick representation. Magenta, CB2; cyan, WIN-55,212-2; orange, $G\alpha_i$; blue, Gβ; pink, Gγ; gold, scFv16.

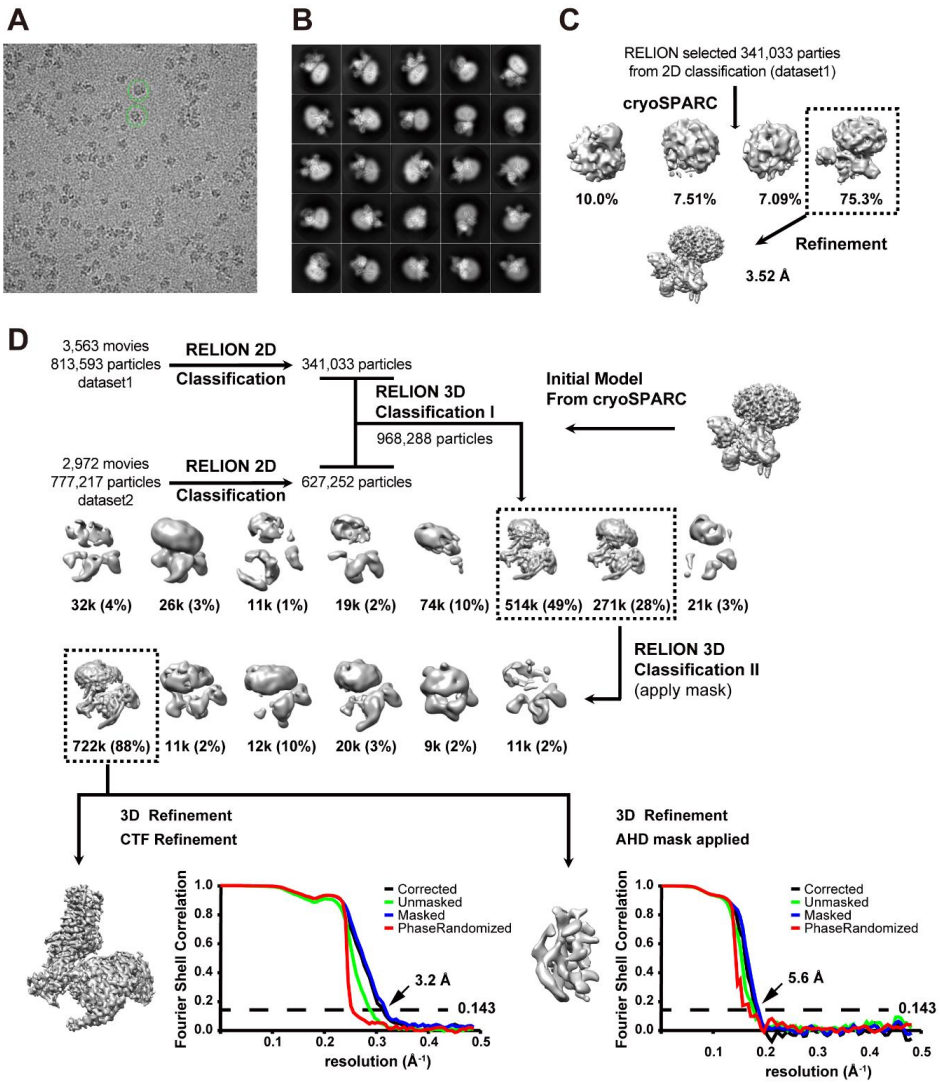

Figure 4. Cryo-EM data collection and structure determination

(A) Representative micrographs CB2-WIN 55,212-2-G_i-scFv16 complex with particles of 190 Å diameter highlighted in a green circle. (**B**) Representative images of 2D class-averages. (**C**) Cryo-electron microscopy data processing workflow by cryoSPARC to generate an unbiased Ab initio 3-D map. Boxed 3-D classes were selected for further processing. (**D**) Cryo-electron microscopy data processing workflow by RELION. Boxed 3-D classes were selected for further processing. Half-map Fourier Shell Correlation (FSC) plots generated by RELION was shown at the down right corner. An overall resolution was set at 3.2 Å at 0.143 FSC, and the α-helical domain (AHD) focused refinement at 5.8 Å at 0.143 FSC.

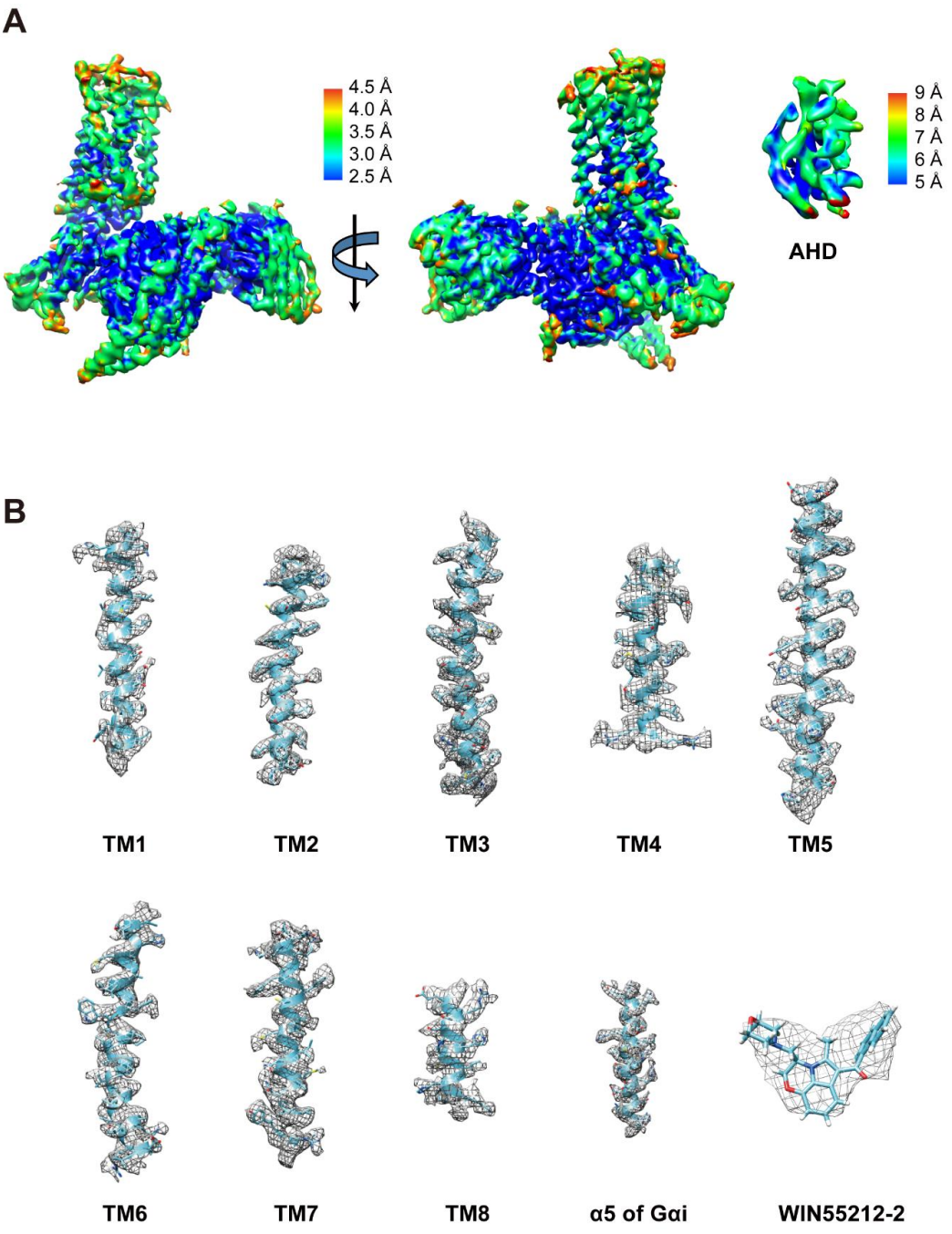

Figure 5. Cryo-EM Maps of CB2-Gi complex.

(**A**) Cryo-EM map colored according to local resolution, which was calculated from half-maps by ResMap software. The density map is shown at 0.022 contour level. (**B**) Density maps of TM1-8 in CB2/WIN 55,212-2, α5 of Gαi and WIN 55,212-2 ligand, showing at 0.016 contour level.

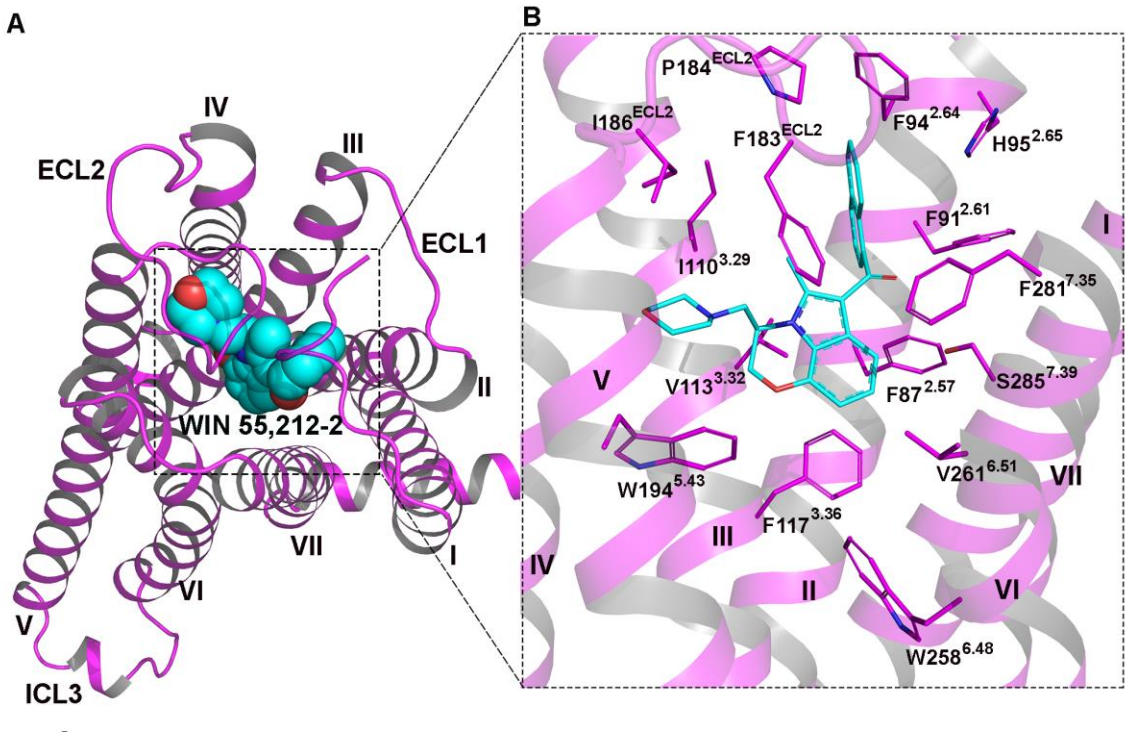

Figure 6. WIN 55,212-2 Binding in CB2 Orthosteric Ligand-Binding Site

(**A**) The overview of CB2 in complex with WIN 55,212-2. Cyan sphere model: chemical structure of WIN 55,212-2. Magenta cartoon: cryo-EM structure of CB2. (**B**) Detailed interactions of WIN 55,212-2 (cyan) within CB2 (magenta). The residues involved in the binding pocket of CB2 are mainly hydrophobic (magenta sticks) and are derived from TM2-TM3, TM5-TM7, and ECL2.

3.3.3 WIN 55,212-2 binding features

The EM density map shows the binding mode of the CB2 agonist WIN 55,212-2 in the orthosteric binding site in the TM domain of CB2. The orientation of the agonist was determined with both the electron density and the chemical and geometric constraints of the binding pocket of CB2 (**Figure 6**). To further validate the binding pose of WIN 55,212-2 in the ligand-binding pocket of CB2, we conducted molecular docking (**Figure 7A**) using three different software/algorithms: Schrödinger-Glide, Auto Dock, and SYBYL-Surflex Dock. The pose of WIN 55,212-2 depicted

in our complex structure (**Figure 7A**) was scored as the top one or two from all three algorithms, with the lowest binding energies. We also performed molecular dynamics simulation and the results showed that the pose of WIN 55,212-2 in the orthosteric ligand-binding pocket of CB2 is stable (**Figure 7B, 7C, and 7D**). The binding interface between WIN 55,212-2 and CB2 is also supported by previously reported mutagenesis-based and structural studies [133, 144, 162, 163].

As shown in **Figure 6**, the binding pocket of WIN 55,212-2, buried in the TM region, is formed by residues from TM2-TM3 and TM5-TM7 and capped by the extracellular loop 2 (ECL2). The naphthalene moiety of WIN 55,212-2 extends between TM2 and TM3 and is predicted to form strong π-π interactions with $F91^{2.61}$ and $F94^{2.64}$ and hydrophobic interactions with $F87^{2.57}$, $H95^{2.65}$, $P184^{ECL2}$, and $F281^{7.35}$. These results are consistent with the findings from Li et al. [133], who reported that $F87^{2.57}$, $F91^{2.61}$, $F94^{2.64}$, and $H95^{2.65}$ in TM2 are important for the recognition of CB2 antagonist AM10257. Furthermore, our cryo-EM data reveal that the core structure of WIN 55,212-2 (2,3-dihydro-[1,4]oxazino[2,3,4-*hi*]indole) points downward and engages in π-π interactions with $F117^{3.36}$ and $W258^{6.48}$. It also interacts with $I110^{3.29}$, $V113^{3.32}$, $F183^{ECL2}$, $V261^{6.51}$, and $M265^{6.55}$ via hydrophobic interactions, which have been shown previously to play key roles in the ligand binding of CB2. The morpholine moiety of WIN 55,212-2, which adopts the chair conformation, approaches TM5 and ECL2 to form additional hydrophobic interactions with critical residues that have been reported to function in ligand binding [149], including $F183^{ECL2}$, $I186^{ECL2}$, and $W194^{5.43}$.

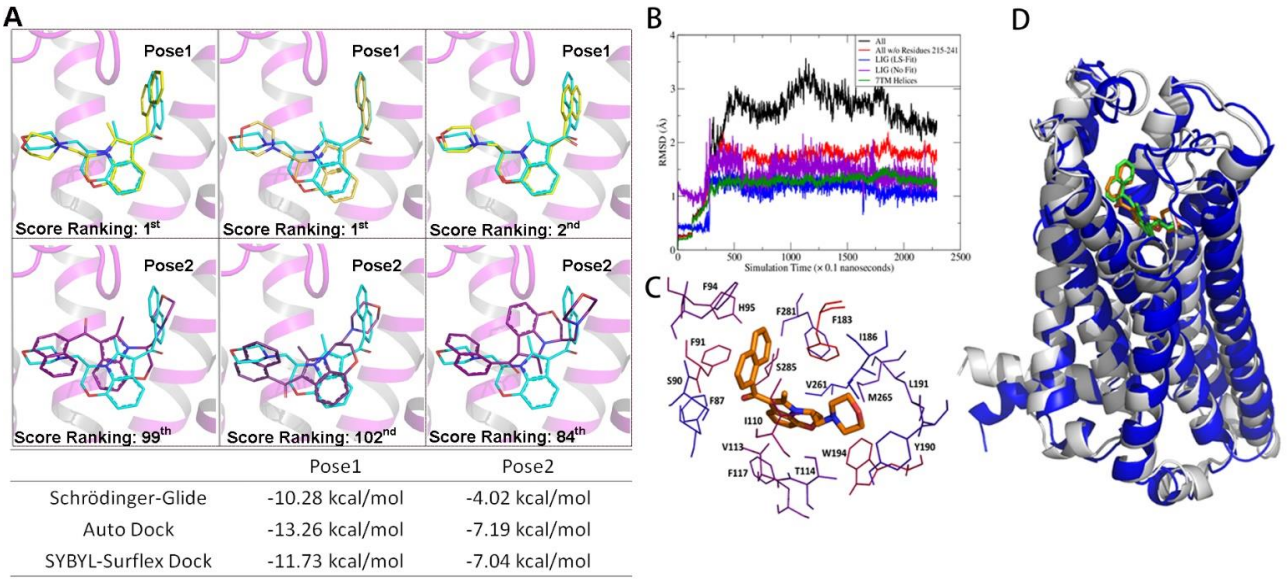

	Pose1	Pose2
Schrödinger-Glide	-10.28 kcal/mol	-4.02 kcal/mol
Auto Dock	-13.26 kcal/mol	-7.19 kcal/mol
SYBYL-Surflex Dock	-11.73 kcal/mol	-7.04 kcal/mol

Figure 7. Molecular Docking and Molecular Dynamics Simulations for the Transmembrane Domain (Residues 21-319)

(**A**) To further validate the binding pose of WIN 55,212-2, we first conducted molecular docking using three different software/algorithms, including Schrödinger-Glide (*left panels*), Auto Dock (*middle panels*), and SYBYL-Surflex Dock (*right panels*) to conduct the studies. All the docking results showed that the pose of WIN 55,212-2 presented in our manuscript (pose 1) ranked at the top one or two with the lowest energy (-10.28, -13.26, and -11.73 kcal/mol, respectively) compared to the alternative pose 2 (-4.02, -7.19, and -7.04 kcal/mol, respectively). (**B**) Root-mean-square deviation (RMSD) approximate time plots for all (black), all excluding the residues 215-241 loop (red), helices (green), a ligand with (blue) and without (purple) least-square fitting. (**C**) Hotspot residues identified by MM-GBSA decomposition. A residue is recognized as a hotspot when its interaction with the ligand is stronger than -1.0 kcal/mol. The hotspots residues according to their MM-GBSA interaction energies with the ligand are shown as brownish sticks. The stronger the interaction, the more reddish the residue is colored, while the weaker the interaction the more blueish the residue. (**D**) Representative MD structure (blue cartoon and brownish sticks), having the smallest RMSD to the average structure of MD snapshots, aligned to the Cryo-EM structure (grey cartoon and greenish sticks).

3.3.4 CB2 activation mechanism

WIN 55,212-2 shares a certain similarity with the antagonist AM10257 in binding to the receptor, but noteworthy differences also exist. From the structural alignment shown in **Figure 8A**, we may infer that AM10257 (antagonist) and WIN 55,212-2 (agonist) share a similar binding pocket and that most of the interactions with the receptor are conserved (**Figure 8A**). In addition, the volume of the WIN 55,212-2 binding site within active CB2 (~415 $Å^3$) is similar to that of the AM10257 binding site (antagonist, ~447 $Å^3$). One significant difference is that AM10257 (antagonist, orange sticks) inserts deeper (2.8 Å) into the binding pocket compared to WIN 55,212-2 (agonist, cyan sticks), which results in different conformations of the toggle switch residue $W258^{6.48}$. $W258^{6.48}$ is a highly conserved residue in class A GPCRs and has been reported to have a crucial role in GPCR activation [164]. In comparison to the inactive CB2, our data showed that $W258^{6.48}$ undergoes a 64° clockwise rotation and $F117^{3.36}$ endures a 10° counterclockwise rotation in the active CB2 (**Figure 8A and 8B**). We also note that the distance between $W258^{6.48}$ and WIN 55,212-2 is about 5.0 Å, greater than that observed for AM10257 (~3.8 Å). Therefore, the steric effects of CB2 ligands on $W258^{6.48}$ appear to play critical roles in determining ligand efficacy.

To further explore the role of critical residues on CB2 activation, we have calculated the individual residue energy contribution to determine how much certain residues contribute to the binding of WIN 55,212-2. Briefly, the total binding energy of WIN 55,212-2 at CB2 is the sum of intra-ligand free energy (the energy of WIN 55,212-2) and inter-ligand free energy (the energy between WIN 55,212-2 and residues in CB2), with the latter component further divided into energy contributions from each residue. We quantitatively calculated and compared the residual energy contributions between the inactive and active CB2. Although most of the residues contribute equally to the recognition of both antagonist-AM10257 (**Figure 8C**, green bars) and agonist-WIN

55,212-2 (**Figure 8C**, magenta bars), three residues, W194$^{5.43}$, F117$^{3.36}$, and W258$^{6.48}$, were found to potentially play important roles in distinguishing agonist from the antagonist. This occurs in a manner not requiring direct interaction since they are too far from the WIN 55,212-2 molecule to contribute significantly to its recognition as an agonist (**Figure 8C**). Several mutagenesis studies from our group and others [144, 162, 163] also provided evidence of the importance of these three residues in terms of WIN 55,212-2 binding and CB2 activation, further validating our residual energy contribution algorithm. This derivation aids in predicting how to design a functional agonist/antagonist pair based on a 3-D structure.

To further investigate and validate the structural findings, we rationally designed and synthesized two structurally related CB2-selective compounds and also measured the binding affinity Ki to CB1 and CB2, XIE55 (CB2 Ki=138 nM, CB1/CB2>1000) and XIE57 (CB2 Ki=639 nM, CB1/CB2>1000). They share the same pharmacophore but with different chemical moieties: XIE55 has a phenylethylene group whereas XIE57 has a thiophene ring (**Figure 9A and Figure 10**). Congruently, cAMP functional assays determined that XIE55 behaves as an inverse agonist, and XIE57 acts as a partial agonist of CB2. Molecular docking also showed that these two ligands adopt similar binding poses to interact with CB2 (**Figure 9C**). The most different feature is that agonist XIE57 does not extend sufficiently deep to constrain the conformation of W258$^{6.48}$ with a distance of 5.5 Å, while inverse agonist XIE55 approaches closer to W258$^{6.48}$ to form potentially strong π-π interactions (3.0 Å), which is consistent with our structural analysis of the action of WIN 55,212-2 and AM10257, addressed above. This pair of small molecules (XIE55 and XIE57) serves as a "proof-of-concept" of our method and investigation that can be applied by other researchers in the field for design and discovery of CB2 functional ligands.

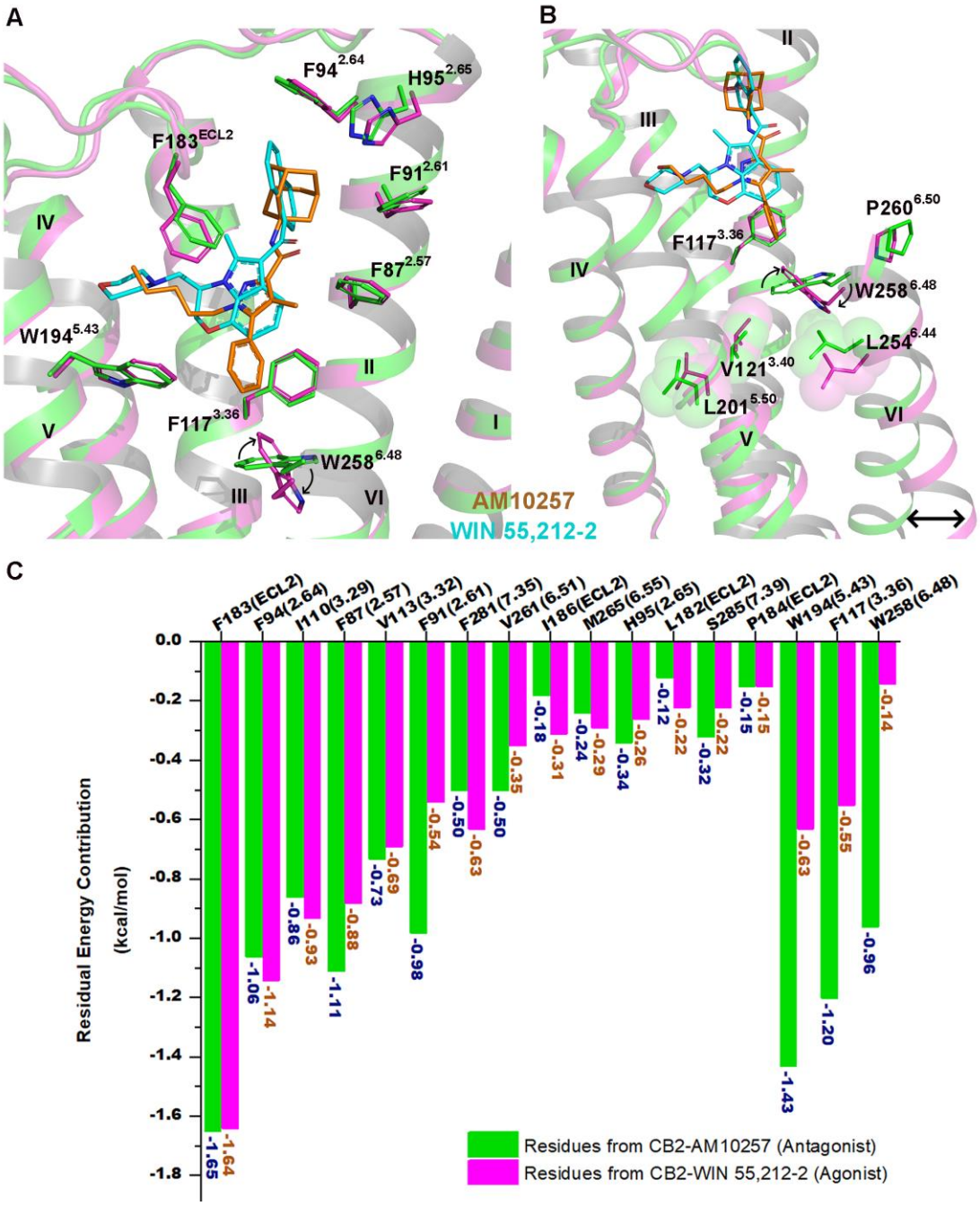

Figure 8. CB2 Activation by WIN 55,212-2

(**A**) Superposition of the WIN 55,212-2 (cyan)-activated CB2 (magenta) complex with antagonist (AM10257, orange)-bound CB2 receptor (green) (PDB: 5ZTY, resolution: 2.8 Å). (**B**) WIN 55,212-2 bound at the CB2 orthosteric pocket makes direct contacts with residues F117$^{3.36}$ and W258$^{6.48}$. The subtle rotation of F117$^{3.36}$ to interact with the 2,3-dihydro-[1,4]oxazino[2,3,4-*hi*]indole moiety of WIN 55,212-2 allows W258$^{6.48}$ to undergo a large rotation, with a

consequent outward movement of the cytoplasmic end of TM6 that serves to create a cavity for G protein binding. Green cartoon: the inactive CB2 crystal structure (PDB: 5ZTY, resolution: 2.8 Å). Magenta cartoon: the active CB2 cryo-EM structure. There is a relatively little rearrangement in residues V121$^{3.40}$, L201$^{5.50}$, and L254$^{6.44}$, different from the corresponding residue Pro$^{5.50}$ of β_2AR and μOR, which is involved in packing interactions with Ile$^{3.40}$ and Phe$^{6.44}$ during the activation of these GPCRs. (**C**) The energy contribution of key residues involved in the binding pockets of inactive and active CB2. Green bars: calculated energy contributions of key residues based on the inactive CB2 crystal structure (PDB: 5ZTY). Magenta bars: calculated energy contributions of key residues using the active CB2 cryo-EM structure.

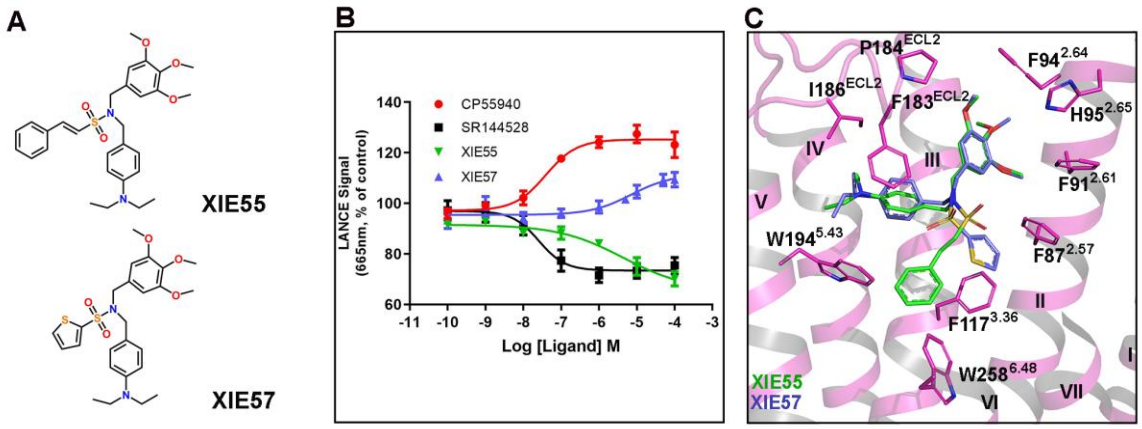

Figure 9. Pharmacology and Molecular Docking of the Designed CB2 Agonist and Antagonist

(**A**) Chemical structures of the rationally designed antagonist XIE55 and agonist XIE57. (**B**) XIE57 acts as a CB2 agonist while XIE55 behaves as a CB2 antagonist, as determined by cAMP assay. The dose-response curves for CP55940, a known agonist, and SR144528, a known inverse agonist, are also shown. CP55940 EC_{50}: 45.5 ± 24 nM, K_i: 1-2 nM; SR144528 EC_{50}: 10.5 ± 4.5 nM, K_i: 0.6 nM; XIE57 EC_{50}: 6.9 ± 2.9 μM, K_i: 639 nM; XIE55 EC_{50}: 1.5 ± 0.4 μM, K_i: 138 nM. Data are presented as mean ± SEM of at least 3 experiments performed in duplicate. (**C**) The docking of XIE55 and XIE57 in WIN 55,212-2-bound CB2 structure (WIN 55,212-2 is removed).

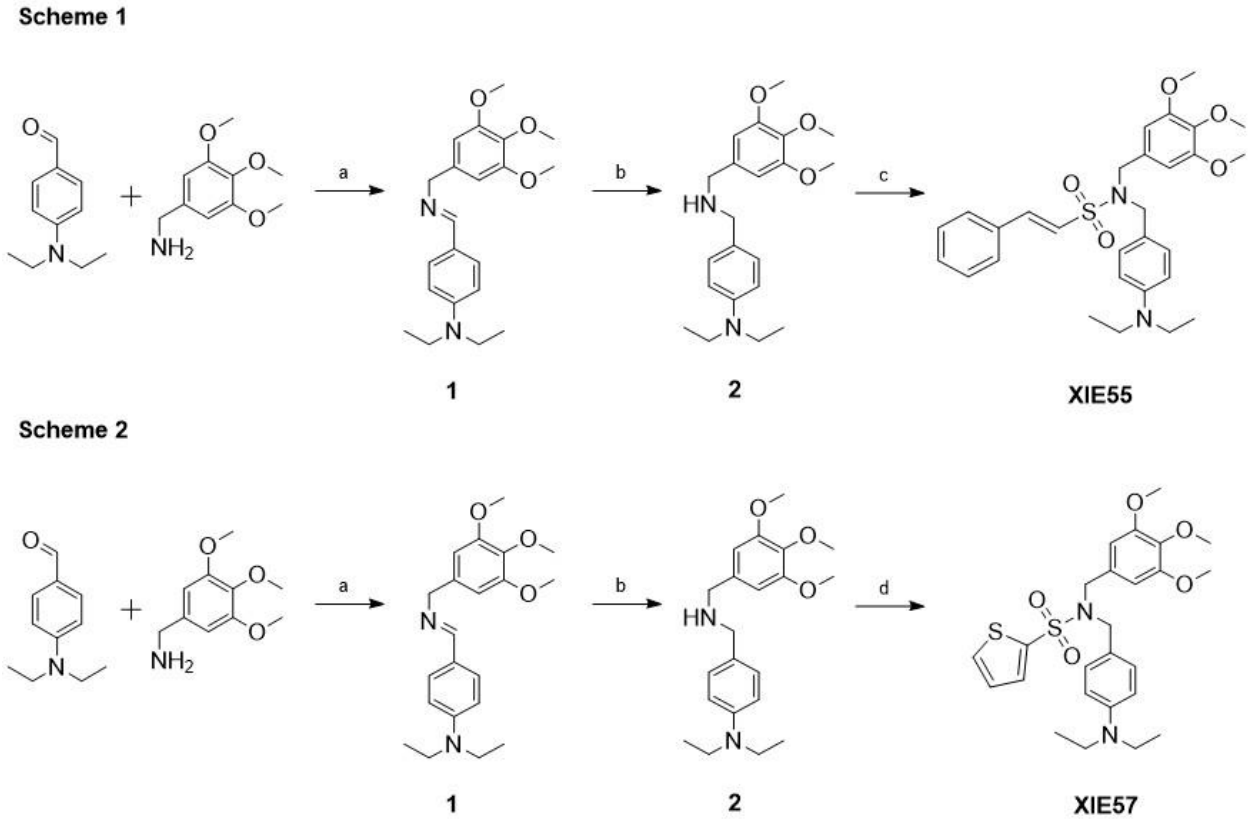

Figure 10. Synthesis of XIE55 (Scheme 1) and XIE57 (Scheme 2), Related to Figure 3C, 3D, and 3E.

Reagents and conditions: (a) Methanol, 70°C reflux. (b) NaBH4, room temperature. (c) TEA, DCM, (E)-2-phenylethene-1- sulfonyl chloride, room temperature. (d) TEA, DCM, Thiophene-2-sulfonyl chloride, room temperature

3.3.5 Comparison of the CB1/CB2 activation mechanism

In order to explore the differences in receptor activation between CB2 and CB1, we aligned the agonist-bound CB2-G_i and agonist-bound CB1-G_i complexes. Although the two ligands, WIN 55,212-2 and MDMB-Fubinaca (FUB), overlap very well, the critical "toggle switch" residues $W^{6.48}$ and $F^{3.36}$ show differences. Specifically, $W356^{6.48}$ in CB1 is positioned about 2.3 Å up towards the extracellular surface, and $F200^{3.36}$ in CB1 is rotated 68° compared to the analogous **Figure 11A** residues in CB2 (**Figure 11A**). As a result, the distance between $W356^{6.48}$ and $F200^{3.36}$

in CB1 (4.8 Å) is longer than that in CB2 (3.4 Å). Similarly, the different arrangement of the "toggle switch" causes a 74° counterclockwise rotation of F202$^{5.51}$ in TM5 of CB2 in comparison to the corresponding residue L287$^{5.51}$ in CB1. Other residues involved in the orthosteric binding in CB receptors, especially those from TM2 and ECL2, show some conformational differences as well (). Interestingly, the conformation and position of ECLs remain largely unchanged during receptor activation, which can likely be attributed to the C174-C179 disulfide bond and a rigid motif of "PXP" (P176 and P178). We also observed modest upward shifts of residues on the cytoplasmic ends of TM5 and TM6 of CB2 relative to those of CB1 (**Figure 11B**), which leads to a shift of Y$^{7.53}$ in the NPXXY motif away from Y$^{5.58}$ and L$^{6.41}$ in CB2 compared to that in CB1. Such structural differences in the ligand-binding pockets are associated with observed differences in the conformation of TM5 and TM6 and the G_i coupling interface between CB1 and CB2, indicating the activation mechanisms of CB1 and CB2 are not the same. All these structural alterations may be also associated with the distinct interactions of G-proteins between CB1 and CB2.

3.3.6 CB1/CB2 selectivity

To compare the selectivity between CB2 and CB1, we conducted molecular docking studies and calculated the residual energy contribution for GW-405,833 (L-768,242) on active CB2 and inactive CB1 (PDB: 5TGZ) [165]. GW-405,833, a dual functional compound [166] , acts as a highly selective partial agonist on CB2 (Ki= 3.92 ± 1.58 nM) but as an antagonist on CB1 (Ki= 4772 ± 1676 nM). The docking poses of GW-405,833 on these two receptors are quite different, as shown in **Figure 12A**. Moreover, the binding energy of GW-405,833 on CB2 (-10.83

kcal/mol) is greater than that on CB1 (-6.66 kcal/mol), which is consistent with the reported binding affinities for CB2 and CB1. Sequentially, the residual energy contributions for GW-405,833 binding on both CB2 and CB1 were calculated and compared (**Figure 12B**). Several residues on inactive CB1, including P102 (N-terminus), M103 (N-terminus), I105 (N-terminus), $F170^{2.57}$, and $W356^{6.48}$, are important for GW-405,833 binding. In particular, $W356^{6.48}$ on CB1 contributes greatly (-0.94 kcal/mol) to the recognition of GW-405,833 as an antagonist. However, the energy contribution of the corresponding residue $W258^{6.48}$ on CB2 for partial agonist GW-405,833 is -0.15 kcal/mol (**Figure 12B**), which is similar to that for WIN 55,212-2. Importantly, $L182^{ECL2}$, $F183^{ECL2}$, $P184^{ECL2}$, and $I186^{ECL2}$ from ECL2 show greater contributions to the binding of GW-405,833 on CB2 than the corresponding residues on CB1 (**Figure 12B**), supporting findings from previous studies [167].

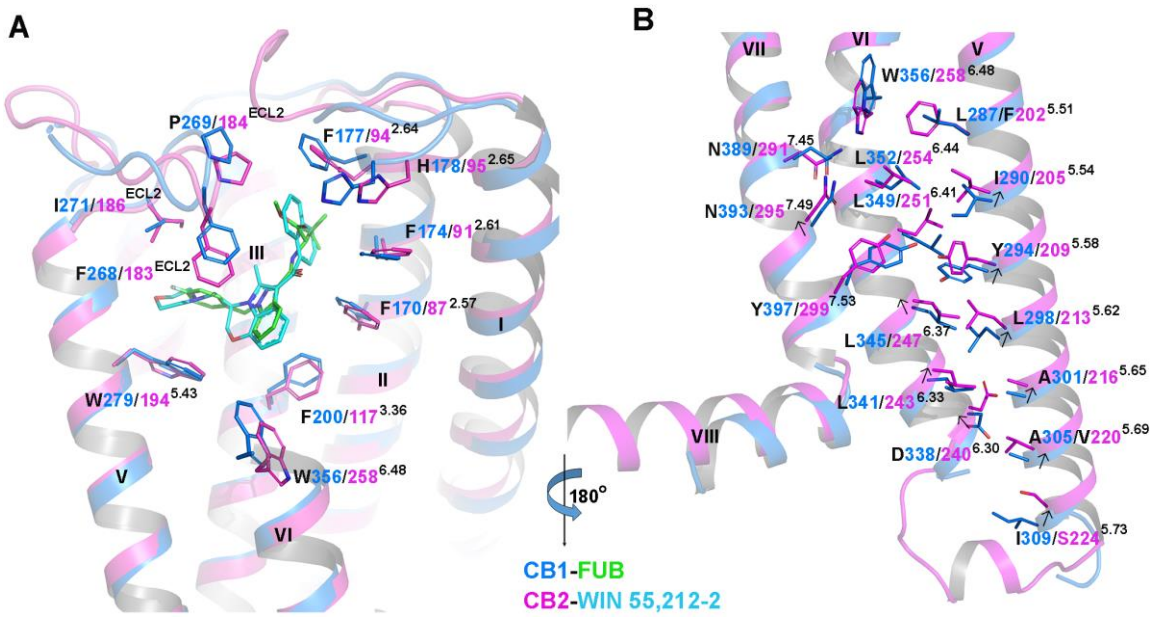

Figure 11. Structure Difference Between Agonist-bound CB2 and Agonist-bound CB1.

(**A**) A comparison of binding pockets between CB1-G_i and CB2-G_i complexes. Marine cartoon: the CB1 structure (PDB: 6N4B, resolution: 3.0 Å). Magenta cartoon: the CB2 structure. Green sticks: MDMB-Fubinaca. Cyan sticks: WIN 55,212-2. (**B**) Residue arrangements in the cytoplasmic end of TM5/TM6/TM7 between CB1-G_i and CB2-G_i structures. Marine cartoon: the CB1 structure (PDB: 6N4B, resolution: 3.0 Å). Purple cartoon: the CB2 structure. Arrows indicate the movements of residues from CB1 to CB2.

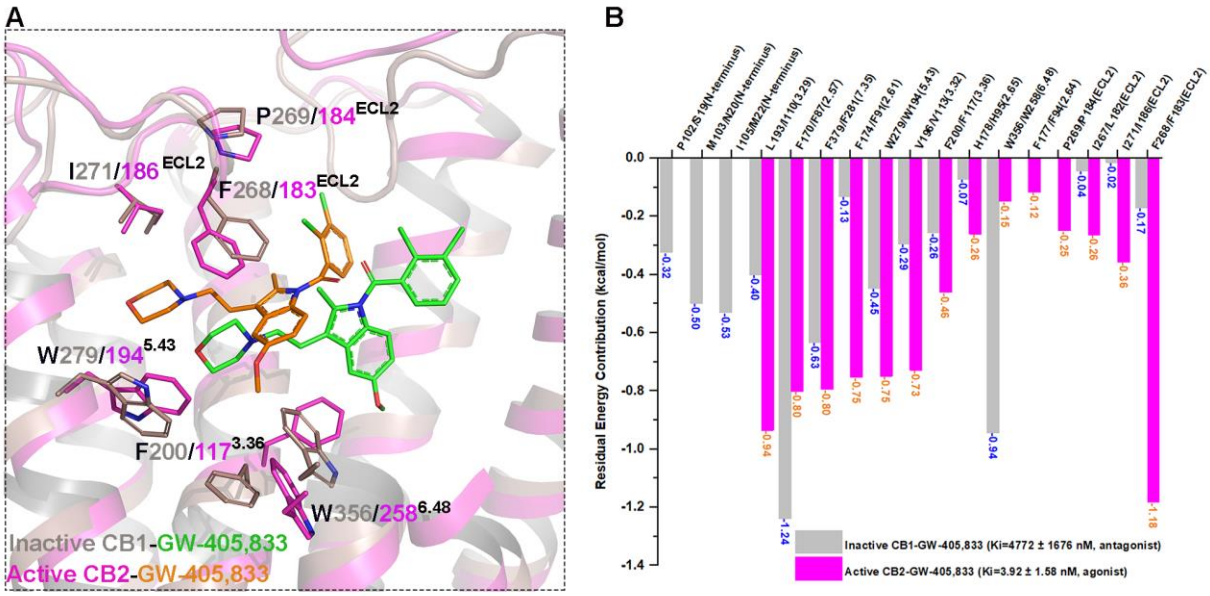

Figure 12. Comparison of Docking Results of CB2 Selective Partial Agonist GW-405,833 (L-768,242) on Active CB2 and Inactive CB1.

(**A**) Comparison of docking poses and detailed interactions of CB2 selective partial agonist GW-405,833 on active CB2 (magenta) and inactive CB1 (gray, PDB: 5TGZ). It is reported that GW-405,833 acts as CB2 agonist (Ki=3.92 ± 1.58 nM) and CB1 antagonist (Ki=4772 ± 1676 nM). (**B**) Comparison of residual energy contribution on GW-405,833 between active CB2 (magenta bars) and inactive CB1 conformations (gray bars).

3.3.7 CB2-Gi coupling and G protein selectivity

The overall cryo-EM structure of the CB2-G_i complex reveals a similar interaction mode between the receptor and G protein compared to other G_i/G_s-coupled receptors (**Figure 13**). The C-terminal α5 helix of the $G\alpha_i$ subunit inserts into the cavity at the cytoplasmic site of CB2 to form the major interaction interface with residues from TM2, ICL2, TM3, TM5, and TM6 of the receptor. When aligned with the reported μ-opioid receptor (μOR)-G_i (PDB: 6DDE) and β_2-adrenergic receptor (β_2AR)-G_s (PDB:3SN6) complexes [168], the α5 helix in CB2-G_i is rotated by 18° and 14°, respectively, along the axis of the membrane (**Figure 13A and 13B**). However,

several striking differences of G_i protein coupling between CB2 and CB1 can be observed. For example, the N-terminus of the α5 helix of $G\alpha_i$ in CB2-G_i is closer to TM5 (**Figure 14A**) and inserts deeper into the receptor-binding cavity than those in Rhodopsin-G_i (PDB: 6CMO)[169] and CB1-G_i (PDB: 6N4B)[133] complexes, as pointed out above. As a result, CB2 forms a more extensive hydrogen-bonding network with the α5 helix of $G\alpha_i$ than that found in the structure of CB1-G_i (**Figures 14B and 14C**). Specifically, compared to the five hydrophilic interactions between CB1 and $G\alpha_i$ [133], eight pairs of hydrogen bonds can be observed between CB2 and α5 helix (**Figure 13B**). $K67^{2.37}$ and $S69^{2.39}$ in the intracellular side of TM2 are observed to form hydrogen bonds with D350 and C351 in α5 helix, respectively. $K142^{ICL2}$ in ICL2 interacts with both N347 and D350 via strong hydrogen bond interactions. $R131^{3.50}$, a residue of the "ionic lock" in TM3 also forms a hydrogen bond with C351. In addition, $H219^{5.68}$ and $H226^{5.75}$ in TM5 approach D341 and D337 in α5 to form two hydrogen bonds. Finally, we also observed a hydrogen bond between $R242^{6.32}$ and F354. In contrast to CB1, ICL3 in CB2 is well-structured and directly interacts with G_i. As shown in **Figure 14D**, an additional α-helix is formed by residues from ICL3 and TM6 including $R229^{ICL3}$, $Q230^{ICL3}$, $V231^{6.21}$, and $P232^{6.22}$. Two polar residues from ICL3, $Q227^{ICL3}$, and $R229^{ICL3}$, form additional hydrogen bonds with Q304 and E297 of $G\alpha_i$, which are absent in the CB1-G_i complex (**Figure 15**).

Although CB1 and μOR primarily signal through the $G_{i/o}$ family, previous studies suggested that they can also couple to G_s [170]. However, CB2 does not couple to the G_s family. On the other hand, ICL2 point mutations P139F, P139M, or P139L allows CB2 to couple to G_s in a CRE-driven luciferase assay [171]. Moreover, a CB2 P139L mutant could activate ERK through both G_i- and G_s-mediated pathways [171]. Interestingly, when L222 of CB1 (corresponding to P139 of CB2) is mutated to proline, G_s coupling is lost but coupling to G_i is retained [172]. These

studies, together with previous cross-linking studies [173], suggest an important role of $P139^{ICL2}$ in the G protein selectivity and coupling for CB2.

In our cryo-EM structure, $P139^{ICL2}$ in CB2 interacts with L194 in the β2-β3 loop of G_i but is away from the hydrophobic pocket formed by L194, I343, T340, and F336 in G_i (**Figure 14E**). It has been suggested that for CB1, the corresponding residue of $P139^{ICL2}$ in CB2, $L222^{ICL2}$ (**Figure 14F**), may engage a similar hydrophobic pocket when coupled to G_s, which is important for G_s recognition [170]. However, the $P139^{ICL2}$ in CB2 may not permit interactions with the hydrophobic pocket in G_s due to the rigid motif of "$P138^{ICL2}P139^{ICL2}$" motif, leading to the high selectivity of CB2 for G_i over G_s. Consistently, mutation of CB2 $P139^{ICL2}$ to bulkier residues, such as Phe or Leu, might allow such coupling interactions with G_s to be regained.

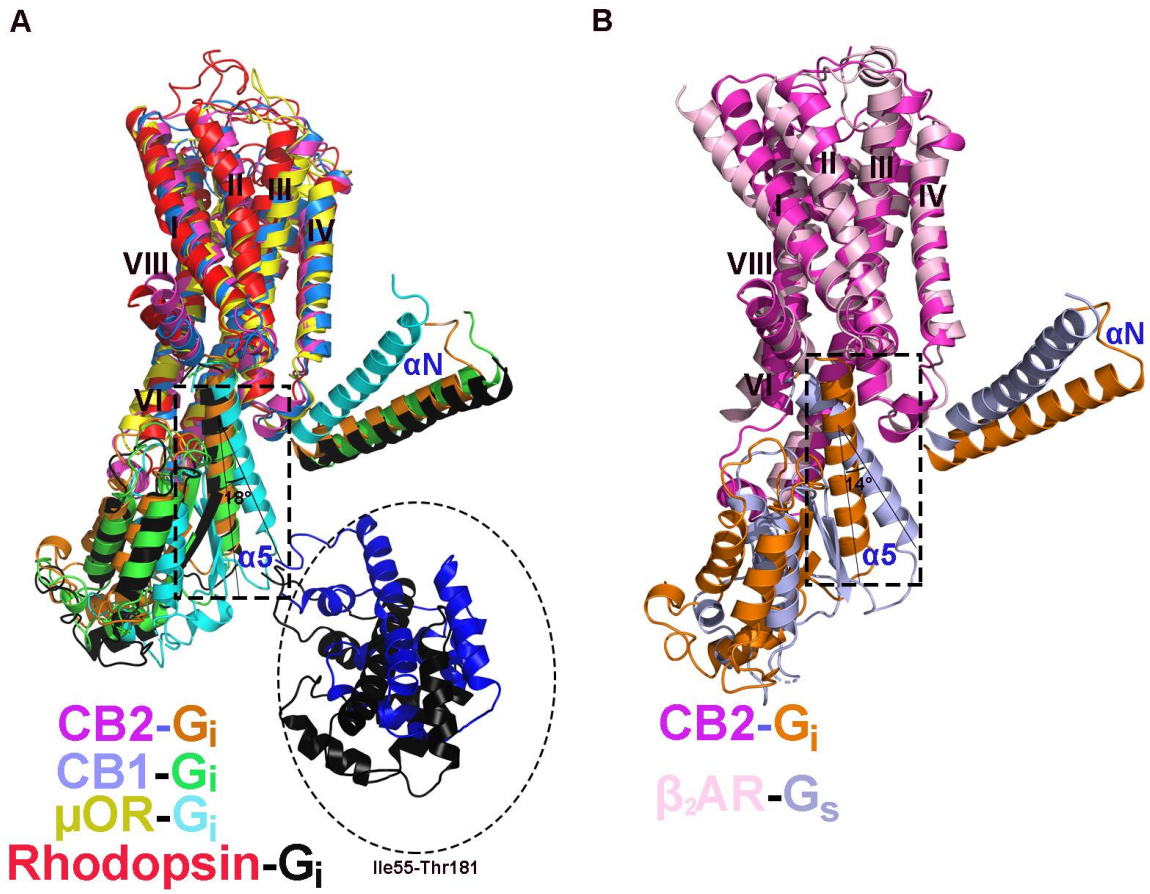

Figure 13. Relative Orientation of CB2 and Gi

(A) Comparison of the relative orientations of Gi bound to CB2 (magenta), CB1 (PDB: 6N4B, marine), μOR (PDB: 6DDE, yellow), and Rhodopsin (PDB: 6CMO, red) when aligned on the receptor. (B) Comparison of CB2-Gi complex with β2AR-Gs complex (PDB:3SN6, light pink) when aligned with the receptor.

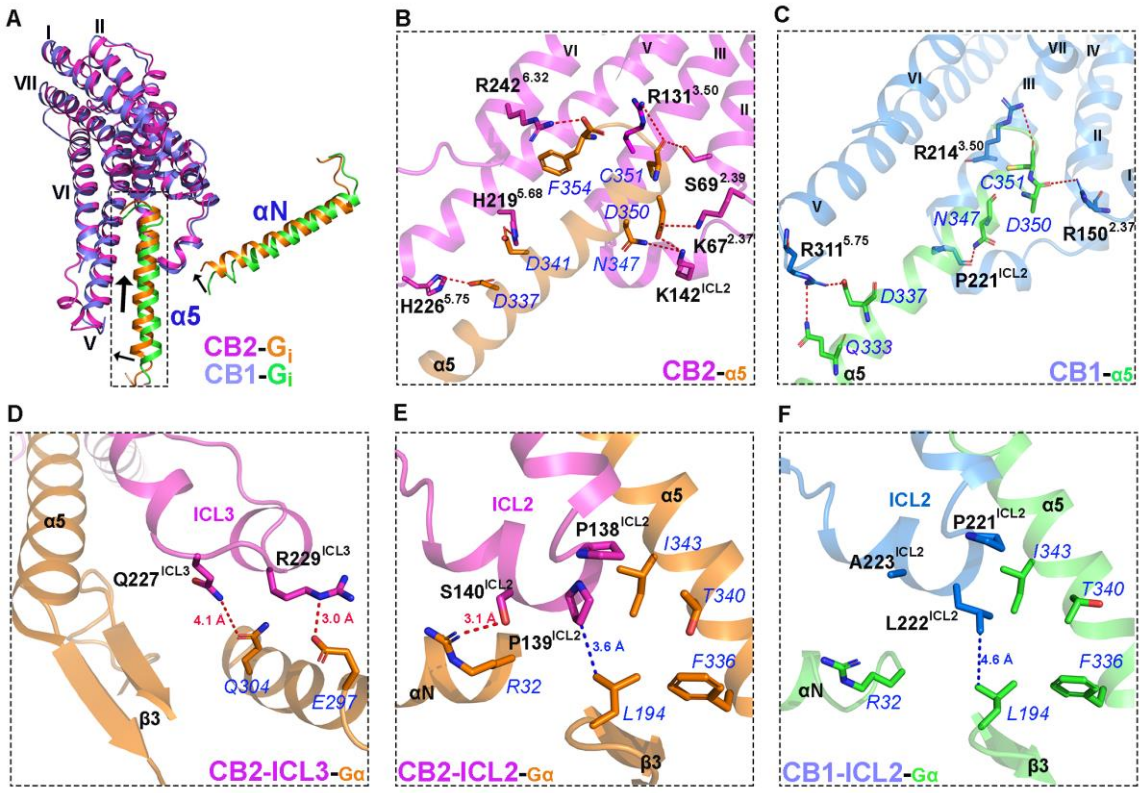

Figure 14. Comparison of the Interface between CB2 and Gα as well as CB1 and Gα.

(**A**) Overlay of CB2 or CB1 and G_i-α5 structures. Marine cartoon: the CB1 structure (PDB: 6N4B, resolution: 3.0 Å). Purple cartoon: the CB2 structure. Orange: G_i-α5/G_i-αN protein of CB2. Green: G_i-α5/G_i-αN protein of CB1. (**B**) The hydrogen bond network in the complex of CB2-Gα. Magenta cartoon: the CB2 structure. Orange: Gα protein. Residues from α5 are highlighted in blue font. The residues belonging to CB2 are highlighted in black font. (**C**) The hydrogen bond network in the complex of CB1-Gα. Marine cartoon: the CB1 structure (PDB: 6N4B, resolution: 3.0 Å). Green: Gα protein. Residues from α5 are highlighted in blue font. The residues belonging to CB1 are highlighted in black font. (**D**) Detailed interactions between ICL3 of CB2 and Gα. Magenta cartoon: the CB2 structure. Orange: Gα protein. The hydrogen bonds are highlighted by red dash lines. (**E**) Interactions between ICL2 of CB2 and Gα. Magenta cartoon: the CB2 structure. Orange: Gα protein. The hydrogen bond is highlighted by a red dash line. The hydrophobic interaction is represented by a blue dash line. (**F**) Interactions between ICL2 of CB1 and Gα. Marine cartoon: the CB1 structure. Green: Gα protein. The hydrophobic interaction is represented by a blue dash line.

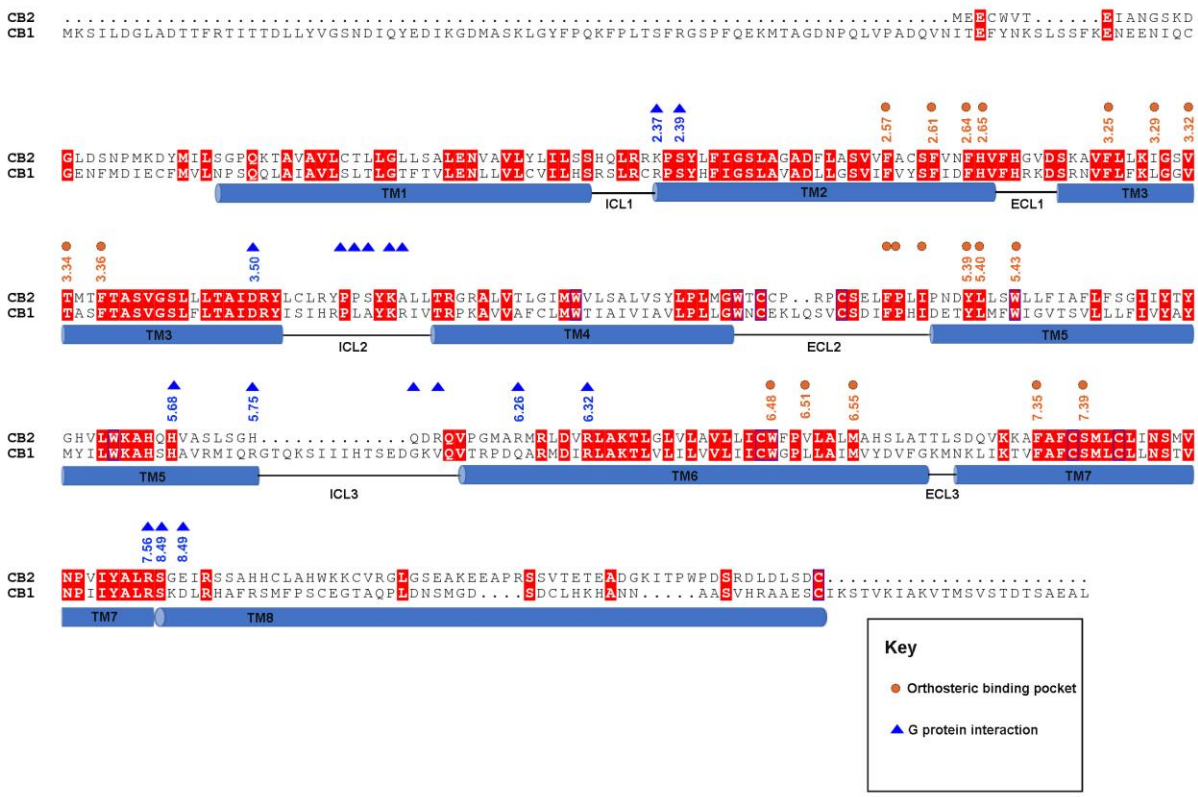

Figure 15. Common Mechanism of CB2 Activation and G Protein Coupling.

Sequence alignments between CB2 and CB1 highlight the orthosteric binding pocket residues and the TM6 kink residues for receptor activation, as well as the G_i-interface residues for G_i coupling. Secondary structure elements are annotated underneath the sequences.

3.4 Discussion and Conclusion

Delineating the CB2 structural basis for ligand recognition and G protein recruitment will facilitate the rational design and development of drugs with high affinity and selectivity, as well as optimal therapeutic effects. Here, we first discovered the cryo-EM structure of an agonist-bound CB2-G_i signaling complex, and the detailed interactions between the potent agonist WIN 55,212-2 and the receptor, the key residues determining ligand selectivity and efficacy, the differences of

activation mechanisms between CB2 and CB1, and the unique molecular features of the CB2-G_i protein interaction.

Our 3-D cryo-EM structure of CB2 reveals that WIN 55,212-2 occupies the same orthosteric binding pocket as antagonist AM10257 in CB2 and stabilizes the CB2-G_i complex in its active conformation through interference with the "toggle switch" residue $W258^{6.48}$, which is critical for distinguishing agonists from antagonists. ECL2 and residues from TM2, TM3, and TM6 play important roles in CB2 ligand recognition and ligand selectivity. This provides an advanced strategy for the rational design of CB2 selective agonists. The divergent conformation of $W^{6.48}$ in CB1 versus CB2 is associated with a series of distinct residue rearrangements in the intracellular side of TM5, TM6, and TM7 of CB2, as addressed above, which distinguish the activation/ G_i signaling mechanism of CB2 from that of CB1. While several novel synthetic CB2-selective agonists, including thiophene-containing compounds, have recently been reported [174-178], few have entered clinical trials and none have yet been approved by the FDA. The results presented herein are likely to aid in the development of potent and selective CB2 ligands with clinical therapeutic potential.

Comparison of the CB2-G_i complex with CB1-G_i, Rhodopsin-G_i, μOR-G_i, and β_2AR-G_s complexes reveals certain similar overall interaction profiles for receptor-G protein binding. Although CB2 and CB1 share a great structural similarity, their interactions with the α5 helix of the G protein remain distinct, reflecting the versatility of G_i coupling. $P139^{ICL2}$ in CB2 and the homologous residue in other GPCRs are critical for G protein coupling, and the unique motif of "$P138^{ICL2}P139^{ICL2}$" in ICL2 of CB2 contributes to its G_i coupling specificity. The well-resolved ICL3 structure provides detailed information relating to CB2 interaction with the G protein. Our findings in this Chapter, along with the published CB1 structures and CB2 inactive structures,

fulfill the complete profile of cannabinoid system receptors and should aid in the rational design of drugs targeting CB2.

4.0 CB2 Structures Characterization with Functional Ligand and Allosteric Modulators

4.1 Research Background

Activation of CB2 carries out downstream signaling by coupling with $G_{i/o}$ or G_q protein, recruiting β-arrestin1/2, inhibiting cAMP formation, activating GIRK channel, decreasing Ca^{2+} influx, etc. G_i coupling and β-arrestin recruitment are two direct downstream signals of CB2 activation that provoke the activity of multiple effectors. Specifically, the recruitment of $G_{\alpha i/o}$ leads to the inhibition of adenylyl cyclase (AC) and causes the down-regulation of cAMP levels [179]. The $G_{\beta\gamma}$ subunits that dissociated from $G_{\alpha i/o}$ are responsible for the inhibition of voltage-gated calcium channels (VGCC) and the activation of GIRKs and phosphatidylinositide-3-kinase (PI3K) [180]. In contrast, the β-arrestin2 recruitment upon CB2 activation has been demonstrated to be physiologically linked to the internalization and desensitization process of CB2 [181, 182]. Additionally, it is reported that the recruitment of β-arrestin1 to the 2-AG activated and internalized CB2 on endosome will lead to ERK1/2 phosphorylation [183]. Although the β-arrestin mediated CB2 signaling pathways are not well studied, functional selectivity of many other GPCRs including opioid receptors, β-adrenergic receptors, angiotensin receptors, dopamine receptors, etc. are well characterized. Some biased agonist/antagonists with better efficacy such as Carvedilol and Fenoterol that target β-adrenergic receptors have also been identified, which shows the significance of developing novel biased ligands [184]. Notably, upon the activation of the μ-opioid receptor, morphine will produce less tolerance, dependence, constipation, and respiratory suppressive side effects in the absence of β-arrestin2. Moreover, a significantly enhanced and prolonged analgesic effect of morphine was observed in loss-of-function of β-arrestin2 [185].

Thus, it is believed that selectively targeting the G_i signal pathways over β-arrestin pathways will mitigate the internalization and desensitization of CB2, which will provide huge opportunities in terms of CB2 drug development. Currently, there is no such CB2 biased ligand in the market nor clinical trials, and there are very few synthetic CB2 ligands that can be identified as CB2 biased ligands.

While efforts devoted to developing therapeutic synthetic cannabinoids binding to the orthosteric site [186, 187], these have had limitations of poor selectivity, lack of efficacy, or resistance or decreased efficacy upon chronic administration [188-190]. On another hand, GPCRs have been reported to also possess allosteric binding sites, which are topologically and functionally distinct from the orthosteric binding site of the same receptor. Allosteric modulators permit specific interactions between ligands and receptors that are typically under less evolutionary pressure for conservation within a receptor family [187, 191, 192].

However, a highly resolved 3-D structure of CB2 with an allosteric modulator has remained elusive, which hindered the development of novel CB2 allosteric modulators. **Figure 16** shows the current available CB2 modulators. Among them, pepcan-12 is an endogenous ligand, TBC, and DHGA are from the plant. Only C2 is reported to be the first CB2 synthetic small-molecule modulator. Thus, it is important to use our 3.2 Å cryo-EM elucidation of 3-D agonist-bound human CB2/Gi complex [193] to probe the active CB2 structure by using our integrated computational and experimental medicinal chemistry biology approaches, to determine CB2 allosteric binding pockets, and then to design and synthesize novel allosteric modulators, towards developing drugs with potential to treat CB2-associated maladies.

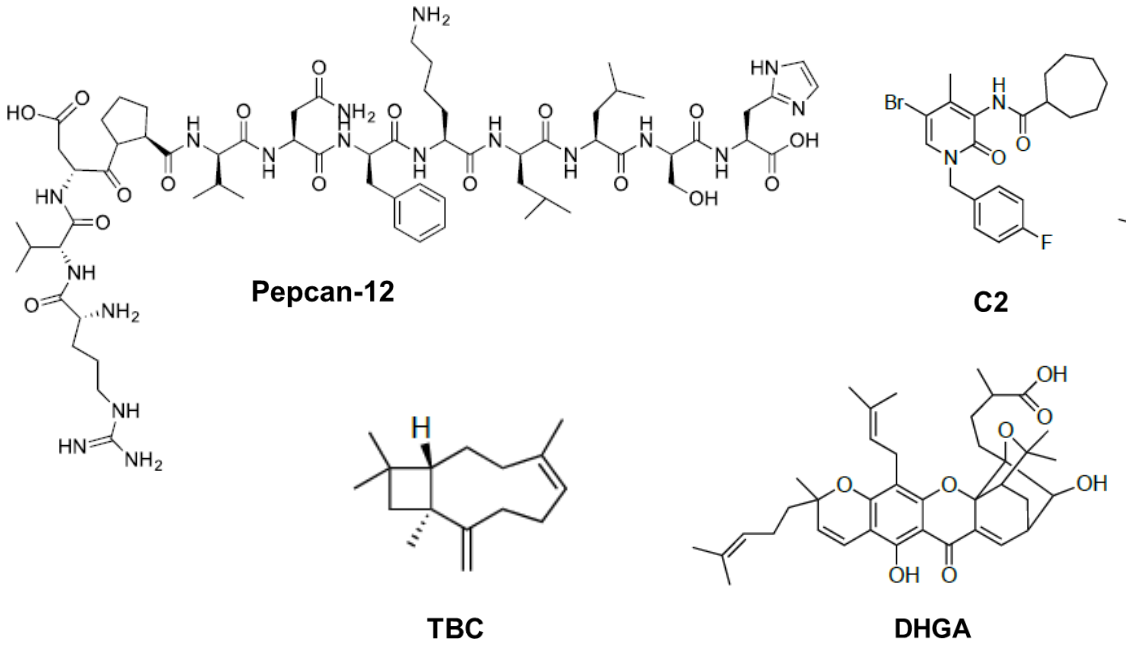

Figure 16. Known CB2 allosteric modulators

Four known CB2 allosteric modulators Pepcan-12 (RVD-hemopressin), C2 (N-[5-Bromo-1,2-dihydro-1-(4′-fluorobenzyl)-4-methyl-2-oxopyridin-3yl]cycloheptanecarboxamide), TBC (trans-β-caryophyllene) and DHGA (dihydro-gambogic acid). Pepcan-12 and C2 are CB2 PAM where TBC and DHGA are CB2 NAM.

4.2 Experimental Procedures

Co-crystallizations of CB2 with NAMs and WIN 55,212-2

We will first optimize the crystals of CB2 with WIN 55,212-2 (we already obtained) by testing various crystallization conditions and LCP lipid additives until we obtain crystals with high quality to allow structural determination. Then, we will use the same experimental conditions and further optimize them to crystallize CB2 with WIN 55,212-2 and two NAMs. Based on our previous successful experience in the LCP crystallization of other GPCRs [81, 84, 89, 93], the

major experimental parameters to optimize are host lipids and temperatures for LCP crystallization. We will test a number of lipids for LCP crystallization including monopalmitolein, MAG7.7, MAG7.8, MAG7.9, and MAG8.7, and will test three different temperatures, 10^{o}C, 16^{o}C, and 20^{o}C [94]. The primary criterion for screening these conditions is to obtain large (over 10μm diameter) and monomorphous crystals.

We will also test CB2 mutations in our crystallization trials. Recently, a crystal structure of CB2 bound to an antagonist was reported [95]. The authors used a similar construct of CB2 with a T4L insertion in ICL3 in their studies. To facilitate the crystallization of antagonist-bound CB2, five mutations were used to increase the thermostability of CB2. These mutations did not affect the binding of antagonists to CB2 [95]. We reason that these mutations may help to crystallize CB2 with agonists and NAMs. We will first test these five mutations individually in radioactive ligand-binding assays and GTPγS binding assays to see if they affect the allosteric action of CB2 PAMs. We will then choose the ones that do not affect NAM action in our crystallization trials.

After we obtain crystals of CB2 with WIN 55,212-2 and NAMs, we will test X-ray diffraction and obtain diffraction data in the Advanced Photon Source (APS) at Argonne National Laboratory using a micro-focused X-ray beam. We will then use the molecular replacement method [96] to determine crystal structures of CB2 with WIN 55,212-2 and NAMs. The final structures will be evaluated and assessed by commonly used methods to ensure high quality.

CB2 compound synthesis and characterization

The peptide ligand pepcan-12 with the sequence RVDPVNFKLLSH will be synthesized through commercial services. For compound C2, we will synthesize it according to the published methods [74]. Starting from the 2-hydroxy-4- methyl-3-nitropyridine, catalytic hydrogenation will

be used to obtain derivative 3-Amino-2-hydroxy-4-methylpyridine. This derivative will react with cycloheptanecarbonyl chloride in toluene, DMF, and triethylamine, carried out initially at 0 °C and then at 30 °C for 48 h, afforded the N-(1,2-Dihydro-4-methyl-2-oxopyridin-3-yl)cycloheptanecarboxamide. C2 was synthesized starting from this amide which was treated with a solution of bromine in $CHCl_3$, affording the corresponding 5- bromo derivative N-(5-Bromo-1,2-dihydro-4-methyl-2-oxopyridin-3-yl)- cycloheptanecarboxamide. The treatment of this derivative with p-fluorobenzyl chloride afforded the desired N-alkylated compound C2. Synthesized compounds will be characterized in 3H-radioactive ligand-binding assays and ^{35}S-GTPγS binding assays as used previously to confirm their allosteric action.

Sample preparation and optimization and cryo-EM structure determination

We will perform experiments to prepare the samples of CB2-Gi with WIN 55,212-2 and two PAMs for cryo-EM data collection and structure determination. We will initially use the same experimental conditions that we used to obtain the structure of CB2-Gi complex with WIN 55,212-2 alone but will continually optimize our experimental conditions in parallel to facilitate high-resolution cryo-EM structure determination with PAMs as follows. i) We will test other orthosteric agonists. It has been shown that both pepcan-12 and compound C2 could enhance the binding and the agonistic action of CP-55,940 and the endocannabinoid 2-Arachidonoylglycerol (2-AG) [24-26, 44, 52]. CP-55,940 and 2-AG are chemically distinct from WIN 55,212-2, which may have different effects on the stability of the CB2-Gi complex. ii) We will test other Gi-stabilizing antibodies. G proteins exhibit certain flexibility and instability [97]. We used scFv16 to stabilize the Gi protein in the structural studies of CB2-Gi with WIN 55,212-2. However, one subdomain of Gαi could not be modeled due to a lack of a recognizable density map, indicating the high flexibility of this domain. To reduce such flexibility, we will test another antibody, Fab50. We

suggest that Fab50 can reduce the flexibility of Gi more than scFv16 does. As an additional refinement, we will also test the more rigid scFv fragment of Fab50 in our structural studies if necessary. To screen protein samples prepared with different experimental conditions and ligands, we will examine the particles of CB2-Gi complex with orthosteric agonists and two PAMs under cryo-EM until we find the optimal conditions for each PAM. We will collect high-resolution data of the signaling complex bound to each PAM and solve the cryo-EM structures.

Structure-guided functional studies

The structural insights into the allosteric action of CB2 PAMs will be further tested in mutagenesis studies. Specifically, CB2 residues that are involved in the recognition of PAMs based on the structures will be mutated. These CB2 mutants will be tested in radioactive ligand-binding assays and GTPγS binding assays. Mutations in CB2 that affect the effects of pepcan-12 and compound C2 in enhancing agonist-binding and receptor activation will illuminate the mechanism of allosteric modulation of CB2.

Development of CB2 allosteric modulators

We calculate the known CB2 modulator, compound **C2** and design the virtual compound collections from various chemical databases, including our CBID database [194] (https://www.cbligand.org/cbid/), and AlloSteric Database [195] (ASD, http://mdl.shsmu.edu.cn/ASD/), etc. Then, we will apply the molecular fingerprint search (implemented in our CBID) for molecular similarity search (Tc value>0.75). Sequentially, based on the *in silico* ADME/Tox prediction, we will select promising candidates for further studies.

CB2-fusion complex in lipidic mesophases

Proteoliposomes containing CB2 (bound to inverse agonist ligands) will be prepared at high density (> 50mg CB2 protein complex/ml) and reconstituted in the lipid phase. The final

mixture composition will be using monoolein as the host lipid with 60% lipids/40 % protein solution (w/w %). This composition will be mixed completely using a joint Luer mixing syringe (Hamilton), however, the exact composition of the LCP will be subject to optimization. The mixing process will be carried out until satisfactory mixing is obtained. The protein-lipid mixture will be transferred to the repeat dispenser. Meanwhile, glass sandwich plates will be prepared, although premade plates for LCP crystallization are now available and may be implemented during crystallization trials (LCP plates Hamilton, NeXtal-Qiagen). The mixed protein-lipid mass will be loaded to a repeat dispenser and a bolus of ~20 nl will be loaded to the individual wells.

Synthesis of CB2 negative allosteric modulators (NAM).

Comparing with CB1 NAM, NAMs of the CB2 receptor has been less recognized, and due to their unacceptable activity, it is demanded to search the next generation of NAM actively. For example, *trans*-β-caryophyllene (TBC) and dihydro-gambogic acid (DHGA) is the reported NAM of the CB2 receptor [196].

Radioligand Binding Assays

Radioligand binding assays using ^{3}H-CP55,940 and ^{3}H-WIN55,212-2 will be performed with CB2 receptor membrane preparations, as reported previously [85, 145, 197-199]. Briefly, 20 μg of membranes of CHO-K1-*h*CB2 cells are incubated in 500 μL of binding buffer (50 mM Tris-HCl, 2.5 mM EDTA, 5 mM MgCl2,0.5 mg/mL fatty acid-free BSA, pH 7.4) in silanized glass tubes in presence of different concentrations of pepcans and 0.5 nM ^{3}H-CP55,940 (168 Ci/mmol) or 2.5 nM ^{3}H-WIN55,212-2 (40 Ci/mmol) for 60 min at 30 °C. Nonspecific binding of the radioligand will be determined in the presence of 10 μM WIN55,512-2 or CP55,940, respectively. After the incubation time, membrane suspensions are rapidly filtered through a 0.1% polyethyleneimine presoaked 96-well microplate bonded with GF/B glass fiber filters (UniFilter-

96 GF/B, PerkinElmer Life Sciences) under vacuum and washed 12 times with 150 μL of ice-cold binding buffer Filters are added with 40 μL of MicroScint20 scintillation liquid, and radioactivity is measured with the Trilux top counter (PerkinElmer Life Sciences). Data will be collected from 3–10 independent experiments, each performed in triplicate, and the nonspecific binding will be subtracted. The results are expressed as a percentage of vehicle-treated samples. The detailed protocols have been reported by us [193, 198-201].

Dissociation Kinetic Studies Using Isotopic Dilution.

Dissociation kinetics experiments are performed as described before [197]. Briefly, 20 μg of membranes of CHO-K1-*h*CB2 cells were incubated in 500 μL of binding buffer in silanized glass tubes and incubated with 0.5 nM ^{3}H-CP55,940 for 60 min at 30 °C. Radioligand dissociation will be initiated by the addition of 1 μM WIN 55,212-2 in the presence of 300 nM pepcan-12 or solvent (DMSO) and incubated for 1–120 min, at 30 °C. Nonspecific binding of the radioligand will be determined in the presence of 10 μM CP-55,940. After the incubation time, membrane suspensions will be rapidly filtered through a 0.1% polyethyleneimine presoaked 96-well microplate bonded with GF/B glass fiber filters and washed as described above.

^{35}S-GTPγS assay

Assays will be performed as previously described [202]. Clean membranes expressing *h*CB2 were diluted in silanized plastic tubes with GTPγS binding buffer (50 mM Tris-HCl, 3 mM MgCl2, 0.2 mM EGTA, and 100 mM NaCl at pH 7.4 supplemented with 0.5% fatty acid-free BSA) in the presence of 10 μM of GDP and0.1 nM of ^{35}S-GTPγS. The mixture is kept on ice until the binding reaction was started by adding the vehicle or compounds. Non-specific binding is measured in the presence of 10 μM GTPγS. The tubes are incubated at 30 °C for 90 min under shaking and then put on ice to stop the reaction. An aliquot (185 μL) of the reaction mixture will

be rapidly filtered through a 96-well microplate bonded with GF/B glass fiber filters previously pre-soaked with ice-cold washing buffer (50 mM of Tris-HCl pH 7.4 plus 0.1% fatty acid-free BSA). The filters are washed six times with 180 μL of washing buffer under vacuum. The radioactivity is measured after the addition of 45 μL of MicroScint20 scintillation cocktail. Specific binding is calculated by subtracting the residual radioactivity signal obtained in the presence of an excess of GTPγS and the results will be expressed as % of vehicle control.

cAMP assay

Described in Chapter III.

β-*arrestin* assay

The PathHunter® β-arrestin cell line (CHO-K1-HOMSA-CNR2) is maintained in culture in F-12 medium supplemented with 10% FBS, 200 μg/mL hygromycin, and 800 μg mL−1 Geneticin (G418). For the experiments, 100 μL well−1 of cell suspension (2 × 105 cell/mL) is plated in 96-well plate and left overnight in the incubator. The day after, tested compounds or vehicle are diluted in 40 μL of CO2-independent medium plus 10% FBS, added to the cells and incubated for 90 min at 37 °C. Following stimulation, the signal is detected using the PathHunter® Detection Kit according to the instruction protocol and the chemiluminescence is measured. Background levels are subtracted, and results expressed as % of vehicle control. The data analysis and detailed protocols are reported [203].

4.3 Experimental Results

4.3.1 Identification and binding features of CB2-G protein biased ligands

To study the binding features of CB2 biased ligand, we first extract the WIN 55,212-2 from our cryo-EM structure and obtain the energy minimized CB2 model. Then, we dock the WIN 55,212-2 back to validate our working model. The docking score of WIN 55,212-2 is 10.31 with binding poses similar to our structure, which prove the feasibility of our computational methods. Then, we use two known CB2 biased ligands JWH-133 and LY2828360 as well as an unbiased ligand CP-55,940 for the docking studies. **Figure 17** shows the binding poses of JWH-133 and LY2828360, compared with WIN 55,212-2. The unbiased ligand WIN 55,212-2 has a morpholine moiety extend to the hydrophobic pocket (as shown in yellow), where it has interactions with $I110^{3.29}$, $G111^{3.30}$, $L191^{5.40,}$ and $W194^{5.43}$. In contrast, although most of the JWH-133 and LY2828360 align pretty well with WIN 55,212-2, both of them do not extend deep enough to this pocket to form strong hydrophobic interactions. To further validate our findings, we dock another unbiased ligand CP-55,940 into our cryo-EM structure and compared it with WIN 55,212-2 (**Figure 17**). The overall poses in the binding pocket are very similar between two ligands and expectedly, both ligands possess a hydrophobic functional group that forms interactions within the highlighted region. These results together with our structural findings, provide strategies to screen or design novel CB2 biased ligand with CB2/CB1 selectivity and desired efficacy.

Based on the criteria and hypothesis above, an in-house library of more than two hundred CB2 compounds was used in the initial docking studies to identify potential CB2 biased ligand. **Figure 17** shows one of the best-scored ligand XIE95OYQ103 with the most similar binding features with JWH-133 and LY2828360. It does not extend to the previously defined hydrophobic pocket (as shown in yellow), and at the same time, it has two hydrophobic rings pointing upward

that align very well with LY2828360 (as shown in gray). Thus, this compound appears to have the potential to become a CB2 biased ligand. To validate our predictions from computational modeling, we will use cAMP functional assay and BRET assay to explore the functional selectivity of certain CB2 ligand. A known unbiased ligand CP-55,940 will be used as the control. The functional selectivity of CB2 ligand is characterized using algorithms from published papers [204]. Besides the current series of ligand, more CB2 ligands will be screened by docking, MD simulation, similarity search, and characterized using these functional assays.

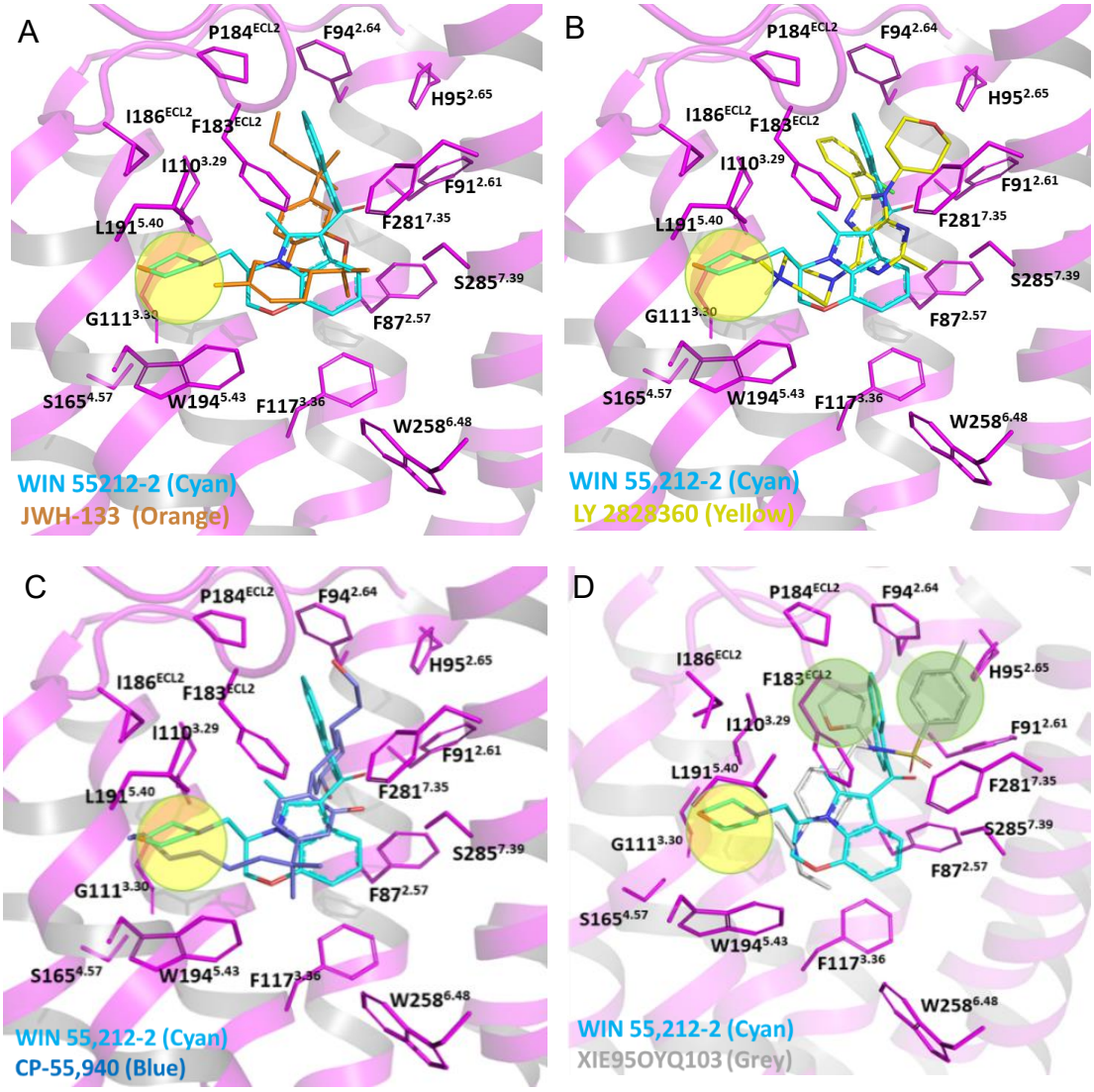

Figure 17. Docking Studies and Binding Features of CB2 Biased Ligand.

(A) Docking pose of CB2 unbiased ligand WIN 55,212-2 and CB2 G protein biased ligand JWH-133 to CB2 cryo-EM structure (PDB:6PT0). Yellow highlighted hydrophobic area is formed by L191$^{5.40}$, G111$^{3.30}$, S165$^{4.57,}$ and W194$^{5.43}$. (B) Docking pose of CB2 unbiased ligand WIN 55,212-2 and CB2 G protein biased ligand LY 2828360 to CB2 cryo-EM structure (PDB:6PT0). Yellow highlighted hydrophobic area is formed by L191$^{5.40}$, G111$^{3.30}$, S165$^{4.57,}$ and W194$^{5.43}$. (C) Docking pose of CB2 unbiased ligand WIN 55,212-2 and CB2 unbiased ligand CP-55,940 to CB2 cryo-EM structure (PDB:6PT0). Yellow highlighted hydrophobic area is formed by L191$^{5.40}$, G111$^{3.30}$, S165$^{4.57,}$ and W194$^{5.43}$. (D) Docking poses of CB2 unbiased ligand WIN 55,212-2 and in-house CB2 ligand XIE95OYQ103 to CB2

cryo-EM structure (PDB:6PT0). Yellow highlighted hydrophobic area is formed by L191$^{5.40}$, G111$^{3.30}$, S165$^{4.57,}$ and W194$^{5.43}$.

4.3.2 Expression and purification of CB2-Gi complex with CB2 G-protein biased ligand

JWH-133 is reported to be a G-protein biased CB2 ligand with Ki=3.4nM and about 200 folds selectivity for CB2 over the CB1 receptor. With the CB2/Gi constructs, nanobody, and purification conditions developed in Chapter III, we first changed the WIN 55,212-2 to JWH-133 to test whether it can stabilize the CB2/Gi/scFv complex as good as WIN 55,212-2. As shown in **Figure 18**, a very sharp monomer peak was obtained and validated from the size-exclusion column and coomassie blue gel, respectively. Further investigation including negative staining and initial cryo-EM screening will be done using this sample.

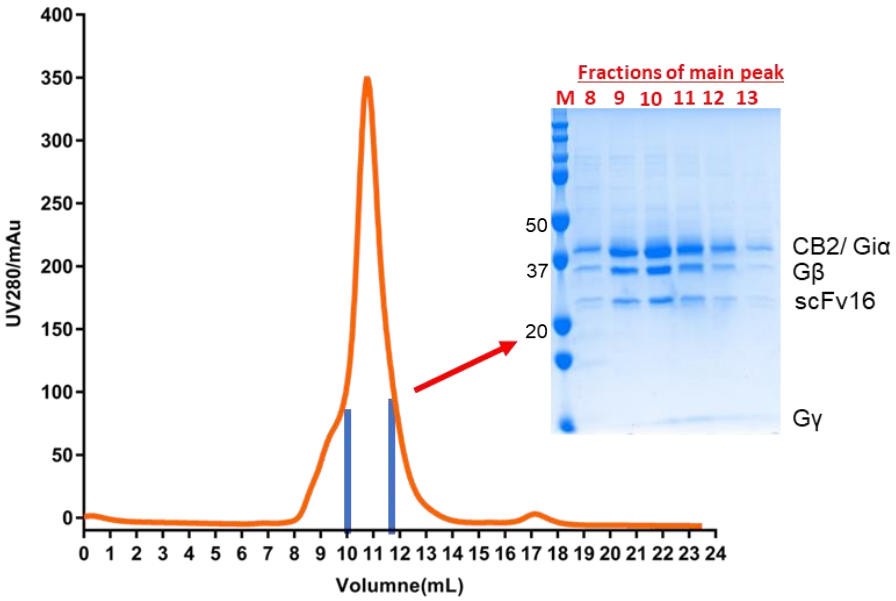

Figure 18. Purification of CB2-Gi Complex with CB2 Biased Ligand JWH-133.

Size-exclusion column purification of CB2/Gi/scFv16 complex with CB2 biased ligand JWH-133. The main peak was collected and characterized by coomassie blue gel. CB2, Giα, Gβ, Gγ and scFv16 bands are shown at their molecular weight compared to the marker.

4.3.3 Identification of CB2 allosteric modulators

Recently, the reported crystal structure of CB1 with the CB1 NAM ORG27569 and the agonist CP-55,940 showed that the Site II [113] is the allosteric binding pocket in CB1 (**Figure 19**). Since CB2 and CB1 share similarity of both sequence and structure, as well as a lot of literature, supported their similar allosteric regulation mode, we supposed that CB2 may possess a similar allosteric binding region with CB1-Site II. We first docked the only known synthetic CB2 PAM C2 to our active CB2 cryo-EM structure, as shown in **Figure 20**. We found that Trp158$^{4.50}$ and Ser75$^{2.45}$ formed hydrogen bonds with C2 at the distance of 4.2 Å and 3.0 Å respectively while Leu154$^{4.46}$, Gly78$^{2.48}$, Leu71$^{2.41}$, and Val159$^{4.51}$ interacted with C2 via hydrophobic interactions. Then, we calculated the recognition pattern between CB2 and its modulator-C2 as a reference (**Figure 20 right**). Sequentially, a virtual screening will be conduct against the virtual modulator library**.** Finally, we will select the virtual hits by comparing their recognition pattern with that of C2. In addition, the different recognition parents of allosteric modulators between CB2 and CB1 will aid the future development of novel allosteric modulators with high CB1/CB2 selectivity to achieve a specific therapeutic effect and with less side effect.

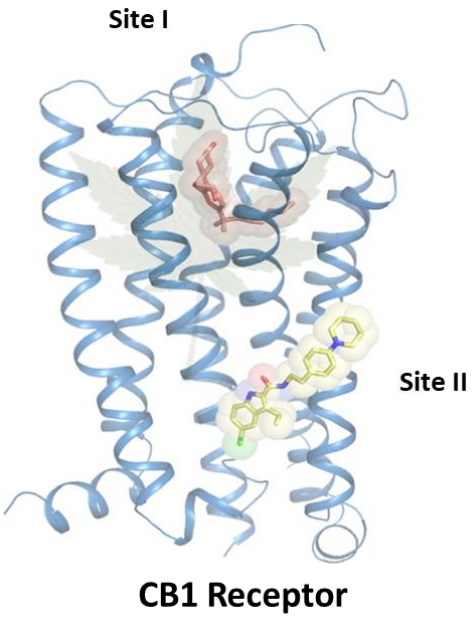

Figure 19. The allosteric binding pocket of CB1.

Two potential allosteric binding pocket of CB1 are highlighted as Site I and Site II. Site II has been proved to be the binding pocket of ORG27569 in the CB1 crystal structure with CP55940 and ORG27569

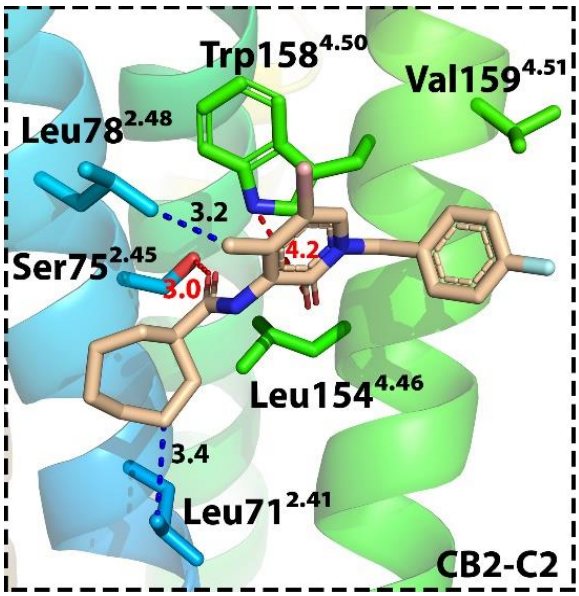

Figure 20. Detailed interaction of C2 in allosteric binding pocket (predicted Site II) of CB2.

Docking pose and interactions are shown on the left panel. Four interactions between C2 and CB2 was described including the hydrogen bond to Ser75 and Trp158.

4.4 Discussion and Conclusion

Although we have solved the first cryo-EM structure of CB2-Gi complex recently that described in Chapter III, there is still a long way to go in terms of uncovering the structural information of CB2 in different conformations and with different kinds of small molecules. Thus, we continued the research toward elucidating novel CB2 structures with CB2 biased ligand and CB2 allosteric modulators. In this study, we have obtained a series of promising preliminary results for further investigations using both X-ray crystallography and cryo-EM.

First of all, we identified the binding features of CB2 G-protein biased ligands by docking studies. These results suggest that the hydrophobic cavity formed by G111, S165, L191, and W194 might be important to distinguish the CB2 biased ligands from unbiased ligands, which will guide the further design of more CB2 G-protein or β-arrestin biased ligands. Then, we use commercially available CB2 G-protein biased ligands JWH-133 to purify the CB2-Gi complex for cryo-EM trials. The preliminary results show a stable complex obtained from the SEC. These can be very useful for further optimization and final data collections in the cryo-EM studies. We also developed a series of functional assays such us β-arrestin BRET assay and cAMP assays to validate the novel CB2 biased ligands we identified through computational predictions.

Additionally, we are interested in how CB2 allosteric modulators bind to the receptor and the design of novel modulators. So first we use both WIN 55,212-2 and one of the published CB2 positive allosteric modulators for cryo-EM studies. Although more screening and optimization are needed, we have successfully obtained stable complex bound to both small molecules by applying previous experimental conditions in Chapter III. We have also conducted a series of X-ray crystallography trials with WIN 55,212-2 and CB2 negative allosteric modulators. There are several initial crystals observed in multiple conditions in LCP, which is encouraging for further

screening. Meanwhile, we employed the machine learning methods and fragment-based design approach to design and synthesize in-house CB2 PAM and NAM, which will also be tested first in functional assays and then in the cryo-EM or X-ray crystallography studies.

In summary of this Chapter, we have built a series of CB2 constructs for the X-ray crystallization, cryo-EM, and functional studies. Consequently, we successfully expressed and purified the CB2 protein with CB2 biased ligand and CB2 modulators. Computational docking is also applied to facilitate the identification of novel CB2 ligands. All these results prove strong feasibility to obtain novel CB2 structure with different ligands and in different conformations.

5.0 Summary and Perspectives

Over the past decades, significant advancement has been accomplished in the cryo-EM field to elucidate the structural information of GPCRs. Among them, cannabinoid receptors especially CB2 has attracted much attention due to their important roles in many physiological and pathological processes. Although the crystal structure of inactive CB2 is available, however, the mechanisms underlying CB2 activation and signaling are poorly understood but critical for drug design. The results in this dissertation including structural information of CB2 active structure, the computational algorithm, and bio-assay validations provide insights into the design of CB2 selective agonist, CB2 allosteric modulators as well as the CB2 functional selective ligands. It also paved the way for further studies relating to CB2 pharmacology and systematic drug design.

The first part of the research was focused on the cryo-EM structure of an agonist-bound CB2-G_i signaling complex. By delineating the CB2 structural basis for ligand recognition and G protein recruitment, this study facilitates the rational design and development of CB2 agonists with high affinity and selectivity, as well as optimal therapeutic effects. Besides the novel CB2 cryo-EM structure, we also investigated the detailed interactions between the potent agonist WIN 55,212-2 and the receptor, the key residues determining ligand selectivity and efficacy, the differences of activation mechanisms between CB2 and CB1, and the unique molecular features of the CB2-G_i protein interaction.

Our 3-D cryo-EM structure of CB2 reveals that WIN 55,212-2 occupies the same orthosteric binding pocket as antagonist AM10257 in CB2 and stabilizes the CB2-G_i complex in its active conformation through interference with the “toggle switch” residue $W258^{6.48}$, which is critical for distinguishing agonists from antagonists. ECL2 and residues from TM2, TM3, and

TM6 play important roles in CB2 ligand recognition and ligand selectivity. This provides an advanced strategy for the rational design of CB2 selective agonists. The divergent conformation of $W^{6.48}$ in CB1 versus CB2 is associated with a series of distinct residue rearrangements in the intracellular side of TM5, TM6, and TM7 of CB2, as addressed above, which distinguish the activation/ G_i signaling mechanism of CB2 from that of CB1. While several novel synthetic CB2-selective agonists, including thiophene-containing compounds, have recently been reported [174-178], few have entered clinical trials and none have yet been approved by the FDA. The results presented herein are likely to aid in the development of potent and selective CB2 ligands with clinical therapeutic potential.

Comparison of the CB2-G_i complex with CB1-G_i, Rhodopsin-G_i, μOR-G_i, and β_2AR-G_s complexes reveals certain similar overall interaction profiles for receptor-G protein binding. Although CB2 and CB1 share a great structural similarity, their interactions with the α5 helix of the G protein remain distinct, reflecting the versatility of G_i coupling. $P139^{ICL2}$ in CB2 and the homologous residue in other GPCRs are critical for G protein coupling, and the unique motif of "$P138^{ICL2}P139^{ICL2}$" in ICL2 of CB2 contributes to its G_i coupling specificity. The well-resolved ICL3 structure provides detailed information relating to CB2 interaction with the G protein. Our findings, along with the published CB1 structures and CB2 inactive structures should aid in the rational design of drugs targeting CB2.

The second part of this research was focused on the elucidation of novel CB2 structures bound with CB2 biased ligand or CB2 allosteric modulator. We have already purified the CB2 complex with CB2 G-protein biased ligand JWH-133, which will be used for the preliminary data collection using cryo-EM. Previous experimental conditions in the first part of this dissertation were applied and optimized. By using the published CB2 G-protein biased ligands, we have also

conducted the docking studies and similarity search to identify in-house CB2 and their binding features. These preliminary hypotheses and computational predictions will be validated using a series of bio-assays and will be used to guide the design of novel CB2 G-protein biased ligands.

Additionally, we have obtained all the known CB2 allosteric modulators for our preliminary screening in both X-ray crystallography studies and cryo-EM studies. Meanwhile, we are also designing and synthesizing novel CB2 allosteric modulators based on the CBID database and molecular fingerprint-based similarity search. Currently, we have obtained initial CB2 crystals with WIN 55,212-2 and CB2 NAM using X-ray crystallography although further optimizations and crystallization trials are needed to improve the crystal quality. We have also co-expressed the CB2 with G protein using both WIN 55,212-2 and CB2 PAM, which give promising results during the purification process.

Overall, in this study, a novel cryo-EM structure of human cannabinoid receptor CB2-G_i signaling complex was obtained, which reveals the binding mode of WIN 55,212-2 and structural determinants for distinguishing CB2 agonists from antagonists. Further structural analysis with computational docking results uncovers the differences between CB2 and CB1 in receptor activation, ligand recognition, and G_i-coupling. CB2 allosteric modulators and CB2 biased ligand were also designed, synthesized, and utilized in the further research of novel CB2 structures in different conformations and novel CB2 signaling mechanisms. Nonetheless, more screenings as well as the advancements in multiple approaches and technologies can be done to increase the overall resolution of current structures, which enable us to dig deeper into the CB2 structure and its molecular mechanisms. Currently, we are designing a series of new thermostable mutations of CB2 to further stabilize the receptor. We are also building an exciting collaboration with NASA

to grow crystals in the space shuttle, where the microgravity environment will benefit the crystal packing of CB2 and enable us to obtain larger and better quality crystals for X-ray diffraction.

In conclusion, our findings along with the published CB1 and CB2 structures will fulfill the complete profile of cannabinoid system receptors and should aid in the rational design of drugs targeting CB2 receptors.

Appendix A

Table 1. Reagent or Resources

REAGENT or RESOURCE	SOURCE	IDENTIFIER
Chemicals, Peptides, and Recombinant Proteins		
WIN 55,212-2 Mesylate	MedChemExpress	Cat# HY-13291
(−)-CP 55,940	Cayman Chemical	Cat# 90084
Lauryl maltose neopentyl glycol	Anatrace	Cat# NG310
n-dodecyl-β-D-maltoside (DDM)	Anatrace	Cat# D310S
Cholesteryl Hemisuccinate	Anatrace	Cat# CH210
CHAPS	Fisher Bioreagents	Cat# BP5715
Digitonin	Millipore Sigma	Cat# 30-041-01GM
Leupeptin	Sigma-Aldrich	Cat# L2884
Benzamidine	Sigma-Aldrich	Cat# 12072
FLAG peptide	GL Biochem	Custom Synthesis
GDP	Sigma Aldrich	Cat# G7127
ESF921 culture medium	Expression System	Cat# NC9541308
2-Mercaptoethanol	Sigma-Aldrich	Cat# M6250
Apyrase	New England Biolabs	Cat# M0398L
PNGase F	New England Biolabs	Cat# P0704S
TEV protease	Prepared In-House	N/A
Anti-Flag M1 resin	Sigma Aldrich	Cat# A4596
N-[4-(7-diethylamino-4-methyl-3-coumarinyl)phenyl]maleimide (CPM)	Sigma	Cat#C1484
FuGENE Transfection Reagent	Promega	Cat#E2311
DyLight 488	Thermo Fisher	Cat#46402
Critical Commercial Assays		
LANCE cAMP Detection Kit	PerkinElmer	Cat# AD0262
Deposited Data		
CB2-Gi coordinates	This paper	PDB: 6PT0
CB2-Gi EM map	This paper	EMDB: EMD-20470

Experimental Models: Cell Lines		
Spodoptera frugiperda Sf9 cells	Novagen	Cat# 71104-3
CHO-K1	PerkinElmer	Cat# ES-111-C
Oligonucleotides		
CB2 forward primer	IDT	N/A
CB2 reverse primer	IDT	N/A
Recombinant DNA		
pFastbac-prolactin-Flag-BN-CB2-H8	This paper	N/A
pFastbac-Gαi1_4M	This paper	N/A
pFastbac-H8-Gβ1	This paper	N/A
pFastbac-Gγ2	This paper	N/A
pFastbac-GP67-scFv16-H8	This paper	N/A
Software and Algorithms		
Clonemanager	Sci-Ed Software	http://www.scied.com/pr_cmpro.htm
Prism7	GraphPad	https://www.graphpad.com/scientific-software/prism/
SerialEM	Mastronarde, 2005	http://bio3d.colorado.edu/SerialEM/
MotionCor2	Zhen, *et al*., 2017	http://msg.ucsf.edu/em/software/motioncor2.html
Relion 3.0	Zivanov, J. *et al.*, 2018	https://www3.mrc-lmb.cam.ac.uk/relion/index.php/Download_%26_install
UCSF Chimera	Pettersen *et al.*, 2004	https://www.cgl.ucsf.edu/chimera/
Phenix	Adams *et al.*, 2011	https://www.phenix-online.org/
Coot	Emsley and Cowtan, 2004	https://www2.mrc-lmb.cam.ac.uk/personal/pemsley/coot/
PyMol 2.3	Schrödinger	https://pymol.org/2/
MolProbity	Williams *et al.*, 2018	http://molprobity.biochem.duke.edu/
Other		

Quantifoil R1.2/1.3 300-mesh holey carbon-coated grids	Quantifoil	https://www.emsdiasum.com/microscopy/products/grids/quantifoil.aspx
Nickel Sepharose resin	GE healthcare	Cat#17526801
Superdex 200 Increase column	GE healthcare	Cat#28990944

Table 2. Cryo-EM Data Collection

Data collection and processing	
Magnification	130,000
Voltage (kV)	300
Electron exposure (e–/Å2)	~83
Defocus range (μm)	-1.0~-2.5
Pixel size (Å)	1.029
Symmetry imposed	C1
11Initial particle images (no.)	1,590,810
Final particle images (no.)	721,844
Map resolution (Å)	3.20
FSC threshold	0.143
Refinement	
Initial model used (code)	6DDE
Model resolution (Å)	3.20
FSC threshold	0.143
Model resolution range (Å)	40-3.2
Map sharpening *B* factor (Å2)	-180
Model composition	10235
non-hydrogen atoms	1284
Protein residues	9
Ligands	
B factors (Å2)	122.5
Protein	150.4
Ligand	
R.m.s. deviations	0.004
Bond lengths (Å)	0.882
Bond angles (°)	
Validation	1.41
MolProbity score	4.98
Clashscore	
Ramachandran plot	97.3
Favored (%)	2.7
Allowed (%)	0
Disallowed (%)	

Table 3. Comparison of NMR spectroscopy, X-ray crystallpgraphy and cryo-EM

	Advantages	Disadvantages
NMR Spectroscopy	1. Structure obtained in solution 2. High resolution 3. Suitable for dynamic study	1. Sample preparation is difficult 2. High sample purity required 3. Computational simulation is difficult
X-ray Crystallography	1. Broad molecular weight range 2. High resolution 3. Easy for model building	1. Difficult for crystallization 2. Usually not native state structure
Cryo-EM	1. Structure in native state 2. Easy sample preparation 3. Small sample size	1. Relatively low resolution 2. Relatively high cost

Table 4. CB2 related agents in clinical trialss

Drug Design	Target & Efficacy	Indication	Phase
GW842166	CB2 receptor agonist	Osteoarthritis	Phase II
S-777469	CB2 receptor agonist	Atopic Dermatitis	Phase II
LEI-101	CB2 receptor partial agonist	Inflammation and oxidative stress	Pre-clinical
SMM189	CB2 receptor inverse agonist	Neurodegenerative diseases and traumatic brain injury	Pre-clinical

Appendix B

Detailed protocols of CB2 recombinant protein purification

- **Material needed:**
  - DDM (n-Dodecyl-β-D-Maltopyranoside, ANTTRACE)
  - CHAPS (3-[(3-Cholamidopropyl) dimethylammonio]-1-propanesulfonate).
  - CHS (Cholesteryl hemisuccinate)
  - Protease inhibitor: Leupeptin (2 mg/ml, 5000X)
    Benzamidine (150 mg/ml, 1000X)
  - Alkylating agent: IA powder (2-Iodoacetamide)
  - Glycosidase: PNGase F (Peptide -*N*-Glycosidase F)
  - 2M Tris pH 7.5; 0.5M EDTA pH 8.5; 1M HEPES pH7.5; 4M Imidazole
  - Salt Active Nuclease (SAN)
  - Bio-Rad Protein dye
  - His60 Ni Superflow Resin (From Clontech Laboratories Inc.)
  - Glycerol
  - 5M NaCl; $MgCl_2$ (2mM); $CaCl_2$ (2mM)
  - Flag column and Flag peptide (20 mg/ml)
  - CB_2 Ligand: Xie 2-64
- **Procedures:**
  - Preparation of Lysis, Solubilization, Ni Column, and Flag Column buffer before the day of doing purification.

    - **Lysis Buffer 500 ml (store at 4°C)**:

Stock	Volume	Final concentration
2M Tris pH 7.5	*5ml*	*20mM*
0.5M EDTA pH 8.5	*200ul*	*1mM*
**IA powder*	*1g*	*2mg/ml*
**Leupeptin*	*100ul*	*1X*
**Benzamidine*	*500ul*	*1X*

** CB2 Ligand, 50mM*	*20ul*	*2uM*

Add ddH_2O to 500ml.
**Add freshly right before use*

- **Solubilization Buffer 500ml (store at 4°C)**:

Stock	Volume	Final concentration
DDM powder	*5g*	*1%*
CHS powder	*1.5g*	*0.3%*
CHAPS	*2.5g*	*0.5%*
1M HEPES pH7.5	*10ml*	*20mM*
5M NaCl	*75ml*	*750mM*
Glycerol	*100ml*	*20%*
**IA powder*	*1g*	*2mg/ml*
**Leupeptin*	*100ul*	*1X*
**Benzamidine*	*500ul*	*1X*
** CB2 Ligand, 50mM*	*20ul*	*2uM*

Add ddH_2O to 500ml, mix at R.T, or 4℃ overnight.
**Add freshly right before use*

- **Ni Column Buffer 500ml (store at 4°C after filtration):**

Stock	Volume	Final concentration
DDM powder	*0.5g*	*0.1%*
CHS powder	*0.5g*	*0.1%*
CHAPS	*2.5g*	*0.5%*
1M HEPES pH7.5	*10ml*	*20mM*
5M NaCl	*75ml*	*750mM*

Glycerol	*100ml*	*20%*
**Leupeptin*	*100ul*	*1X*
**Benzamidine*	*500ul*	*1X*
** CB2 Ligand, 50mM*	*20ul*	*2uM*

Add ddH_2O to 500ml, mix at R.T, or 4℃ overnight. Filter the buffer the next day.
**Add freshly right before use to the filtered buffer.*

- **Flag Buffer 200ml (store at 4°C after filtration)**:

Stock	Volume	Final concentration
DDM powder	*0.2g*	*0.1%*
CHS powder	*0.2g*	*0.1%*
CHAPS	*1g*	*0.5%*
1M HEPES pH7.5	*4ml*	*20mM*
5M NaCl	*4ml*	*100mM*
**Leupeptin*	*40ul*	*1X*
**Benzamidine*	*200ul*	*1X*
** CB2 Ligand, 50mM*	*8ul*	*2uM*

Add ddH_2O to 200ml, mix at R.T, or 4℃ overnight. Filter the buffer the next day.
**Add freshly right before use to the filtered buffer.*

- **Lysis:**
  - Thaw pellet from -80℃ in water.
  - Get Pre-made Lysis buffer from 4℃, pour 100 ml into the beaker.
  - Add IA powder, Leupeptin, Benzamidine (L&B), and Xie 2-64 to the lysis buffer.
  - Stir at 4°C for 25min after dissolving all pellets.
  - Transfer into 250 ml centrifuge tube, 15000 rpm, 25 min using <BECKMAN COULTER Avanti J-E, Rotor JLA-16.250>

- **Solubilization:**
    - Get pre-made Solubilization buffer from 4℃, pour 50 ml into the beaker.
    - Add L&B and Xie 2-64.
    - Pour 40ml into pellet and transfer into douncer, then add IA powder into douncer.
    - Dounce on ice for 30 times, wash with the remaining 10 ml buffer.
    - Collect using a beaker after dounce, add $MgCl_2$ (2mM) and Salt Active Nuclease (SAN) (0.5ul/100ml)
    - Stir at 4℃ for 2 h with foil cover the beaker.
- **Ni Column:**
    - Get Ni+ resin in 4℃, mix well and transfer into the column.
    - Wash by water to remove EtOH, then transfer into a 50 ml centrifuge tube. Centrifuge 3500 rpm for 5 min to remove the upper layer of water using <Thermo Sorvall LEGEND X1R, Rotor No. 75003181>
    - Get Solubilization mix and centrifuge 15000 rpm for 40 min using <BECKMAN COULTER Avanti J-E, Rotor JLA-16.250>
    - Pour supernatant into a 50 ml centrifuge tube with Ni+ resin.
    - Add imidazole (10 mM), stir at 4℃ overnight.
    - Centrifuge 3500 rpm for 15 min and discard the supernatant.
    - Get Ni+ column buffer 70 ml from 4℃ and then add L&B and Xie 2-64.
    - Add imidazole (40 mM) to 50 ml buffer in the last step as Ni+ washing buffer and imidazole (400 mM) 20 ml from Step 7 as Ni+ elute buffer.
    - Add Ni washing buffer 10 ml to the Ni resin, mix well and centrifuge 3500 rpm for 10 min, discard the supernatant.
    - Transfer Ni resin into the column using Ni washing buffer. Wash with remaining Ni washing buffer until other protein came out. (Detect using 2 ul from column added into Bio-Rad dye 20 ul)
    - Elute with Ni elute buffer until all CB_2 protein came out.
- **Flag Column:**
    - Add $CaCl_2$ (2mM) to Ni elution.
    - Get Flag buffer from 4℃, pour 40 ml into a 50 ml centrifuge tube.
    - Add L&B and Xie 2-64, add CaCl2 (2 mM) into 30 ml from the last step as Flag washing buffer; add 100 ul Flag, and 100ul EDTA to the remaining 10ml as Flag elute buffer.
    - Wash Flag column with Flag washing buffer (10 ml) and then load Ni elution, collect the sample as Flag flow through.
    - Wash with remaining 20 ml Flag washing buffer.

- Elute with Flag elute buffer, collected using a 1.7 ml EP tube (1ml/tube), detected by the protein-dye.
- Combine protein and centrifuge to 500 ul using protein centrifuge tube, then test concentration after transferring all protein into a 1.7 ml EP tube.
- Cut cleavage site overnight and run gel tomorrow, then run SEC.

  TEV cleavage:
  - ❖ Use 480 ul of 500 ul protein for the cleavage and 20 ul as a comparison.
  - ❖ Add 1 ul TCEP and 3 ul TEVase to 480 ul of protein.
  - ❖ Sit at R.T. for 1h
  - ❖ Put in 4℃ overnight.

  3C cleavage:
  - ❖ Use 4ul 3C enzyme
  - ❖ Sit at RT for 1h
  - ❖ Put in 4^{o}C overnight

  If the construct contains both TEV and 3C:
  - ❖ Use 480 ul of 500 ul protein for the cleavage and 20 ul as a comparison.
  - ❖ Add 1 ul TCEP and 3 ul TEVase to 480 ul of protein.
  - ❖ Take out another 20ul as comparison
  - ❖ Add 4ul 3C enzyme
  - ❖ Sit at RT for 1h
  - ❖ Put in 4^{o}C overnight

  If the construct needs de-glycosylation
  - ❖ Add 2ul PNGaseF simultaneously with 3C or TEV enzyme
  - ❖ RT 1h then 4^{o}C overnight

- **Size-Exclusive Column (SEC):**
  - Prepare wash buffer by adding HEPES (20 mM) +NaCl (100 mM) buffer and Xie 2-64 into the Flag buffer.
  - Wash column for 27 ml.
  - Inject sample and start a collection from 8 ml or when peaks came out.
  - Collect tubes that contain monomer peaks (usually around 11 ml)
  - Run coomassie blue gel to make sure you are collecting the right tubes.
  - Centrifuge protein to 500 ul and test concentration, store at 4℃. (Or grow crystal directly.)

Detailed protocols of CB2 recombinant protein crystallization

- **Material needed:**
  - MNG (maltose–neopentyl glycol)
  - CHS (Cholesteryl hydrogen succinate)
  - $CaCl_2$, NaCl
  - HEPES pH 7.5
  - Ligand
  - EDTA
  - Flag peptide
  - MNG stock buffer: 5% MNG, 0.5% CHS in 100mM HEPES pH 7.5
- **Procedures:**
  - **MNG exchange: (For crystallization, MNG exchange is normally done during Flag purification)**
    - MNG buffer: 0.1% MNG, 0.01% CHS, 2mM Ca^{2+},20mM HEPES pH 7.5, 100mM NaCl
    - Same procedure as Flag purification before eluting the protein
    - After loading Ni elution and wash with Flag buffer, continue wash to exchange DDM into MNG.
      - Wash with 30ml buffer: 15ml MNG buffer + 15ml Flag buffer + ligand
      - Wash with 20ml buffer: 15ml MNG buffer + 5ml Flag buffer + ligand
      - Wash with 15ml buffer: 13ml MNG buffer + 2ml Flag buffer + ligand
      - Wash with 10ml MNG buffer + ligand
    - Elute with LOW MNG buffer: 20mM HEPES pH 7.5, 100mM NaCl, 0.02% MNG, 0.002% CHS, EDTA, 200 µg/ml Flag peptide, 10 µM ligand
    - Same procedure after as Flag purification including PNGaseF + TEV or 3C as treatment.

  - **Size-Exclusive Column (SEC):**
    - Prepare wash buffer: 0.01% MNG, 20mM HEPES pH 7.5, 100mM NaCl, Ligand 1uM
    - Wash column for 27 ml.
    - Inject sample and start a collection from 8 ml or when peaks came out.
    - Collect tubes that contain monomer peaks (Run gel if necessary)
    - Run coomassie blue gel to see protein status.

- Concentrate protein to 10-20 ul (Add 100 uM Ligand before concentration and incubate on ice for 10min, 50kD cutoff)
- Pipette the protein into the EP tube.
- Get rid of the bottom part of the centrifuge tube and invert the centrifuge tube, centrifuge 1500rpm for one second to obtain the remaining protein in the tube.
- Combine the protein and test concentration.
- If the protein concentration is enough, stop concentrating.
- Use EP tube to centrifuge the protein in 4°C to get rid of the bubbles.

- Crystallization Setup:
  - Prepare glass plate sandwich
    - ❖ Glass plate soak in ddwater and take out
    - ❖ Spray the Glass water repellent and wipe use fine tissue to evenly distribute the water repellent.
    - ❖ Wait 20min and use a dry tissue to wipe the glass plate again
    - ❖ Stick the sticky plate to the glass plate firmly (one wide edge, one narrow edge). And stick the labels for condition screening on the wider edge.

  - Wash syringe apparatus with methanol and blow with air to dry.
  - Put one of the mixing tubes into 37°C to pre-warm.
  - At the same time, take out the condition buffer plate and shake in R.T for 10min, and then centrifuge at 600rpm for one second.
  - Meanwhile, take MOC out from -80°C and put it into 42°C to let it melt.
  - Weigh Protein in the syringe that stays in R.T and use 2:3 (w/w) ratio for Protein: Lipid.

    Push the protein to the other side of the syringe and seal with another part of the apparatus.
  - Weigh MOC (Monoolein 90% + cholesterol 10%) using syringe that in 37°C quickly in case the lipid becomes solid. And push the lipid to the other side too.
  - Mix at room temperature about 3-5 min or until the mixture turns clear.
  - Turn on the power of computer and robot and open software “Gryphon”, click connect.
  - After connection, click exchange solo syringe, and then put syringe on, adjust the location of the syringe until one drop comes out of the needle.
  - A window indicating the volume of protein-MOC mixture in the syringe is shown.

- Open protocol “LCP_SGP Glass” and set up a 20-40 nl mixture drop based on volume and how many plates to grow crystals.
- Setup a 700nl precipitant solution.
- Make sure the water in the bottle is enough and wash with ddwater in the bottle until the water fills up the white plate 3.
- Put precipitant solution on the left.
- Spray little EtOH on the right place and the put the plate sandwich on the right after get rid of dust.
- Wipe plate 6 areas with tissue.
- Run protocol and when done, if the precipitant solution is not dispensed well, use a pipette and do it by hand.
- Get rid of the dust of another piece of glass and put it on the plate sandwich.
- Roll it to firmly attach the glass to the sandwich.
- Put the glass plate into 20 °C for crystallization.
- Disengage syringe apparatus and wash with methanol:
    - Use a wash bottle to wash every place that might have contact with LCP.
    - Wash by pushing the methanol until the syringe is not blocked by the LCP.
    - Then disengage the needle and assemble the double syringe again to wash the middle part of the syringe with methanol by pushing.
    - Wash remaining part of the apparatus and dry by airflow.
    - Put back in the EtOH glass box.
- Wash the robot:
    - Turn the water pump switch that farther from us to the right.
    - Push the button to drain the water in the white plate 3 a little.
    - Take off plate 3 and drain the remaining water.
    - Put back in the plate 3 slot firmly.
- Disconnect and turn off the computer, then turn off the main power.

Transfection of Sf9 Cells

- **Material needed:**
    - CB_2 Bacmid
    - Sf9 cells grow to 1 M-1.3 M
    - FUGENE Transfection Reagent
    - Grace Medium
    - FBS (after filtration)

- ESF 921 Insect Cell Culture Medium (From Expression Systems, Catalog Number: NC1149297)
- Six-wells plate

➢ **Procedures:**

- Add Sf9 cells to the two wells of the six-wells plate (one for control and the other is to produce P0 virus), 1 ml per well.
- Allow the cells to attach at 27°C for at least 30 min.
- At the same time, prepare the transfection mix.
  - Mixture A: 10 ul FUGENE Transfection reagent
    100 ul Grace Medium
  - Mixture B: 5 ul of Bacmid
    100 ul of Grace Medium
    Gently mix A and B by fingers and sit at R.T. for 5 min respectively.
    Combine A and B and gently mix by finger, sit at R.T. for 30 min.
- Get the six-wells plate out, remain the control well unchanged and get rid of the cell medium in the P0 virus well, add 1ml Grace Medium, and then add transfection mix.
- Put the plate into a white box containing wetted paper tissues, at 27°C, 4 h.
- Remove Grace Medium and add 2 ml ESF 91 Cell Culture Medium into the well.
- Put the white box into 27°C and incubate for 5 days or until signs of viral infection are observed.
  - Control well: Cells are tight, grow faster, and cover more than 95% of wells.
  - P0 well: Cells become large, loose, grow slower, and cover only 50%-70% of wells.
- Collect the medium from P0 well into sterile 1.7 ml EP tube, centrifuge 12000 rpm, 5 min.
- Transfer the supernatant into another sterile 1.7 ml EP tube and add 2% FBS for storage at 4°C.
  - If it is used for P1 virus production directly, FBS is not needed.

Amplification of Baculovirual Stock from P0 to P1 virus

➢ **Material needed:**

- P0 virus from the last step
- Sf9 cells grow to 1 M-1.2 M

- ESF 921 Insect Cell Culture Medium (From Expression Systems; Catalog Number: NC1149297)

- **Procedures:**
  - Sf9 cells culture in suspension using ESF 921 Medium and grow to 1 M-1.2 M, 30 ml is needed for two ratio test (1:5000 and 1:10000).
  - Add P0 virus from last step 3 ul and 1.5 ul respectively to 15 ml of Sf9 cells.
  - Culture at 27°C for 4 days or until the cells stop to grow and 20%-70% of them become large or dead and the cell density becomes 3M-3.5M.
  - Use Flow Cytometry to test virus quality.
  - Collect P1 virus by centrifuging at 4 °C, 1000 rpm, 3 min.
  - Use 0.22um filter for the filtration of supernatant and add 2% FBS.
  - Pack separately by EP tube (1ml/tube), and store at -80°C for long term use. For the direct production of P2 virus or the short-term storage, put P1 virus into 4°C.

Amplification of Baculovirual Stock from P1 to P2 virus

- **Material needed:**
  - P1 virus from the last step
  - Sf9 cells grow to 1 M-1.2 M
  - ESF 921 Insect Cell Culture Medium (From Expression Systems, Catalog Number: NC1149297)

- **Procedures:**
  - Sf9 cells culture in suspension using ESF 921 Medium and grow to 1 M-1.2 M, 100 ml is needed for two ratio test (1:2500 and 1:5000). (If the P1 virus is thawed from -80°C, use 1:1000 ratio is better.)
  - Add P1 virus from last step 20 ul and 10 ul respectively to 50 ml of Sf9 cells.
  - Culture at 27°C for 3 days or until the cells stop to grow and 20%-70% of them become large or dead and the cell density becomes 3M-3.5M.
  - Use Flow Cytometry to test virus quality.
  - Collect P2 virus by centrifuging at 4°C, 1000 rpm, 3 min.
  - Use 0.22um filter for the filtration of supernatant and add 2% FBS.
  - Store at 4°C for the expression of the wanted protein.

Bibliography

1. Mechoulam, R., *Interview with Prof. Raphael Mechoulam, codiscoverer of THC.. Interview by Stanley Einstein.* Int J Addict, 1986. **21**(4-5): p. 579-87.
2. Kirkham, T.C., *Endocannabinoids in the regulation of appetite and body weight.* Behav Pharmacol, 2005. **16**(5-6): p. 297-313.
3. Seeley, R.J. and S.C. Woods, *Monitoring of stored and available fuel by the CNS: implications for obesity.* Nat Rev Neurosci, 2003. **4**(11): p. 901-9.
4. Calignano, A., et al., *Control of pain initiation by endogenous cannabinoids.* Nature, 1998. **394**(6690): p. 277-81.
5. Walter, L. and N. Stella, *Cannabinoids and neuroinflammation.* Br J Pharmacol, 2004. **141**(5): p. 775-85.
6. Fulmer, M.L. and D.P. Thewke, *The Endocannabinoid System and Heart Disease: The Role of Cannabinoid Receptor Type 2.* Cardiovasc Hematol Disord Drug Targets, 2018. **18**(1): p. 34-51.
7. Idris, A.I. and S.H. Ralston, *Role of cannabinoids in the regulation of bone remodeling.* Front Endocrinol (Lausanne), 2012. **3**: p. 136.
8. Sledzinski, P., et al., *The current state and future perspectives of cannabinoids in cancer biology.* Cancer Med, 2018. **7**(3): p. 765-775.
9. Lawrence, D.K. and E.W. Gill, *The effects of delta1-tetrahydrocannabinol and other cannabinoids on spin-labeled liposomes and their relationship to mechanisms of general anesthesia.* Mol Pharmacol, 1975. **11**(5): p. 595-602.

10. Y. Gaoni, R.M., *Isolation, Structure, and Partial Synthesis of an Active Constituent of Hashish.* J. Am. Chem. Soc, 1964. **86, 8, 1646-1647**.

11. Mechoulam, R. and L. Hanus, *A historical overview of chemical research on cannabinoids.* Chem Phys Lipids, 2000. **108**(1-2): p. 1-13.

12. Guindon, J., et al., *Synergistic antinociceptive effects of anandamide, an endocannabinoid, and nonsteroidal anti-inflammatory drugs in peripheral tissue: a role for endogenous fatty-acid ethanolamides?* Eur J Pharmacol, 2006. **550**(1-3): p. 68-77.

13. Ulugol, A., et al., *Antihyperalgesic, but not antiallodynic, effect of melatonin in nerve-injured neuropathic mice: Possible involvements of the L-arginine-NO pathway and opioid system.* Life Sci, 2006. **78**(14): p. 1592-7.

14. Guindon, J. and P. Beaulieu, *Antihyperalgesic effects of local injections of anandamide, ibuprofen, rofecoxib and their combinations in a model of neuropathic pain.* Neuropharmacology, 2006. **50**(7): p. 814-23.

15. Sofia, R.D., H.B. Vassar, and L.C. Knobloch, *Comparative analgesic activity of various naturally occurring cannabinoids in mice and rats.* Psychopharmacologia, 1975. **40**(4): p. 285-95.

16. Formukong, E.A., A.T. Evans, and F.J. Evans, *Analgesic and antiinflammatory activity of constituents of Cannabis sativa L.* Inflammation, 1988. **12**(4): p. 361-71.

17. Herzberg, U., et al., *The analgesic effects of R(+)-WIN 55,212-2 mesylate, a high affinity cannabinoid agonist, in a rat model of neuropathic pain.* Neurosci Lett, 1997. **221**(2-3): p. 157-60.

18. Bridges, D., et al., *Localisation of cannabinoid receptor 1 in rat dorsal root ganglion using in situ hybridisation and immunohistochemistry.* Neuroscience, 2003. **119**(3): p. 803-12.

19. Reche, I., J.A. Fuentes, and M. Ruiz-Gayo, *A role for central cannabinoid and opioid systems in peripheral delta 9-tetrahydrocannabinol-induced analgesia in mice.* Eur J Pharmacol, 1996. **301**(1-3): p. 75-81.

20. Tsou, K., et al., *Suppression of noxious stimulus-evoked expression of Fos protein-like immunoreactivity in rat spinal cord by a selective cannabinoid agonist.* Neuroscience, 1996. **70**(3): p. 791-8.

21. Richardson, J.D., S. Kilo, and K.M. Hargreaves, *Cannabinoids reduce hyperalgesia and inflammation via interaction with peripheral CB1 receptors.* Pain, 1998. **75**(1): p. 111-9.

22. Li, J., et al., *The cannabinoid receptor agonist WIN 55,212-2 mesylate blocks the development of hyperalgesia produced by capsaicin in rats.* Pain, 1999. **81**(1-2): p. 25-33.

23. Martin, W.J., C.M. Loo, and A.I. Basbaum, *Spinal cannabinoids are anti-allodynic in rats with persistent inflammation.* Pain, 1999. **82**(2): p. 199-205.

24. Guindon, J., et al., *Pre-emptive antinociceptive effects of a synthetic cannabinoid in a model of neuropathic pain.* Eur J Pharmacol, 2007. **568**(1-3): p. 173-6.

25. Guindon, J., A. De Lean, and P. Beaulieu, *Local interactions between anandamide, an endocannabinoid, and ibuprofen, a nonsteroidal anti-inflammatory drug, in acute and inflammatory pain.* Pain, 2006. **121**(1-2): p. 85-93.

26. Ottani, A., et al., *The analgesic activity of paracetamol is prevented by the blockade of cannabinoid CB1 receptors.* Eur J Pharmacol, 2006. **531**(1-3): p. 280-1.

27. Schelling, G., et al., *Effects of general anesthesia on anandamide blood levels in humans.* Anesthesiology, 2006. **104**(2): p. 273-7.

28. Klein, T.W., et al., *Cannabinoid receptors and T helper cells.* J Neuroimmunol, 2004. **147**(1-2): p. 91-4.

29. Killestein, J., et al., *Immunomodulatory effects of orally administered cannabinoids in multiple sclerosis.* J Neuroimmunol, 2003. **137**(1-2): p. 140-3.

30. Klein, T.W., *Cannabinoid-based drugs as anti-inflammatory therapeutics.* Nat Rev Immunol, 2005. **5**(5): p. 400-11.

31. Walsh, D., K.A. Nelson, and F.A. Mahmoud, *Established and potential therapeutic applications of cannabinoids in oncology.* Support Care Cancer, 2003. **11**(3): p. 137-43.

32. Hall, W., M. Christie, and D. Currow, *Cannabinoids and cancer: causation, remediation, and palliation.* Lancet Oncol, 2005. **6**(1): p. 35-42.

33. De Petrocellis, L., et al., *Effect on cancer cell proliferation of palmitoylethanolamide, a fatty acid amide interacting with both the cannabinoid and vanilloid signalling systems.* Fundam Clin Pharmacol, 2002. **16**(4): p. 297-302.

34. Guzman, M., C. Sanchez, and I. Galve-Roperh, *Cannabinoids and cell fate.* Pharmacol Ther, 2002. **95**(2): p. 175-84.

35. Guzman, M., *Neurons on cannabinoids: dead or alive?* Br J Pharmacol, 2003. **140**(3): p. 439-40.

36. Jones, S. and J. Howl, *Cannabinoid receptor systems: therapeutic targets for tumour intervention.* Expert Opin Ther Targets, 2003. **7**(6): p. 749-58.

37. Velasco, G., et al., *Hypothesis: cannabinoid therapy for the treatment of gliomas?* Neuropharmacology, 2004. **47**(3): p. 315-23.

38. Patsos, H.A., et al., *Cannabinoids and cancer: potential for colorectal cancer therapy.* Biochem Soc Trans, 2005. **33**(Pt 4): p. 712-4.

39. Kiskova, T., et al., *Future Aspects for Cannabinoids in Breast Cancer Therapy.* Int J Mol Sci, 2019. **20**(7).

40. De Petrocellis, L., et al., *The endogenous cannabinoid anandamide inhibits human breast cancer cell proliferation.* Proc Natl Acad Sci U S A, 1998. **95**(14): p. 8375-80.

41. Capozzi, A., et al., *Anti-Proliferative Properties and Proapoptotic Function of New CB2 Selective Cannabinoid Receptor Agonist in Jurkat Leukemia Cells.* Int J Mol Sci, 2018. **19**(7).

42. Roberto, D., L.H. Klotz, and V. Venkateswaran, *Cannabinoid WIN 55,212-2 induces cell cycle arrest and apoptosis, and inhibits proliferation, migration, invasion, and tumor growth in prostate cancer in a cannabinoid-receptor 2 dependent manner.* Prostate, 2019. **79**(2): p. 151-159.

43. Casanova, M.L., et al., *Inhibition of skin tumor growth and angiogenesis in vivo by activation of cannabinoid receptors.* J Clin Invest, 2003. **111**(1): p. 43-50.

44. Bifulco, M., et al., *Cannabinoids and cancer: pros and cons of an antitumour strategy.* Br J Pharmacol, 2006. **148**(2): p. 123-35.

45. McKallip, R.J., et al., *Targeting CB2 cannabinoid receptors as a novel therapy to treat malignant lymphoblastic disease.* Blood, 2002. **100**(2): p. 627-34.

46. Nagayama, T., et al., *Cannabinoids and neuroprotection in global and focal cerebral ischemia and in neuronal cultures.* J Neurosci, 1999. **19**(8): p. 2987-95.

47. Sinor, A.D., S.M. Irvin, and D.A. Greenberg, *Endocannabinoids protect cerebral cortical neurons from in vitro ischemia in rats.* Neurosci Lett, 2000. **278**(3): p. 157-60.

48. Milton, N.G., *Anandamide and noladin ether prevent neurotoxicity of the human amyloid-beta peptide.* Neurosci Lett, 2002. **332**(2): p. 127-30.

49. Wallace, M.J., B.R. Martin, and R.J. DeLorenzo, *Evidence for a physiological role of endocannabinoids in the modulation of seizure threshold and severity.* Eur J Pharmacol, 2002. **452**(3): p. 295-301.

50. Koob, G.F., *Drugs of abuse: anatomy, pharmacology and function of reward pathways.* Trends Pharmacol Sci, 1992. **13**(5): p. 177-84.

51. Wise, R.A., *Dopamine, learning and motivation.* Nat Rev Neurosci, 2004. **5**(6): p. 483-94.

52. Chen, J.P., et al., *Delta 9-tetrahydrocannabinol produces naloxone-blockable enhancement of presynaptic basal dopamine efflux in nucleus accumbens of conscious, freely-moving rats as measured by intracerebral microdialysis.* Psychopharmacology (Berl), 1990. **102**(2): p. 156-62.

53. Tanda, G., P. Loddo, and G. Di Chiara, *Dependence of mesolimbic dopamine transmission on delta9-tetrahydrocannabinol.* Eur J Pharmacol, 1999. **376**(1-2): p. 23-6.

54. Gardner, E.L., et al., *Facilitation of brain stimulation reward by delta 9-tetrahydrocannabinol.* Psychopharmacology (Berl), 1988. **96**(1): p. 142-4.

55. Rodriguez de Fonseca, F., et al., *Activation of corticotropin-releasing factor in the limbic system during cannabinoid withdrawal.* Science, 1997. **276**(5321): p. 2050-4.

56. Koob, G.F., *Drug addiction: the yin and yang of hedonic homeostasis.* Neuron, 1996. **16**(5): p. 893-6.

57. Lepore, M., et al., *Conditioned place preference induced by delta 9-tetrahydrocannabinol: comparison with cocaine, morphine, and food reward.* Life Sci, 1995. **56**(23-24): p. 2073-80.

58. Valjent, E. and R. Maldonado, *A behavioural model to reveal place preference to delta 9-tetrahydrocannabinol in mice.* Psychopharmacology (Berl), 2000. **147**(4): p. 436-8.

59. Zangen, A., et al., *Two brain sites for cannabinoid reward.* J Neurosci, 2006. **26**(18): p. 4901-7.

60. De Vries, T.J., et al., *A cannabinoid mechanism in relapse to cocaine seeking.* Nat Med, 2001. **7**(10): p. 1151-4.

61. Kreitzer, A.C. and W.G. Regehr, *Retrograde inhibition of presynaptic calcium influx by endogenous cannabinoids at excitatory synapses onto Purkinje cells.* Neuron, 2001. **29**(3): p. 717-27.

62. Ohno-Shosaku, T., T. Maejima, and M. Kano, *Endogenous cannabinoids mediate retrograde signals from depolarized postsynaptic neurons to presynaptic terminals.* Neuron, 2001. **29**(3): p. 729-38.

63. Wilson, R.I., G. Kunos, and R.A. Nicoll, *Presynaptic specificity of endocannabinoid signaling in the hippocampus.* Neuron, 2001. **31**(3): p. 453-62.

64. De Vries, T.J. and A.N. Schoffelmeer, *Cannabinoid CB1 receptors control conditioned drug seeking.* Trends Pharmacol Sci, 2005. **26**(8): p. 420-6.

65. Maldonado, R., O. Valverde, and F. Berrendero, *Involvement of the endocannabinoid system in drug addiction.* Trends Neurosci, 2006. **29**(4): p. 225-32.

66. Pacher, P., S. Batkai, and G. Kunos, *Blood pressure regulation by endocannabinoids and their receptors.* Neuropharmacology, 2005. **48**(8): p. 1130-8.

67. Jarai, Z., et al., *Cannabinoid-induced mesenteric vasodilation through an endothelial site distinct from CB1 or CB2 receptors.* Proc Natl Acad Sci U S A, 1999. **96**(24): p. 14136-41.

68. Wagner, J.A., et al., *Endogenous cannabinoids mediate hypotension after experimental myocardial infarction.* J Am Coll Cardiol, 2001. **38**(7): p. 2048-54.

69. Wagner, J.A., et al., *Coronary vasodilator effects of endogenous cannabinoids in vasopressin-preconstricted unpaced rat isolated hearts.* J Cardiovasc Pharmacol, 2005. **46**(3): p. 348-55.

70. Bonz, A., et al., *Cannabinoids acting on CB1 receptors decrease contractile performance in human atrial muscle.* J Cardiovasc Pharmacol, 2003. **41**(4): p. 657-64.

71. Maslov, L.N., et al., *Selective cannabinoid receptor agonist HU-210 decreases pump function of isolated perfused heart: role of cAMP and cGMP.* Bull Exp Biol Med, 2004. **138**(6): p. 550-3.

72. Sterin-Borda, L., C.F. Del Zar, and E. Borda, *Differential CB1 and CB2 cannabinoid receptor-inotropic response of rat isolated atria: endogenous signal transduction pathways.* Biochem Pharmacol, 2005. **69**(12): p. 1705-13.

73. Niederhoffer, N. and B. Szabo, *Cannabinoids cause central sympathoexcitation and bradycardia in rabbits.* J Pharmacol Exp Ther, 2000. **294**(2): p. 707-13.

74. Ishac, E.J., et al., *Inhibition of exocytotic noradrenaline release by presynaptic cannabinoid CB1 receptors on peripheral sympathetic nerves.* Br J Pharmacol, 1996. **118**(8): p. 2023-8.

75. Malinowska, B., et al., *Cannabinoid CB1 receptor-mediated inhibition of the neurogenic vasopressor response in the pithed rat.* Naunyn Schmiedebergs Arch Pharmacol, 1997. **356**(2): p. 197-202.

76. Szabo, B., U. Nordheim, and N. Niederhoffer, *Effects of cannabinoids on sympathetic and parasympathetic neuroeffector transmission in the rabbit heart.* J Pharmacol Exp Ther, 2001. **297**(2): p. 819-26.

77. Niederhoffer, N., K. Schmid, and B. Szabo, *The peripheral sympathetic nervous system is the major target of cannabinoids in eliciting cardiovascular depression.* Naunyn Schmiedebergs Arch Pharmacol, 2003. **367**(5): p. 434-43.

78. Batkai, S., et al., *Endocannabinoids acting at cannabinoid-1 receptors regulate cardiovascular function in hypertension.* Circulation, 2004. **110**(14): p. 1996-2002.

79. Liu, J., et al., *Functional CB1 cannabinoid receptors in human vascular endothelial cells.* Biochem J, 2000. **346 Pt 3**: p. 835-40.

80. Lagneux, C. and D. Lamontagne, *Involvement of cannabinoids in the cardioprotection induced by lipopolysaccharide.* Br J Pharmacol, 2001. **132**(4): p. 793-6.

81. Joyeux, M., et al., *Endocannabinoids are implicated in the infarct size-reducing effect conferred by heat stress preconditioning in isolated rat hearts.* Cardiovasc Res, 2002. **55**(3): p. 619-25.

82. Aronne, L.J., et al., *A clinical trial assessing the safety and efficacy of taranabant, a CB1R inverse agonist, in obese and overweight patients: a high-dose study.* Int J Obes (Lond), 2010. **34**(5): p. 919-35.

83. Proietto, J., et al., *A clinical trial assessing the safety and efficacy of the CB1R inverse agonist taranabant in obese and overweight patients: low-dose study.* Int J Obes (Lond), 2010. **34**(8): p. 1243-54.

84. Moreira, F.A. and J.A. Crippa, *The psychiatric side-effects of rimonabant.* Braz J Psychiatry, 2009. **31**(2): p. 145-53.

85. Yang, P., et al., *Lead discovery, chemistry optimization, and biological evaluation studies of novel biamide derivatives as CB2 receptor inverse agonists and osteoclast inhibitors.* J Med Chem, 2012. **55**(22): p. 9973-87.

86. Galiegue, S., et al., *Expression of central and peripheral cannabinoid receptors in human immune tissues and leukocyte subpopulations.* Eur J Biochem, 1995. **232**(1): p. 54-61.

87. Onaivi, E.S., et al., *Discovery of the presence and functional expression of cannabinoid CB2 receptors in brain.* Ann N Y Acad Sci, 2006. **1074**: p. 514-36.

88. Chen, D.-J., et al., *Brain cannabinoid receptor 2: expression, function and modulation.* 2017. **38**(3): p. 312.

89. Seely, K.A., et al., *Marijuana-based drugs: innovative therapeutics or designer drugs of abuse?* 2011. **11**(1): p. 36.

90. Idris, A.I., et al., *Regulation of bone mass, bone loss and osteoclast activity by cannabinoid receptors.* Nat Med, 2005. **11**(7): p. 774-9.

91. Aso, E. and I. Ferrer, *CB2 cannabinoid receptor as potential target against Alzheimer's disease.* Frontiers in neuroscience, 2016. **10**: p. 243.

92. Gómez-Gálvez, Y., et al., *Potential of the cannabinoid CB2 receptor as a pharmacological target against inflammation in Parkinson's disease.* Progress in Neuro-Psychopharmacology Biological Psychiatry, 2016. **64**: p. 200-208.

93. Chen, D.-J., et al., *Brain cannabinoid receptor 2: expression, function and modulation.* Acta Pharmacologica Sinica, 2017. **38**(3): p. 312.

94. Fulmer, M.L. and D.P. Thewke, *The Endocannabinoid System and Heart Disease: The Role of Cannabinoid Receptor Type 2.* Cardiovascular Haematological Disorders-Drug Targets, 2018. **18**(1): p. 34-51.

95. Guimaraes, S., J.P. Godbout, and J.F. Sheridan, *Repeated Social Defeat-Induced Neuroinflammation, Anxiety-like behavior and Resistance to Fear Extinction were*

Attenuated by the Cannabinoid Receptor Agonist WIN55, 212-2. Neuropsychopharmacology, 2018.

96. Turcotte, C., et al., *The CB 2 receptor and its role as a regulator of inflammation.* Cellular Molecular Life Sciences, 2016. **73**(23): p. 4449-4470.

97. Guindon, J. and A. Hohmann, *Cannabinoid CB2 receptors: a therapeutic target for the treatment of inflammatory and neuropathic pain.* British journal of pharmacology, 2008. **153**(2): p. 319-334.

98. Xiang, J., et al., *Successful Strategies to Determine High-Resolution Structures of GPCRs.* Trends Pharmacol Sci, 2016. **37**(12): p. 1055-1069.

99. Kobilka, B.K., *G protein coupled receptor structure and activation.* Biochim Biophys Acta, 2007. **1768**(4): p. 794-807.

100. Devinsky, O., et al., *Open-label use of highly purified CBD (Epidiolex(R)) in patients with CDKL5 deficiency disorder and Aicardi, Dup15q, and Doose syndromes.* Epilepsy Behav, 2018. **86**: p. 131-137.

101. Schlienz, N.J., et al., *The effect of high-dose dronabinol (oral THC) maintenance on cannabis self-administration.* Drug Alcohol Depend, 2018. **187**: p. 254-260.

102. Swartwood, C., et al., *Efficacy of Dronabinol for Acute Pain Management in Adults with Traumatic Injury: Study Protocol of A Randomized Controlled Trial.* Brain Sci, 2020. **10**(3).

103. Badowski, M.E. and P.K. Yanful, *Dronabinol oral solution in the management of anorexia and weight loss in AIDS and cancer.* Ther Clin Risk Manag, 2018. **14**: p. 643-651.

104. Sloan, M.E., et al., *The endocannabinoid system as a target for addiction treatment: Trials and tribulations.* Neuropharmacology, 2017. **124**: p. 73-83.

105. Tsang, C.C. and M.G. Giudice, *Nabilone for the Management of Pain.* Pharmacotherapy, 2016. **36**(3): p. 273-86.

106. Pergolizzi, J.V., Jr., et al., *Concise review of the management of iatrogenic emesis using cannabinoids: emphasis on nabilone for chemotherapy-induced nausea and vomiting.* Cancer Chemother Pharmacol, 2017. **79**(3): p. 467-477.

107. Fairhurst, C., et al., *Efficacy and safety of nabiximols cannabinoid medicine for paediatric spasticity in cerebral palsy or traumatic brain injury: a randomized controlled trial.* Dev Med Child Neurol, 2020.

108. Turcott, J.G., et al., *The effect of nabilone on appetite, nutritional status, and quality of life in lung cancer patients: a randomized, double-blind clinical trial.* Support Care Cancer, 2018. **26**(9): p. 3029-3038.

109. Sekar, K. and A. Pack, *Epidiolex as adjunct therapy for treatment of refractory epilepsy: a comprehensive review with a focus on adverse effects.* F1000Res, 2019. **8**.

110. Gado, F., et al., *Allosteric modulators targeting cannabinoid cb1 and cb2 receptors: implications for drug discovery.* Future Med Chem, 2019. **11**(15): p. 2019-2037.

111. Gado, F., et al., *Identification of the First Synthetic Allosteric Modulator of the CB2 Receptors and Evidence of Its Efficacy for Neuropathic Pain Relief.* J Med Chem, 2019. **62**(1): p. 276-287.

112. Price, M.R., et al., *Allosteric modulation of the cannabinoid CB1 receptor.* Mol Pharmacol, 2005. **68**(5): p. 1484-95.

113. Shao, Z., et al., *Structure of an allosteric modulator bound to the CB1 cannabinoid receptor.* Nat Chem Biol, 2019. **15**(12): p. 1199-1205.

114. Hryhorowicz, S., et al., *Allosteric Modulation of Cannabinoid Receptor 1-Current Challenges and Future Opportunities.* Int J Mol Sci, 2019. **20**(23).

115. Watson, J.D. and F.H. Crick, *Molecular structure of nucleic acids; a structure for deoxyribose nucleic acid.* Nature, 1953. **171**(4356): p. 737-8.

116. Kendrew, J.C. and M.F. Perutz, *X-ray studies of compounds of biological interest.* Annu Rev Biochem, 1957. **26**: p. 327-72.

117. Marion, D., *An introduction to biological NMR spectroscopy.* Mol Cell Proteomics, 2013. **12**(11): p. 3006-25.

118. Montelione, G.T., et al., *Protein NMR spectroscopy in structural genomics.* Nat Struct Biol, 2000. **7 Suppl**: p. 982-5.

119. Schneider, R., M. Blackledge, and M.R. Jensen, *Elucidating binding mechanisms and dynamics of intrinsically disordered protein complexes using NMR spectroscopy.* Curr Opin Struct Biol, 2019. **54**: p. 10-18.

120. Shi, Y., *A glimpse of structural biology through X-ray crystallography.* Cell, 2014. **159**(5): p. 995-1014.

121. Pear, B.L., *1896: the first year of X-rays in Colorado.* AJR Am J Roentgenol, 1995. **165**(5): p. 1075-8.

122. Chapman, H.N., *Microscopy: A new phase for X-ray imaging.* Nature, 2010. **467**(7314): p. 409-10.

123. Eckert, M., *Disputed discovery: the beginnings of X-ray diffraction in crystals in 1912 and its repercussions.* Acta Crystallogr A, 2012. **68**(Pt 1): p. 30-9.

124. Thomas, J.M., *Centenary: The birth of X-ray crystallography.* Nature, 2012. **491**(7423): p. 186-7.

125. Wagner, U. and C. Kratky, *Structure elucidation of natural compounds by X-ray crystallography.* Prog Chem Org Nat Prod, 2015. **100**: p. 1-75.

126. Venien-Bryan, C., et al., *Cryo-electron microscopy and X-ray crystallography: complementary approaches to structural biology and drug discovery.* Acta Crystallogr F Struct Biol Commun, 2017. **73**(Pt 4): p. 174-183.

127. Doerr, A., *Single-particle cryo-electron microscopy.* Nat Methods, 2016. **13**(1): p. 23.

128. Cheng, Y., *Single-Particle Cryo-EM at Crystallographic Resolution.* Cell, 2015. **161**(3): p. 450-457.

129. Cheng, Y., *Single-particle cryo-EM-How did it get here and where will it go.* Science, 2018. **361**(6405): p. 876-880.

130. Egelman, E.H., *The Current Revolution in Cryo-EM.* Biophys J, 2016. **110**(5): p. 1008-12.

131. Armache, J.P. and Y. Cheng, *Single-particle cryo-EM: beyond the resolution.* Natl Sci Rev, 2019. **6**(5): p. 864-866.

132. Bai, X.C., G. McMullan, and S.H. Scheres, *How cryo-EM is revolutionizing structural biology.* Trends Biochem Sci, 2015. **40**(1): p. 49-57.

133. Li, X., et al., *Crystal Structure of the Human Cannabinoid Receptor CB2.* Cell, 2019. **176**(3): p. 459-467 e13.

134. Liu, P., et al., *The structural basis of the dominant negative phenotype of the Gα i1 β 1 γ 2 G203A/A326S heterotrimer.* Acta Pharmacologica Sinica, 2016. **37**(9): p. 1259.

135. Zheng, S.Q., et al., *MotionCor2: anisotropic correction of beam-induced motion for improved cryo-electron microscopy.* Nat Methods, 2017. **14**(4): p. 331-332.

136. Rohou, A. and N. Grigorieff, *CTFFIND4: Fast and accurate defocus estimation from electron micrographs.* J Struct Biol, 2015. **192**(2): p. 216-21.

137. Zivanov, J., et al., *New tools for automated high-resolution cryo-EM structure determination in RELION-3.* Elife, 2018. **7**.

138. Punjani, A., et al., *cryoSPARC: algorithms for rapid unsupervised cryo-EM structure determination.* Nat Methods, 2017. **14**(3): p. 290-296.

139. Rosenthal, P.B. and R. Henderson, *Optimal determination of particle orientation, absolute hand, and contrast loss in single-particle electron cryomicroscopy.* J Mol Biol, 2003. **333**(4): p. 721-45.

140. Kucukelbir, A., F.J. Sigworth, and H.D. Tagare, *Quantifying the local resolution of cryo-EM density maps.* Nat Methods, 2014. **11**(1): p. 63-5.

141. Kelley, L.A., et al., *The Phyre2 web portal for protein modeling, prediction and analysis.* Nat Protoc, 2015. **10**(6): p. 845-58.

142. Emsley, P. and K. Cowtan, *Coot: model-building tools for molecular graphics.* Acta Crystallogr D Biol Crystallogr, 2004. **60**(Pt 12 Pt 1): p. 2126-32.

143. Adams, P.D., et al., *PHENIX: a comprehensive Python-based system for macromolecular structure solution.* Acta Crystallogr D Biol Crystallogr, 2010. **66**(Pt 2): p. 213-21.

144. Zhang, Y.X., et al., *Mutagenesis and Computer Modeling Studies of A GPCR Conserved Residue W5.43(194) in Ligand Recognition and Signal Transduction For CB2 Receptor.* International Immunopharmacology, 2011. **11**: p. 1303.

145. Ouyang, Q., et al., *Trisubstituted Sulfonamides: a New Chemotype for Development of Potent and Selective CB2 Receptor Inverse Agonists.* ACS Medicinal Chemistry Letters, 2013(DOI: 10.1021/ml3004236): p. February 22, 2013.

146. Li, H., K.-S. Leung, and M.-H. Wong. *idock: A multithreaded virtual screening tool for flexible ligand docking*. in *2012 IEEE Symposium on Computational Intelligence in Bioinformatics and Computational Biology (CIBCB)*. 2012. IEEE.

147. Chen, M., et al., *DAKB-GPCRs: An Integrated Computational Platform for Drug Abuse Related GPCRs.* Journal of chemical information modeling, 2019.

148. Trott, O. and A.J. Olson, *AutoDock Vina: improving the speed and accuracy of docking with a new scoring function, efficient optimization, and multithreading.* Journal of computational chemistry, 2010. **31**(2): p. 455-461.

149. Feng, Z., et al., *Modeling, molecular dynamics simulation, and mutation validation for structure of cannabinoid receptor 2 based on known crystal structures of GPCRs.* Journal of chemical information modeling, 2014. **54**(9): p. 2483-2499.

150. Feng, Z., et al., *Structural insight into tetrameric hTRPV1 from homology modeling, molecular docking, molecular dynamics simulation, virtual screening, and bioassay validations.* Journal of chemical information modeling, 2015. **55**(3): p. 572-588.

151. Jorgensen, W.L., et al., *Comparison of simple potential functions for simulating liquid water*. The Journal of Chemical Physics, 1983. **79**(2): p. 926.

152. Yin, J., et al., *Crystal structure of the human NK1 tachykinin receptor.* Proc Natl Acad Sci U S A, 2018. **115**(52): p. 13264-13269.

153. Maier, J.A., et al., *ff14SB: Improving the Accuracy of Protein Side Chain and Backbone Parameters from ff99SB.* J Chem Theory Comput, 2015. **11**(8): p. 3696-713.

154. Dickson, C.J., et al., *Lipid14: The Amber Lipid Force Field.* J Chem Theory Comput, 2014. **10**(2): p. 865-879.

155. Wang, J.M., et al., *Development and testing of a general amber force field.* Journal of Computational Chemistry, 2004. **25**(9): p. 1157-1174.

156. Case, D.A., et al., *AMBER 2018.* University of California, San Francisco, 2018.

157. Wang, J.M., T.J. Hou, and X.J. Xu, *Recent Advances in Free Energy Calculations with a Combination of Molecular Mechanics and Continuum Models.* Current Computer-Aided Drug Design, 2006. **2**(3): p. 287-306.

158. Hou, T., et al., *Assessing the performance of the MM/PBSA and MM/GBSA methods. 1. The accuracy of binding free energy calculations based on molecular dynamics simulations.* J Chem Inf Model, 2011. **51**(1): p. 69-82.

159. Hou, T., et al., *Assessing the performance of the molecular mechanics/Poisson Boltzmann surface area and molecular mechanics/generalized Born surface area methods. II. The accuracy of ranking poses generated from docking.* J Comput Chem, 2011. **32**(5): p. 866-77.

160. Hawkins, G.D., C.J. Cramer, and D.G. Truhlar, *Parametrized models of aqueous free energies of solvation based on pairwise descreening of solute atomic charges from a dielectric medium.* Journal of Physical Chemistry, 1996. **100**(51): p. 19824-19839.

161. Maeda, S., et al., *Development of an antibody fragment that stabilizes GPCR/G-protein complexes.* Nat Commun, 2018. **9**(1): p. 3712.

162. McAllister, S.D., et al., *Structural mimicry in class A G protein-coupled receptor rotamer toggle switches: the importance of the F3.36(201)/W6.48(357) interaction in cannabinoid CB1 receptor activation.* J Biol Chem, 2004. **279**(46): p. 48024-37.

163. Singh, R., et al., *Activation of the cannabinoid CB1 receptor may involve a W6.48/F3.36 rotamer toggle switch.* Journal of Peptide Research, 2002. **60**(6): p. 357-370.

164. Lin, S.W. and T.P.J.B. Sakmar, *Specific tryptophan UV-absorbance changes are probes of the transition of rhodopsin to its active state.* 1996. **35**(34): p. 11149-11159.

165. Hua, T., et al., *Crystal structure of the human cannabinoid receptor CB1*. Cell, 2016. **167**(3): p. 750-762. e14.

166. Dhopeshwarkar, A., et al., *Two Janus cannabinoids that are both CB2 agonists and CB1 antagonists.* Journal of Pharmacology Experimental Therapeutics, 2017. **360**(2): p. 300-311.

167. Raitio, K., et al., *Targeting the cannabinoid CB2 receptor: mutations, modeling and development of CB2 selective ligands.* Current medicinal chemistry, 2005. **12**(10): p. 1217-1237.

168. Rasmussen, S.G., et al., *Crystal structure of the β 2 adrenergic receptor–Gs protein complex.* Nature, 2011. **477**(7366): p. 549.

169. Kang, Y., et al., *Cryo-EM structure of human rhodopsin bound to an inhibitory G protein.* Nature, 2018. **558**(7711): p. 553.

170. Kumar, K.K., et al., *Structure of a Signaling Cannabinoid Receptor 1-G protein complex.* Cell, 2019. **176**(3): p. 448-458. e12.

171. Zheng, C., et al., *The second intracellular loop of the human cannabinoid CB2 receptor governs G protein coupling in coordination with the carboxyl terminal domain.* PloS one, 2013. **8**(5): p. e63262.

172. Timossi, C., et al., *Structural determinants in the second intracellular loop of the human follicle-stimulating hormone receptor are involved in Gs protein activation.* Molecular cellular endocrinology, 2002. **189**(1-2): p. 157-168.

173. Mnpotra, J.S., et al., *Structural basis of G protein-coupled receptor-Gi protein interaction: formation of the cannabinoid CB2 receptor-Gi protein complex.* J Biol Chem, 2014. **289**(29): p. 20259-72.

174. Scott, C.E., et al., *Identification and biochemical analyses of selective CB2 agonists.* Eur J Pharmacol, 2019. **854**: p. 1-8.

175. Leleu-Chavain, N., et al., *Benzo[d]thiazol-2(3H)-ones as new potent selective CB2 agonists with anti-inflammatory properties.* Eur J Med Chem, 2019. **165**: p. 347-362.

176. Nettekoven, M., et al., *Novel Triazolopyrimidine-Derived Cannabinoid Receptor 2 Agonists as Potential Treatment for Inflammatory Kidney Diseases.* ChemMedChem, 2016. **11**(2): p. 179-89.

177. Mugnaini, C., et al., *Synthesis of novel 2-(1-adamantanylcarboxamido)thiophene derivatives. Selective cannabinoid type 2 (CB2) receptor agonists as potential agents for the treatment of skin inflammatory disease.* Eur J Med Chem, 2019. **161**: p. 239-251.

178. Mukhopadhyay, P., et al., *The novel, orally available and peripherally restricted selective cannabinoid CB2 receptor agonist LEI-101 prevents cisplatin-induced nephrotoxicity.* Br J Pharmacol, 2016. **173**(3): p. 446-58.

179. Howlett, A.C., et al., *Cannabinoid physiology and pharmacology: 30 years of progress.* Neuropharmacology, 2004. **47 Suppl 1**: p. 345-58.

180. Ibsen, M.S., M. Connor, and M. Glass, *Cannabinoid CB1 and CB2 Receptor Signaling and Bias.* Cannabis Cannabinoid Res, 2017. **2**(1): p. 48-60.

181. Chen, X., et al., *Involvement of beta-arrestin-2 and clathrin in agonist-mediated internalization of the human cannabinoid CB2 receptor.* Curr Mol Pharmacol, 2014. **7**(1): p. 67-80.

182. Morales, P., P. Goya, and N. Jagerovic, *Emerging strategies targeting CB2 cannabinoid receptor: Biased agonism and allosterism.* Biochem Pharmacol, 2018. **157**: p. 8-17.

183. Nogueras-Ortiz, C., et al., *Retromer stops beta-arrestin 1-mediated signaling from internalized cannabinoid 2 receptors.* Mol Biol Cell, 2017. **28**(24): p. 3554-3561.

184. Bologna, Z., et al., *Biased G Protein-Coupled Receptor Signaling: New Player in Modulating Physiology and Pathology.* Biomol Ther (Seoul), 2017. **25**(1): p. 12-25.

185. Thompson, G.L., et al., *Novel GPCR paradigms at the mu-opioid receptor.* Br J Pharmacol, 2015. **172**(2): p. 287-96.

186. Wellendorph, P. and H. Bräuner‐Osborne, *Molecular basis for amino acid sensing by family CG‐protein‐coupled receptors.* British journal of pharmacology, 2009. **156**(6): p. 869-884.

187. Wenthur, C.J., et al., *Drugs for allosteric sites on receptors.* Annual review of pharmacology and toxicology, 2014. **54**: p. 165.

188. Lane, J.R., A. Abdul-Ridha, and M. Canals, *Regulation of G protein-coupled receptors by allosteric ligands.* ACS chemical neuroscience, 2013. **4**(4): p. 527-534.

189. Melancon, B.J., et al., *Allosteric modulation of seven transmembrane spanning receptors: theory, practice, and opportunities for central nervous system drug discovery.* Journal of medicinal chemistry, 2012. **55**(4): p. 1445-1464.

190. Christopoulos, A., *Allosteric binding sites on cell-surface receptors: novel targets for drug discovery.* Nature Reviews Drug Discovery, 2002. **1**(3): p. 198-210.

191. Conn, P.J., A. Christopoulos, and C.W. Lindsley, *Allosteric modulators of GPCRs: a novel approach for the treatment of CNS disorders.* Nature reviews Drug discovery, 2009. **8**(1): p. 41-54.

192. Bridges, T.M. and C.W. Lindsley, *G-protein-coupled receptors: from classical modes of modulation to allosteric mechanisms.* ACS chemical biology, 2008. **3**(9): p. 530-541.

193. Changrui Xing, et al., *Cryo-EM Structure of Human Cannabinoid Receptor CB2-Gi Signaling Complex.* Cell, 2020: p. In press.

194. Xie, X.-Q., et al., *In silico chemogenomics knowledgebase and computational system neuropharmacology approach for cannabinoid drug research*, in *Neuropathology of Drug Addictions and Substance Misuse*. 2016, Elsevier. p. 183-195.

195. Shen, Q., et al., *ASD v3. 0: unraveling allosteric regulation with structural mechanisms and biological networks.* Nucleic acids research, 2015. **44**(D1): p. D527-D535.

196. Rajasekaran, M., *Characterization of Allosteric Modulators of CB2 Receptors as Novel Therapeutics for Inflammatory Diseases*. 2011, University of Arkansas for Medical Sciences.

197. Bauer, M., et al., *Identification and quantification of a new family of peptide endocannabinoids (Pepcans) showing negative allosteric modulation at CB1 receptors.* Journal of biological chemistry, 2012. **287**(44): p. 36944-36967.

198. Alqarni, M., et al., *Examining the critical roles of human CB2 receptor residues Valine 3.32 (113) and Leucine 5.41 (192) in ligand recognition and downstream signaling activities.* Biochem. Biophys. Res. Commun., 2014. **452**(3): p. 334-339.

199. Ouyang, Q., et al., *Trisubstituted sulfonamides: a new chemotype for development of potent and selective CB2 receptor inverse agonists.* ACS medicinal chemistry letters, 2013. **4**(4): p. 387-392.

200. Zhang, Y. and X.-Q. Xie, *Biosynthesis, purification, and characterization of a cannabinoid receptor 2 fragment (CB2271-326).* Protein Expression and Purification, 2008. **59**(2): p. 249-257.

201. Zhang, Y., et al., *Mutagenesis and computer modeling studies of a GPCR conserved residue W5.43(194) in ligand recognition and signal transduction for CB2 receptor.* International Immunopharmacology, 2011. **11**(9): p. 1303-1310.

202. Rosati, O., et al., *One-pot heterogeneous synthesis of Δ3-tetrahydrocannabinol analogues and xanthenes showing differential binding to CB1 and CB2 receptors.* European journal of medicinal chemistry, 2014. **85**: p. 77-86.

203. Petrucci, V., et al., *Pepcan-12 (RVD-hemopressin) is a CB2 receptor positive allosteric modulator constitutively secreted by adrenals and in liver upon tissue damage.* Scientific Reports, 2017. **7**(1): p. 1-14.

204. Soethoudt, M., et al., *Cannabinoid CB2 receptor ligand profiling reveals biased signalling and off-target activity.* Nat Commun, 2017. **8**: p. 13958.